



UPPSALA
UNIVERSITET

*Digital Comprehensive Summaries of Uppsala Dissertations
from the Faculty of Science and Technology 2110*

Aqueous graphene dispersions for paper packaging

WEI ZHAO



ACTA
UNIVERSITATIS
UPSALIENSIS
UPPSALA
2022

ISSN 1651-6214
ISBN 978-91-513-1389-4
URN urn:nbn:se:uu:diva-465565

Dissertation presented at Uppsala University to be publicly examined in Beurlingrummet, Ångströmlaboratoriet, Lägerhyddsvägen 1, Uppsala, Friday, 25 February 2022 at 14:00 for the degree of Doctor of Philosophy. The examination will be conducted in English. Faculty examiner: Prof. Valeria Nicolosi (Trinity College Dublin).

Abstract

Zhao, W. 2022. Aqueous graphene dispersions for paper packaging. *Digital Comprehensive Summaries of Uppsala Dissertations from the Faculty of Science and Technology* 2110. 107 pp. Uppsala: Acta Universitatis Upsaliensis. ISBN 978-91-513-1389-4.

Graphene is widely touted as the thinnest and the most versatile material available. As an atomically thin layer of carbon atoms arranged in a hexagonal configuration, graphene has a combination of technologically important properties, such as thermal and electrical conductivity, mechanical strength, and impermeability to gases. From an industrial perspective on applications, water as a dispersing media for graphene offers safer handling and environmental benefits compared with conventional organic solvents. However, the high surface tension of water and the attractive forces between graphene surfaces drive the sheets to aggregation. Although surfactants have been an important stepping stone in the advancement of aqueous graphene dispersions, these surface-active molecules are often needed in excess and have adverse effects on coatings during film formation. These challenges limit the industrial relevance of graphene as an effective barrier in composites. In general, gas barriers against both oxygen and water vapour, made from a single coating formulation, is seemingly a holy grail for the packaging industry. In this thesis work, the aim was to gain a fundamental understanding of aqueous graphene dispersions for gas barriers used in paper packaging. Biobased materials were systematically investigated as dispersing agents for graphene based on dispersing conditions and functional barrier performance. Flavin mononucleotide (FMN), a food additive, dispersed graphene using a relatively low amount of FMN and showed intriguing spectroscopic signatures of π - π interactions with graphene. Starch nanoparticles (SNPs) realised concentrated and stable aqueous graphene dispersions for composite films. The SNP-stabilized graphene sheets in starch films lowered the gas permeability of both oxygen and water vapour simultaneously by over 70% under all the conditions tested. In general, a combined gas barrier performance is unusual for both bioplastics and common petrochemical-based plastics used in the packaging industry. Motivated by the graphene network leading to the extraordinary barrier performance, the aqueous SNP-graphene dispersion was modified for inkjet printing. The printed patterns were flexible and electrically conductive in the order of 10^4 S m^{-1} that is on par with the highest reported values in the literature. These surfactant-free aqueous SNP-graphene dispersions have the potential and versatility for paper-based gas barriers with integrated electronics. Multifunctional composite films made from these dispersions, when optimized, could become competitive with commercial plastics, and meet the current and future demands of the packaging industry.

Keywords: Graphene, Aqueous graphene dispersions, Noncovalent interactions, Composites, Barriers, Inkjet printing

Wei Zhao, Department of Electrical Engineering, Solid-State Electronics, Box 534, Uppsala University, SE-751 21 Uppsala, Sweden.

© Wei Zhao 2022

ISSN 1651-6214

ISBN 978-91-513-1389-4

URN urn:nbn:se:uu:diva-465565 (<http://urn.kb.se/resolve?urn=urn:nbn:se:uu:diva-465565>)

“Now is the time to understand more, so that we may fear less.”

Maria Skłodowska-Curie

List of Papers

This thesis is based on the following papers, which are referred to in the text by their Roman numerals.

- I. **Zhao, W.**, Sugunan, A., Zhang, Z., Ahniyaz, A. (2019) Graphene and Flavin Mononucleotide Interaction in Aqueous Graphene Dispersions. *J. Phys. Chem. C*, 123(43):26282–26288
- II. **Zhao, W.**, Sugunan, A., Gillgren, T., Larsson, A. J., Zhang, Z., Zhang, S., Ahniyaz, A. (2021) Surfactant-Free Stabilization of Aqueous Graphene Dispersions Using Starch as a Dispersing Agent. *ACS Omega*, 6(18):12050-12062
- III. **Zhao, W.**, Sugunan, A., Gillgren, T., Larsson, A. J., Zhang, Z., Zhang, S., Sommertune, J., Dobryden, I., Ahniyaz, A. (2021) Surfactant-free starch-graphene composite films as simultaneous oxygen and water vapour barriers. *npj 2D Mater. Appl.* (accepted)
- IV. Majee, S., **Zhao, W.**, Sugunan, A., Gillgren, T., Larsson, A. J., Brooke, R., Nordgren, N., Zhang, Z., Zhang, S., Nilsson, D., Ahniyaz, A. (2021) Highly Conductive Films by Rapid Photonic Annealing of Inkjet Printable Starch–Graphene Ink. *Adv. Mater. Interfaces* (epub ahead of print)

Reprints were made with permission from the respective publishers.

Author's contributions

This thesis is based on the following papers, which are referred to in the text by their Roman numerals.

- I. All experimental work and data analysis. A major part of the manuscript preparation.
- II. Major part of experimental work , data analysis, and manuscript preparation.
- III. Major part of experimental work, data analysis, and manuscript preparation.
- IV. Preparation of graphene dispersion and characterizations thereof. A minor part of experimental work and data analysis, and manuscript preparation.

Related work not included in this thesis

- I. Fall, A., **Zhao, W.**, Abitbol, T., Granberg, H., Blademo, Å., Nordgren, N., Sugunan A. (2021) Stabilizing graphene using cellulose nanofibers for electrically conductive and high barrier composite films. *Manuscript*

Contents

1	Introduction	13
1.1	Motivation and objectives	16
1.2	Outline of this thesis.....	17
2	Theoretical background	19
2.1	Graphene	19
2.1.1	A brief history.....	19
2.1.2	Structure and properties.....	20
2.1.3	Production methods	21
2.2	Aqueous graphene dispersions	22
2.2.1	DLVO theory	22
2.2.2	Zeta potential	24
2.2.3	Surface modifications	25
2.3	Graphene applications	28
2.3.1	Gas barriers.....	28
2.3.2	Conductive inks	30
3	Experimental methods	33
3.1	Chemicals and materials.....	33
3.1.1	Graphene powders	33
3.1.2	Bio-based dispersing agents	33
3.2	Aqueous graphene dispersions and composites	35
3.2.1	Preparation of aqueous graphene dispersions.....	35
3.2.2	Fabrication of graphene composite films	37
3.3	Characterization techniques	38
3.3.1	Spectroscopic analysis.....	38
3.3.2	Microscopy imaging	42
3.3.3	Surface charge and energy.....	44
3.3.4	Thermal properties.....	46
3.3.5	Electrical properties.....	47
3.3.6	Gas barrier performance	48
3.3.7	Inkjet printing	50
4	Results and Discussion	51
4.1	Aqueous graphene dispersions	51
4.1.1	Graphene concentration.....	51
4.1.2	Starting concentration parameters	53

4.1.3	Processing parameters	54
4.1.4	Colloidal stability	55
4.1.5	Particle size distribution	56
4.1.6	Morphology	57
4.1.7	Topography.....	58
4.1.8	Physicochemical properties	59
4.1.9	FMN-graphene interactions	64
4.1.10	SNP-graphene interactions.....	66
4.2	Graphene composite films.....	69
4.2.1	Fabrication and optimization of the films.....	69
4.2.2	Graphene distribution in the composite films.....	71
4.2.3	Raman study on the graphene-matrix interaction.....	73
4.2.4	Physicochemical properties of composite films	77
4.3	Graphene composite applications.....	78
4.3.1	Oxygen and water vapour permeability.....	78
4.3.2	Electrical conductivity	82
4.4	Inkjet printable graphene inks	83
4.4.1	Formulation of SNP-graphene inks	83
4.4.2	Post-treatment conditions	84
4.4.3	Surface morphology	86
4.4.4	Electrical conductivity.....	87
5	Conclusions and outlook	89
6	Sammanfattning på Svenska	91
7	Acknowledgments	93
8	References	95

Abbreviations

0D	Zero dimensional
1D	One dimensional
2D	Two dimensional
3D	Three dimensional
AFM	Atomic force microscopy
BF	Bright-field
CTAB	Hexadecyl trimethylammonium bromide
DF	Dark-field
DLVO	Derjaguin-Landau-Verwey-Overbeek
DMF	Dimethylformamide
DMSO	Dimethyl sulfoxide
DTAB	Dodecyl trimethylammonium bromide
DTG	Derivative thermogravimetry
EVOH	Ethylene vinyl alcohol
FMN	Flavin mononucleotide
FT-IR	Fourier transform infrared spectroscopy
GO	Graphene oxide
HAADF	High-angle annular dark-field
HDPE	High-density polyethylene
LDPE	Low-density polyethylene
NMP	N-methyl-2-pyrrolidone
OP	Oxygen permeability
OTR	Oxygen transmission rate
PAH	Polycyclic aromatic hydrocarbons
PET	Polyethylene terephthalate
PP	Polypropylene
PVDC	Polyvinylidene chloride
RGO	Reduced graphene oxide
SC	Sodium cholate
SDBS	Sodium dodecyl benzenesulfonate
SDC	Sodium deoxycholate
SDS	Sodium dodecyl sulphate
SEM	Scanning electron microscopy
SNP	Starch nanoparticle
STC	Sodium taurocholate

STEM	Scanning transmission electron microscopy
SWCNTs	Singe-walled carbon nanotubes
TGA	Thermogravimetric analysis
TTAB	Tetradecyl trimethylammonium bromide
UV-vis	Ultraviolet-visible
WVP	Water vapour permeability
WVTR	Water vapour transmission rate

1 Introduction

Since the first graphene monolayer was discovered in 2004[1], the world has witnessed many intriguing breakthroughs in graphene research[2], in parallel, important advances in the global production of large-scaled and cost-effective graphene[3]. Today, we could be standing at the tipping point and witnessing more graphene applications entering the market [4]. Graphene, in its pristine form, is simply a 2D network of carbon atoms arranged in a hexagonal configuration. This configuration gives rise to a combination of unprecedented properties that exceed beyond those measured in other materials. For instance, the electrical conductivity[5,6] and the thermal conductivity[7] exceed that of copper, while the mechanical strength makes graphene the strongest material ever measured[8]. Furthermore, despite being only one atom thick, graphene is considered impermeable to all gases and liquids[9–11]. These technologically important properties and a wealth of many others, combined in a single material, could lead to new disruptive technologies or even replace the existing technologies and materials in a wide range of applications[12], such as gas barrier coatings for paper-packaging[13] or conductive inks for flexible printed electronics[14]. To make use of graphene in wide-ranging high-performing applications, scalable production of single- to few-layer graphene is often required. To meet this requirement, a deeper understanding of suitable dispersing systems is needed. In the early stage of graphene research, dispersions of graphene were extensively studied in organic solvents, such as dimethylformamide (DMF)[15], N-methyl-2-pyrrolidone (NMP)[16,17], and dimethyl sulfoxide (DMSO)[18]. Although graphene can be dispersed well in these solvents ($0.01\text{--}28\text{ mg mL}^{-1}$), most organic solvents are often toxic, flammable, or difficult to remove due to high boiling points ($\sim 203\text{ }^{\circ}\text{C}$)[19]. From an industrial perspective on applications, water is the most sustainable alternative. Dispersing graphene in water can offer safer handling and improved biocompatibility, and most importantly, minimize the adverse impact on human health and the environment. However, graphene is not readily dispersible in aqueous systems due to its low surface energy (46.7 mN m^{-1})[20] compared to the high surface tension of water (72.3 mN m^{-1}). Furthermore, the attractive van der Waals forces acting between two similar graphene surfaces lead to restacking, aggregation and eventually sedimentation. To prevent graphene restacking in water, a wide range of

surfactants has been explored as dispersing agents. These are surface-active molecules that consist of a hydrophobic body (affinity towards nonpolar solvents) and a hydrophilic head group (affinity towards polar solvents). The dispersion mechanism of surfactants is by non-covalent adsorption of the hydrophobic body onto the graphene surface and extension of the hydrophilic head group towards the aqueous phase, thus separating the graphene sheets by electrostatic repulsion, steric hindrance, or often the combination. The earliest pioneering work studied commercially available surfactants with a negatively charged head group (anionic), such as sodium dodecyl benzenesulfonate (SDBS)[21], sodium cholate (SC)[22], sodium deoxycholate (SDC)[23], sodium taurocholate (STC)[24], sodium dodecyl sulphate (SDS)[25], and many more[26]. The positively charged counterparts (cationic) were long-chained dodecyl trimethylammonium bromide (DTAB), tetradecyl trimethylammonium bromide (TTAB), and hexadecyl trimethylammonium bromide (CTAB)[27]. As for the neutral (non-ionic), they were Pluronics, Tween80, Brij700, and TritonX100[28]. These aqueous surfactant systems could achieve a graphene concentration of 0.002-7.1 mg mL⁻¹. In addition to surfactants, there are biomolecules with amphiphilic characteristics, such as deoxyribonucleic acid[29], peptides[30], and proteins[31,32]. These biomolecule systems could also achieve a graphene concentration of 0.03-7 mg mL⁻¹. Among other amphiphilic biomolecules, flavin mononucleotide (FMN)[33] has been reported to achieve up to 50 mg mL⁻¹[34], which merits further investigation. Although the conventional amphiphilic molecules have been essential in aiding the dispersion of graphene in water, on the other hand, their surface activity often leads to complications in coating formulations and end-uses[35]. In particular, molecules with high mobility[36] and potential incompatibility with the polymer matrix[37] tend to migrate efficiently towards the interfaces (substrate/film or film/air) during film formation. The surface migration of molecules, such as surfactants, is a general challenge in many application areas. For gas barriers, these migrating events lead to defects inside the film and at the film interfaces, thus opening channels that allow gas permeation through the film[38]. Moreover, the increasing occurrence of synthetic surfactants in the environment, including their degraded products, is raising more concerns due to the adverse effects on the ecosystem[39,40]. These complications limit the applications of surfactant-stabilized graphene and motivate the need for alternatives. From both a technical and a sustainable perspective, natural biopolymers made by nature have shown great potential[41,42].

Among many biopolymers, starch is one of the most abundant polysaccharides in nature. For decades, starch has been extracted from plant-based sources on a large scale and used as a versatile additive in a wide range of industry sectors, such as food, papermaking, and pharmaceuticals[43]. Furthermore, the facile processing and thermoplastic behaviour of starch makes it a promising dispersing agent as well as a polymer matrix for composite films.

In the last 20 years, starch from a wide range of botanical sources has been explored to disperse different carbon allotropes. The earliest work explored the dispersion of 1D allotropes of carbon, such as single-wall carbon nanotubes (SWCNTs), in aqueous systems using amylose[44] and amylopectin[45]. In the following years, the SWCNTs were chemically functionalized with polar groups to increase their hydrophilicity as well as facilitate the interaction with the starch polymer matrix via hydrogen bonding[46,47]. After the discovery and rise of graphene[1,2], the past knowledge was extended to graphene and its 2D derivatives. For instance, graphene oxide (GO) with an oxygen-rich surface could be mixed directly with a polymer matrix made from starch[48] and starch/chitosan mixtures[49], respectively, and obtain composites with improved mechanical properties. Moreover, the oxygen groups on the GO surface increase its hydrophilicity and eliminate the need for dispersing agents in aqueous systems. On the other hand, these oxygen groups and other impurities substantially limit the important properties of graphene, such as electrical conductivity and barrier properties. To restore these properties, starch was explored as a reducing agent to remove the oxygen groups as well as grafted onto the resulting reduced GO (RGO)[50,51], however, with limited improvements in the electrical conductivity[52,53]. In general, the interfacial interaction between GO/RGO and starch is attributed to hydrogen bonding via their oxygen groups, respectively[54–56]. Overall, while these oxygen-rich 2D materials behave more hydrophilic and could disperse well in aqueous systems, they have limited potential in gas barrier and electrical applications. In general, hydrophilic materials make poor water vapour barriers, while conversely, hydrophobic materials make poor oxygen barriers[57]. This trend originates from the chemical nature of oxygen molecules (affinity to nonpolar) and water molecules (affinity to polar). These mutually opposing material limitations of the oxygen and the water vapour barrier, respectively, make the engineering of a combined gas barrier from a single coating formulation an interesting challenge. Graphene, being both hydrophobic and impermeable to all gases under ambient conditions, is therefore a promising barrier material in this regard. To the best of my knowledge, a simultaneous gas barrier performance (oxygen and water vapour) has not been achieved with bio-based and biodegradable polymers. Thus far, research efforts have achieved either one or the other.

In this thesis work, FMN and starch nanoparticles (SNPs) were investigated as dispersing agents for graphene in water. Among these, starch was selected and processed as a dispersing agent that achieved concentrated SNP-graphene dispersions. The SNP-graphene dispersion was further customized for gas barrier applications and demonstrated a simultaneous gas barrier performance. The barrier performance was substantially improved compared with the common bio-based and biodegradable polymers. Furthermore, the barrier performance was also comparable to the most common commercial plastics,

such as ethylene vinyl alcohol (EVOH), polyvinylidene chloride (PVDC) in terms of oxygen permeability (OP) and low-density polyethylene (LDPE) and polypropylene (PP) in terms of water vapour permeability (WVP). Moreover, the SNP-graphene dispersion was also customized for inkjet printable inks and achieved high electrical conductivity values on par with the highest reported in the literature. These findings demonstrate that starch can function as a promising dispersing agent for the preparation of concentrated and stable aqueous graphene dispersions for wide-ranging applications, such as barrier composite films for paper-packaging applications as well as conductive inks for inkjet-printed flexible electronics.

1.1 Motivation and objectives

The main motivation of this thesis work was the development of a concentrated aqueous graphene dispersion and its potential for gas barrier coatings used in paper-packaging applications. The packaging industry has high demands on the barrier coatings used in food packaging to protect all types of food and beverages from gases and moisture from the surroundings. To meet the current demands, the most common barrier coatings used today are multi-layered laminates comprising petrochemical-based polymers that are non-biodegradable, and in some cases, additional metal foils. Furthermore, some of these non-biodegradable polymers are challenging to recycle as well as harmful to human health. In addition, consumer products from such polymers contribute to plastic pollutants that are accumulating in the ocean at an alarming rate and have adverse effects on the environment and its ecosystems. This continuation poses a global challenge and stresses the need for environmentally friendly substitutions, such as bio-based and biodegradable polymers. However, to enable competitive substitutions, biopolymers need fillers to improve specific features, such as the gas barrier performance. One of the most promising fillers in this regard is indeed graphene, due to its wealth of technologically important properties, and most importantly, impermeability to gases and liquids. To produce barrier coatings with graphene on a large scale, solution deposition is a promising route where the quality of the graphene film is offset by the cost-advantages and facile processing. For this purpose, stable and concentrated aqueous graphene dispersion is needed.

The objective of this thesis work was to develop stable and concentrated aqueous graphene dispersions that can be customized for wide-ranging applications, such as gas barrier coatings for paper-packaging or conductive inks for inkjet printing. With the motivation and the targeted applications in the scope, a large part of the thesis work was to identify suitable dispersing

agents to disperse graphene in water. Moreover, the dispersing agent used to aid the graphene dispersion must also be compatible with the intended polymer matrix, thus minimizing the adverse effects on the final composite film properties. Traditionally, surfactants have been essential in the dispersion of graphene. However, a general challenge is their high surface activity and thereby tendency to migrate within the composite film, thus impairing the gas barrier properties. Therefore, this thesis work is focused mainly on the formulation of aqueous graphene dispersions and the elucidation of the dispersing conditions as well as mechanisms of bio-based dispersing agents. From an industrial perspective, starch was identified as a promising candidate. Furthermore, starch plays an important role in the paper-packaging industry as a binder and surface sizing agent. Therefore, the starch-stabilized aqueous graphene dispersion was selected for further formulations and functional studies of barrier composite films and conductive inks. The objectives of this thesis are: (I) Enhance fundamental understanding of graphene and dispersing agents in aqueous systems. (II) Create a knowledge platform for aqueous graphene dispersions to enable the preparation of customizable dispersions for various industrial applications, such as graphene-based barriers, “smart packaging”, or patterned conductive coatings. (III) Enhance knowledge transfer and skills transfer between academia and industry.

1.2 Outline of this thesis

In this thesis work, the aqueous graphene dispersion and its preparations, characterizations, and applications are discussed. The thesis begins with an introduction to the field of aqueous graphene dispersions and indicates the gap (Chapter 1). The next chapter provides the theoretical background of fundamental graphene properties, dispersion mechanisms, and applications (Chapter 2). The following chapter describes the experimental methods and characterizations thereof (Chapter 3). Then, the results and main findings are presented and discussed (Chapter 4). Finally, the last chapter summarizes the work and outlook (Chapter 5).

2 Theoretical background

2.1 Graphene

2.1.1 A brief history

Graphene, as an atomically thin layer (2D), is one of many crystalline forms of the carbon element, and the basic building block in all other dimensional carbon allotropes, such as fullerene (0D), nanotube (1D), and graphite (3D). In nature, graphene is the 2D layers stacked into 3D graphite, a naturally occurring mineral that can be found on the surface of the earth and is one of the longest well-known forms of pure carbon. In the 1560s, the oldest known graphite pencil was created. At that time, graphite was mostly used as a marking or writing implement for over three centuries. Until 1924, after the discovery of X-ray, the crystal structure of graphite was identified as hexagonal for the first time[58]. Later in the 1940s, the theories of the electrical properties of graphene began to unfold[59]. Back then, it was predicted that such an atomically thin layer of carbon atoms could not exist due to thermodynamic instability. Then, in 2004 when the first graphene monolayer was isolated by the “scotch tape” method, the existence of graphene was confirmed, and many ground-breaking properties were possible to be measured. Today, graphene has attracted unprecedented interest and is touted as the thinnest and most versatile material available to mankind.

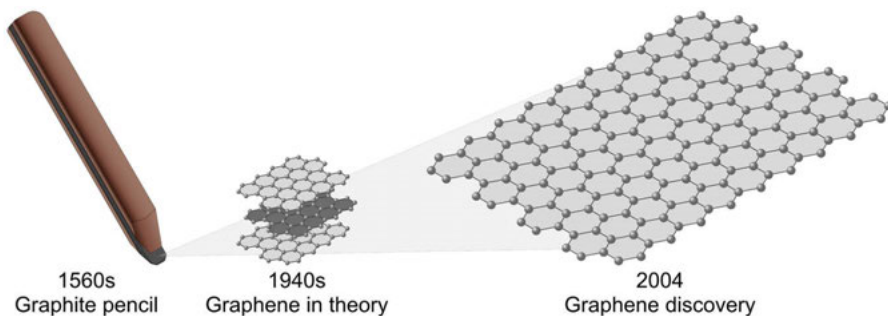


Figure 1. The timeline of the first known graphite pencil (the 1560s) to the early theoretical studies of graphene (1940s) and the discovery of graphene monolayer (2004).

2.1.2 Structure and properties

Graphene is composed of a planar hexagonal lattice of sp^2 -hybridized carbon atoms. Each of these carbon atoms has fused atomic orbitals that can form three σ -orbitals and one π -orbital (**Figure 2**). The three σ -orbitals are responsible for the in-plane covalent bonds (σ -bonds) between neighbouring atoms with a 0.142 nm distance apart and a 120° angle wide. The remaining π -orbital is either responsible for the restacking of graphene layers with an interlayer separation of 0.335 nm, or in a monolayer, de-localized out-of-plane (above and below) and establishes a conjugated π -system. This electronic configuration gives rise to a combination of technologically important properties of graphene.

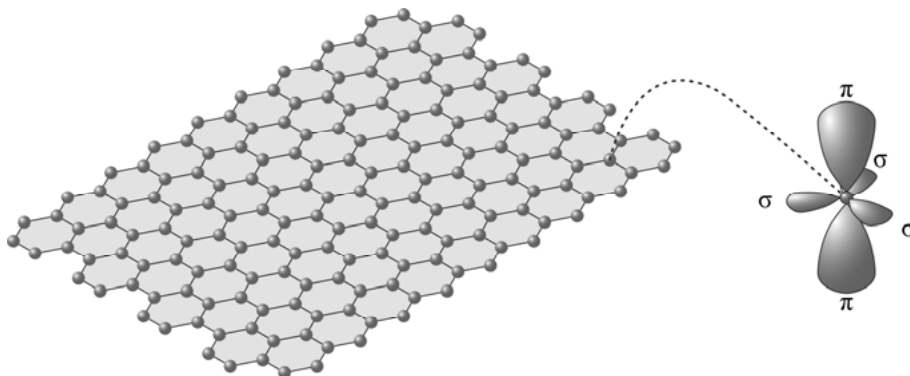


Figure 2. A graphene sheet with a hexagonal lattice of sp^2 -hybridized carbon atoms. A single carbon atom with mixed atomic orbitals forms three σ -orbitals and one de-localized π -orbital (above and below).

As an atomically thin layer with delocalized π -electrons, many of the graphene properties exceed far beyond those measured in other materials (**Figure 3**). For instance, graphene has demonstrated a room temperature electron mobility of $250,000 \text{ cm}^2 \text{ V}^{-1} \text{ s}^{-1}$ (100 times faster than that of silicon and a comparable electrical conductivity to copper and silver)[5,6], a thermal conductivity of 5000 W mK^{-1} (10 times higher than that of copper)[7], and a breaking strength of 42 N m^{-1} with a tensile strength up to 130 GPa and a Young's modulus of 1 TPa (100 times stronger than steel)[8]. Furthermore, graphene also has a high surface area of $2630 \text{ m}^2 \text{ g}^{-1}$ [60] and a lightweight of only 0.00077 g m^{-2} . In addition, it's almost optically transparent as it absorbs only 2.3% of the light intensity per layer[61]. Most importantly, despite being only one atom thick, graphene has extraordinary impermeability to gases and liquids[9–11]. Since 2008, graphene was touted as completely impermeable to all gases, including the smallest and potentially leakiest gas helium. Until recently in 2020, a discernible amount of hydrogen was found to transport through graphene at the surface ripples via a two-stage chemisorption and desorption

process[62]. At the catalytically active graphene ripples, the hydrogen can share its electron with graphene and become indistinguishable as an adsorbed proton, and thereby flip to the other side of the sheet where it can desorb[63]. Nevertheless, bilayer graphene remains indeed undisputed as impermeable to all gases. Therefore, owing to all these extraordinary properties combined within a single material, graphene has the potential to create disruptive innovation and replace currently used materials. In this thesis work, the impermeability to gases and the electrical conductivity of graphene are the most relevant properties.

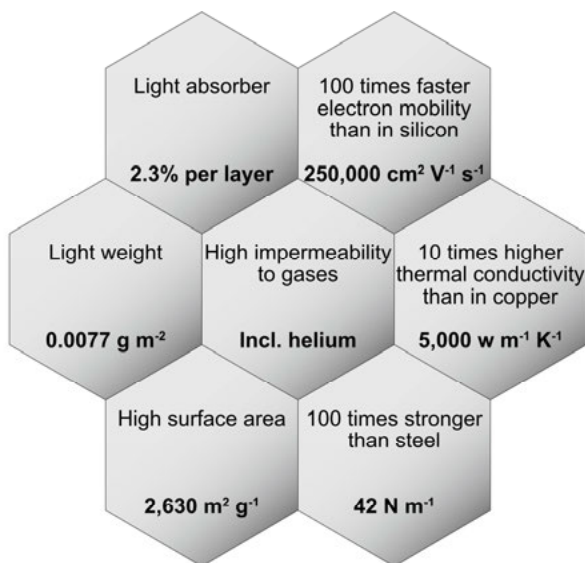


Figure 3. Graphene features and technologically important properties.

2.1.3 Production methods

To expand the industrial applicability of graphene, large-scale and cost-effective production methods are needed. The production methods of graphene can be classified into two fundamentally different approaches, the bottom-up and the top-down. In general, the bottom-up approach is based on the growth of graphene atom by atom (e.g. CVD, growth on SiC, and MBE)[64]. Although the bottom-up methods can offer the highest graphene quality, they are often associated with high temperatures up to 1000°C , the need for ultra-high vacuum, and high production costs[3]. Furthermore, the graphene size and quantity are restricted by the growth substrate. Therefore, the bottom-up approach is not suitable for mass production. The top-down approach, on the other hand, is based on the exfoliation of the bulk material graphite down to individual graphene layers. In graphite, the carbon atoms are held by shorter covalent σ -bonds (0.142 nm), while the individual layers are

held by longer π -bonds (0.335 nm). The longer π -bonds are relatively weaker and therefore facilitate the exfoliation of graphite. The exfoliation can be performed both dry (e.g. mechanical cleavage, anodic bonding, and photoexfoliation)[64] and in liquid-phase[65]. Among these two approaches, liquid-phase exfoliation offers scalable production of graphene at low costs by applying shear force. The minimum shear force needed for efficient exfoliation of graphite has been suggested to occur at 10^4 s^{-1} [66], which can be achieved by high-shear mixers[66], high-pressure homogenizers[67], and microfluidizers[68]. In general, the most common technique is ultrasonication via bath or probe[69]. The ultrasonication process is based on ultrasound waves (20 kHz) that propagate through the suspension of graphite and generate shear force via acoustic cavitation[70]. In only 1 mm thick graphite material, ~ 3 million graphene layers could be exfoliated. Therefore, liquid-phase exfoliation is the most cost-efficient approach and will pave the way for the mass production of graphene[3].

2.2 Aqueous graphene dispersions

2.2.1 DLVO theory

In the 1940s, Boris Derjaguin, Lev Landau, Evert Verwey and Theo Overbeek proposed a theory of colloidal stability that became known as the DLVO theory. In the DLVO theory, the interaction between two opposing forces (repulsive and attractive) are considered to impact colloidal stability. Accordingly, the colloidal stability is considered attained when the net energy between the two opposing forces is balanced or when the repulsive forces (red) overcome the attractive forces (blue), thus resulting in an energy barrier (**Figure 4**). The total potential energy of interaction (E_{tot}) is related to the repulsion from the electrical double layer (E_{EDL}), while the attraction from the van der Waals forces (E_{vdW}), as given by equation (2.1).

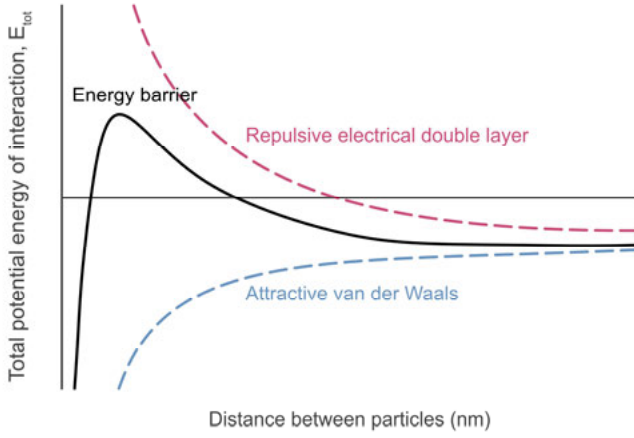


Figure 4. Schematic diagram of the total potential energy of interaction as a function of the distance between particles, according to the DLVO theory[71].

$$E_{tot} = E_{EDL} + E_{vdW} \quad (2.1)$$

The attractive forces originating from the van der Waals forces, E_{vdW} , are always present and can act between two similar particles, such as two graphene sheets, regardless of the chemical nature of the particles or the dispersion system. The equation (2.2) for the van der Waals forces has been calculated[21] similar to the method pioneered by Hamaker[72]:

$$E_{vdW} = -\frac{A\pi\rho^2C}{2D^4} \quad (2.2)$$

In this equation, the E_{vdW} is related to the surface area (A), the density of atoms in the area (ρ), a constant related to the van der Waals forces and the interatomic separation (C), over the separation between the sheets (D). On the other hand, the repulsive forces originating from the electrical double layer, E_{EDL} , are acquired either from the particle surface charge or the adsorption from the solution. The equation (2.3) for the repulsive forces have been derived by Israelachvili[71] and then adapted for two idealized parallel sheets[21]:

$$E_{EDL} = 4A\varepsilon_r\varepsilon_0\kappa\zeta^2e^{-\kappa D} \quad (2.3)$$

In this equation, the E_{EDL} is related to the relative permittivity of the dispersion system and the free space ($\varepsilon_r\varepsilon_0$), respectively, the Debye screening length (κ^{-1}), and the zeta potential (ζ). Furthermore, the Debye length is the

characteristic decay distance to which an electric potential still exists, and the general equation is given by (2.4).

$$\kappa^{-1} = \sqrt{\frac{kT\varepsilon_r\varepsilon_0}{e^2 \sum_i n_i z_i^2}} \quad (2.4)$$

Here, the κ^{-1} is given by the square root of the Boltzmann constant (k), the temperature (T), the $\varepsilon_r\varepsilon_0$, over the elementary charge (e), the number density of ions in the bulk solution (n_i), and the ion valency (z_i). As shown in this equation, the Debye length extends with the temperature, while conversely, shortens with the ion concentration. Overall, the total potential energy of interaction (2.1) of two planar sheets is then summarized by equation (2.5). This is the classical explanation of colloidal stability and provides a fundamental understanding of colloidal behaviours in a dispersion system.

$$E_{tot} = 4A\varepsilon_r\varepsilon_0\kappa\zeta^2 e^{-\kappa D} - \frac{A\pi\rho^2 C}{2D^4} \quad (2.5)$$

2.2.2 Zeta potential

The zeta potential (ζ) is defined as the electrical potential at the slipping plane outside the surface of a charged particle (**Figure 5**). Moving away from the surface of the charged particle (surface charge), a compact layer of strongly bound counterions surrounds the particle (Stern layer), while the next diffuse layer consists of weakly bound ions that still move with the particle within a boundary (slipping plane). The magnitude of the electrical potential at the slipping plane can be measured using electrophoresis.

$$\zeta = \frac{\mu_e 3\eta}{2\varepsilon_r\varepsilon_0 f(\kappa\alpha)} \quad (2.6)$$

In this equation, the zeta potential, ζ , is related to the electrophoretic mobility (μ_e) of the colloidal particles, the viscosity (η) of the solution, over the relative permittivity of the solution and free space ($\varepsilon_r\varepsilon_0$), respectively. Depending on the Henry function ($f(\kappa\alpha)$), which is the relationship between the particle size (α) and the inverse of the Debye length (κ), either the Hückel approximation ($\kappa\alpha = 1$) or the Smoluchowski approximation ($\kappa\alpha = 1.5$) is used.

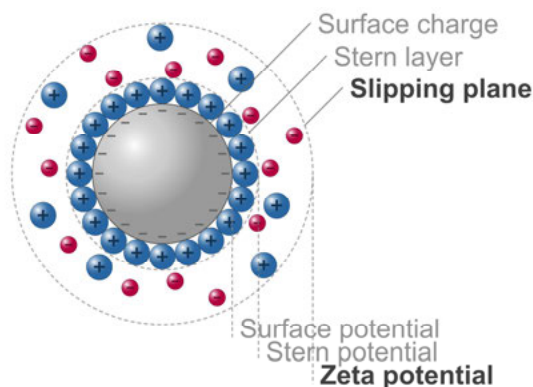


Figure 5. Schematic diagram of the zeta potential for a particle with a negatively charged surface (grey) surrounded by positive ions (blue) and negative ions (red) that move with the particle as one entity.

2.2.3 Surface modifications

A wide range of attractive forces and intermolecular interactions come into play when graphene is introduced into an aqueous phase. Since graphene is incapable of forming hydrogen bonds with water, the water molecules attempt to rearrange themselves around the graphene sheets in the most energetically favourable configuration without giving up hydrogen bonds. The water structuring at the graphene-water interface becomes more ordered, thus leading to a decrease in entropy. This phenomenon is generally termed the hydrophobic effect[73]. Consequently, the graphene sheets are forced close to each other and the van der Waals forces acting between two graphene surfaces induce restacking of the graphene sheets via π -bonds, thus leading to graphene aggregation. To prevent graphene aggregation in water, the graphene sheets in the dispersion require an energy barrier to overcome these attractive forces. This energy barrier can be introduced by either electrostatic repulsion, steric hindrance, or in most cases, the combination of the two interactions[74]. This can be realized by functionalization of the graphene sheets via covalent or non-covalent interactions[75,76]. The covalent functionalization involves a chemical reaction with the sp^2 -hybridized carbon atoms of graphene, thus compromising the π -system and the electronic properties of the graphene. In contrast, the non-covalent functionalization is based on the adsorption of molecules on the graphene surface, thus preserving the π -system and consequently the graphene properties. The π -system of graphene can establish a variety of π -complexes with other molecules (nonpolar gas- π , H- π , π - π , anion- π , and cation- π)[75]. In general, the non-covalent functionalization by π - π interactions, hydrophobic interactions, and van der Waals forces in the aqueous graphene dispersions are the most relevant and discussed

interactions in the literature. The type of stabilization mechanism needed can be tailored based on the intended applications and the end-uses of graphene.

π — π interactions

The precise nature of π — π interactions is ongoing debate due to the complex interplay between dispersive and electrostatic interactions[77–79]. The concept is used to describe the non-covalent interaction between molecules with unsaturated aromatic rings. This type of interaction can occur in different orientations, such as stacked (π — π) or perpendicular (CH— π). The perpendicular orientation can arise with another graphene sheet with hydrogen-terminated edges or other aromatic systems. A wide range of systems is capable to interact with graphene via π — π interactions, such as FMN[33], SDBS[21], and DNA[80]. By far the most common systems are polycyclic aromatic hydrocarbons (PAH)[81]. Among the PAHs, pyrene derivatives with a body comprising four aromatic rings and a charged functional head group have been explored to facilitate strong π — π interactions with graphene. The strength of the π — π interactions was found to increase with the electronegativity of the functional head group[82] and the chain length[83].

hydrophobic interactions

The hydrophobic nature of graphene is also an ongoing debate[84] and has been challenged in the past based on the wetting transparency[85], the effect of airborne contaminants[86], and the thickness-dependent behaviour[87]. In general, graphene is widely described with a hydrophobic character that has been utilized to facilitate the interaction with other molecules that contain hydrophobic components (**Figure 6**). For instance, surfactants are amphiphilic molecules comprising both a hydrophobic body and a hydrophilic head group. This means they like both a polar and a nonpolar environment. Surfactants are defined as surface-active agents that reduce the free energy of surfaces and interfaces. In an aqueous solution, the surfactants self-assemble at the water/air interface and form tightly-packed structures, thus lowering the surface tension of water[88]. Therefore, surfactants can adsorb onto the graphene surface with their hydrophobic part and extend towards the aqueous phase with the other hydrophilic part, thus improving the wetting of graphene in water as well as overcoming the attractive forces by electrostatic repulsion, steric hindrance, or the combination. There is a wide range of commercially available surfactants with varied chemical structures and dispersion efficiency. For long alkyl-chained SDS[25], SDBS[22], and CTAB[27], a longer surfactant chain length contributes to stronger van der Waals and hydrophobic interaction with graphene, and therefore a higher dispersion efficiency[89]. Furthermore, an additional aromatic ring on the alkyl chain can

improve the dispersion further via the π – π interactions[26,33]. For surfactants with a planar structure, such as bile salts, the achievable graphene concentration is in the following order: SC (0.52 mg ml⁻¹), SDC (2.58 mg ml⁻¹), and STC (7.1 mg ml⁻¹). The higher dispersed graphene concentration by the SDC and STC is attributed to the absence of one oxygen functional group on the basal plane[23], and a higher effective charge density on the head group of the STC[24]. Surface modification of the graphene surface with surfactants of a high charge density can provide a greater electrostatic repulsion between the sheets, thus improving the stability by overcoming the van der Waals forces. For biopolymers extracted from biomass, the stabilization mechanism is an ongoing investigation, and more understanding is needed. In addition to starch (**Paper II and III**), several other biopolymers have been demonstrated as dispersing agents, such as cellulose[90], gum arabic[91], and chitosan[41]. Among polysaccharides, starch and cellulose share the same monomer unit (glucose) and differ only in the glycosidic bonding between repeated units. In general, polysaccharides can have a hydrophobic-hydrophilic nature as well[92]. The hydrophobicity originates from the enriched C—H groups, while the hydrophilicity from the O—H group[93]. Moreover, a dense packing of polysaccharides chains can conform into 3D structures with hydrophobic-hydrophilic domains[94]. In addition, polysaccharides can be modified into an ionic character and induce dipole moment with graphene and establish electrostatic interactions[42]. For starch polysaccharides specifically, the linear amylose tends to coil into a helix with a hydrophilic shell and hydrophobic core that can form inclusion complexes with hydrophobic particles[95,44].

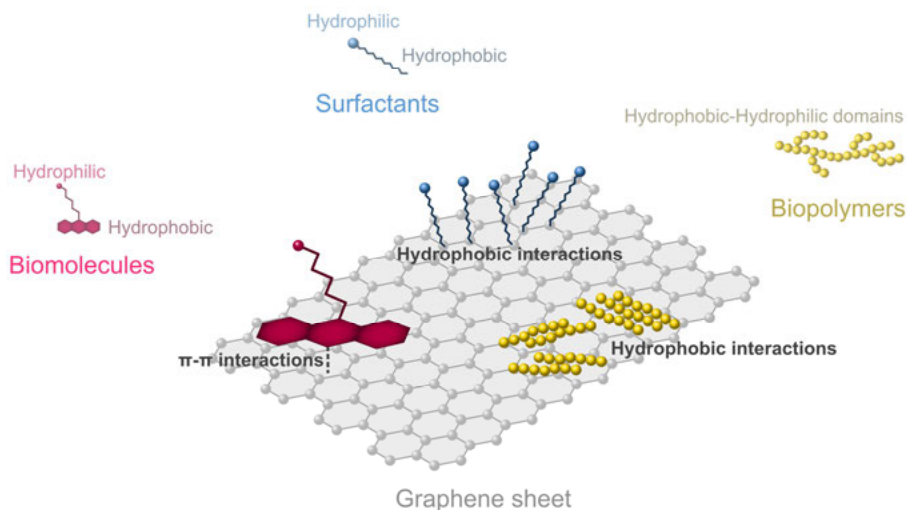


Figure 6. Schematic illustrations (not to scale) of the conformation and stabilization mechanism of amphiphilic biomolecules (red), surfactants (blue) and biopolymers (yellow) on the surface of a graphene sheet (grey).

2.3 Graphene applications

2.3.1 Gas barriers

The gas permeation through a film can be understood and predicted by the solution-diffusion model based on Fick's first law of diffusion and Henry's law of solubilities. In 1803, William Henry described that the amount of dissolved gas, under thermodynamic equilibrium, is proportional to the partial pressure of that gas[96]. A few decades later in 1855, Adolf Fick described that the diffusion flux of a gas is proportional to the concentration gradient and moves from the high concentration region to the low concentration region[97]. Combining these two principles, this solution-diffusion model suggests that the gas permeation process through a film involves five consecutive steps (**Figure 7**):

1. Diffusion of the gas towards the film.
2. Adsorption of the gas at the high-pressure atmosphere/film interface.
3. Diffusion of the gas inside the film.
4. Desorption of the gas at the film/low-pressure atmosphere.
5. Diffusion of the gas away from the film.

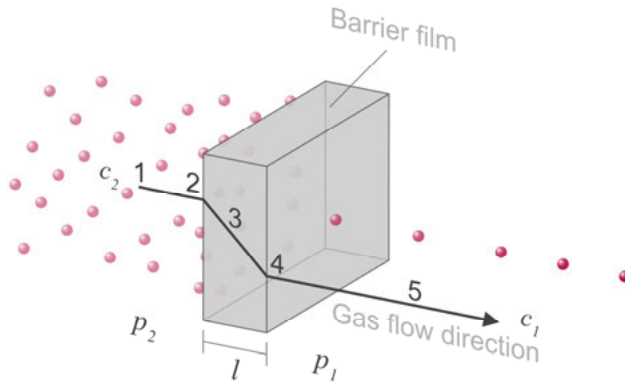


Figure 7. Solution-diffusion model of gas permeation through a single film.

Among these processes, the gas diffusion inside the film (step 3) is the rate-determining step that defines the barrier performance of the film. Once a gas is diffusing inside the film, the equation (2.7) describes the diffusive flux (J) of that gas as a function of the amount (Q) passing through an area (A) over time (t).

$$J = \frac{Q}{At} \quad (2.7)$$

According to Fick's first law, the diffusive flux (J) of the gas is proportional to the concentration gradient ($\partial c/\partial x$) inside the film with a fixed thickness (l). The diffusion coefficient (D) is a proportionality constant for each material in the film and is assumed constant for thin films.

$$J = -D \frac{\partial c}{\partial x} \quad (2.8)$$

Integrating the concentration (c) across the film thickness in equation (2.8).

$$J = D \frac{c_2 - c_1}{l} \quad (2.9)$$

The diffusive flux, J , in equation (2.7) and (2.9) can be combined.

$$\frac{Q}{At} = D \frac{c_2 - c_1}{l} \quad (2.10)$$

For gases, the concentration, c , is replaced by pressure (p). According to Henry's law, the concentration of a gas is related to the solubility coefficient (S) and partial pressure of the gas (p).

$$c_n = Sp_n \quad (2.11)$$

Insert Henry's law into equation (2.10).

$$\frac{Q}{At} = DS \frac{p_2 - p_1}{l} \quad (2.12)$$

The product of DS is equal to the gas permeability (P), which can be determined experimentally by measuring the amount of permeated gas over time. This solution-diffusion model assumes that the gas diffusion inside a single film is in a steady-state condition and takes place in one direction.

$$DS = \frac{Ql}{At(p_2 - p_1)} \quad (2.13)$$

$$P = \frac{Ql}{At\Delta p} \quad (2.14)$$

The inherent barrier properties of most polymer films are mainly associated with tortuous pathways from the structural features inside the film (**Figure 8**), such as crystallinity, morphology, and orientation[98]. However, many commonly used polymers in the packaging industry are semicrystalline with amorphous domains that allow gas permeation (**Figure 8a**), hence will function poorly as gas barriers by themselves[99]. Therefore, when graphene sheets, as an impermeable filler, is incorporated uniformly into the polymer matrix, tortuous pathways are formed (**Figure 8b**), thus improving the overall gas barrier properties of the film. On the contrary, when the incorporated graphene sheets are aggregated, the improvement is limited (**Figure 8c**). When incorporating graphene sheets, the relevant factors contributing to the extended tortuosity are mainly the aspect ratio (lateral size over thickness) and the orientation (relative to the film plane)[13]. However, the prerequisite to obtaining these structural features is a stable graphene dispersion that is compatible with the polymer matrix. To meet this prerequisite, a fundamental understanding of the surface chemistry of graphene is key.

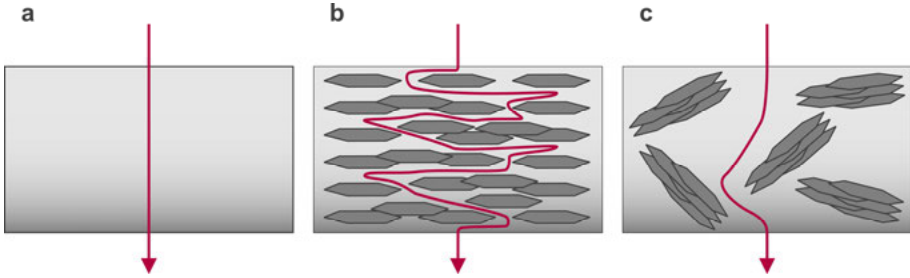


Figure 8. The gas barrier performance is dependent on the permeation pathways within films. **a** A polymer film without filler. **b** A polymer film incorporated with compatible and uniformly distributed graphene sheets **c** A polymer film with graphene aggregates.

2.3.2 Conductive inks

To formulate inkjet printable conductive inks, the physical and rheological properties must satisfy the requirement of fluid flow for a fixed nozzle diameter[100,101]. The inverse Ohnesorge number, equation (2.15), is used to predict the drop formation and jetting behaviour during printing[100].

$$Z^{-1} = O_h = \frac{\sqrt{W_e}}{R_e} \quad (2.15)$$

$$R_e = \frac{v\rho d}{\eta} \quad (2.16)$$

$$W_e = \frac{v^2\rho d}{\gamma} \quad (2.17)$$

The value of the Z^I is related to the dimensionless Reynolds number (R_e) and Weber number (W_e). The R_e is the ratio between the inertia and the viscous force, while the W_e is the ratio between the inertial force over the surface tension. To generate stable drop formation, the ink should have a certain drop velocity (v) and density (ρ). The most relevant parameters to adjust are the viscosity (η) and the surface tension (γ). In addition, the particle size of the graphene sheets also has an impact on printability and could block the nozzles when too large. As a figure of merit, the ink droplet is stable and printable when the ink formulation is within the range $1 < Z < 10$ [102], known as the parameter space of inkjet printable fluids. Inks with a Z value within this space is considered inkjet printable, while a value outside can lead to unwanted phenomena, such as splashing on the substrate or satellite drop formation[103]. Furthermore, when either the viscosity is too high or the surface energy is too low, the droplet breakup cannot occur.

3 Experimental methods

3.1 Chemicals and materials

3.1.1 Graphene powders

Graphene

The graphene powders used in this thesis work were commercially available graphene in two grades, industrial grade (product number AV-70-1-2.5i) and research grade (product number AV-70-1-1.5). The industrial grade is mass-produced graphene with lower tolerance on the characterization control, while the research grade, in contrast, is the high-end graphene suitable for research and development (**Figure 9**). These grades are classified by the graphene lateral size (70 μm), average thickness (1 nm), and oxygen content (1.5-2.5 at%). All graphene powders were purchased from Avanzare Innovacion Technologica SL.



Figure 9. Graphene powder from a typical grade (AV-70-1-1.5) and the chemical structure of graphene.

3.1.2 Bio-based dispersing agents

Flavin mononucleotide

The FMN is a naturally occurring biomolecule derived from riboflavin (vitamin B2) via the catalytic activity of the enzyme (riboflavin kinase). In nature, FMN is commonly associated with flavoenzymes as a cofactor that

takes part in vital biological processes, such as photosynthesis, aerobic respiration, denitrification, and sulphur respiration[104]. In the European Union, FMN is commonly used as an orange-red colour additive designated as E101a. The chemical structure of FMN comprises an isoalloxazine aromatic ring system (hydrophobic) and a phosphorylated head group (hydrophilic), thus making the FMN amphiphilic (**Figure 10**). The amphiphilic character of this biomolecule makes FMN function as a dispersing agent for graphene in water. In this thesis work, riboflavin 5'-monophosphate sodium salt hydrate was purchased from Sigma-Aldrich (product number F6750).



Figure 10. FMN powder and the chemical structure of FMN with an isoalloxazine ring system.

Starch

Starch is one of the most abundant biopolymers and has been industrially extracted from plant-based sources on large scale for decades. The abundant, biodegradable, and renewable nature of starch makes it attractive as both dispersing agent and polymer matrix in composite film formulations. The starch chemical structure is composed of two types of polysaccharides, amylose and amylopectin (**Figure 11**). The amylose is a linear polysaccharide chain composed of repeating D-glucose units that are joined by glycosidic α -1,4 links. The amylopectin is a branched polysaccharide chain with double-helical side chains that are joined to the main chain by glycosidic α -1,6 links. The composition of amylose and amylopectin is responsible for the semi-crystalline nature of the starch granule. In this thesis work, unmodified native corn starch powder with 23% amylose and 73% amylopectin was purchased from Sigma-Aldrich (product number S4126).

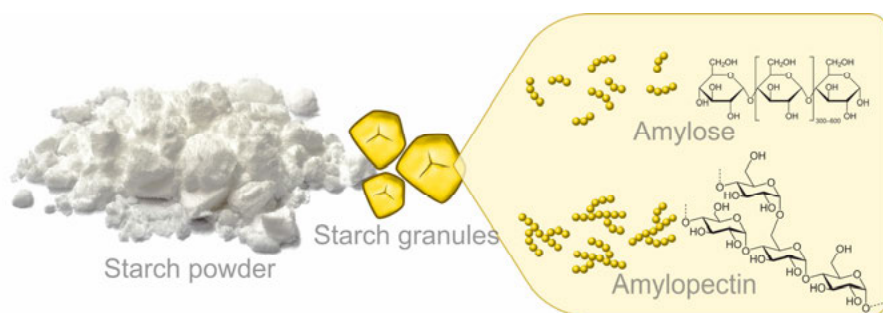


Figure 11. Native corn starch powder. The granules mainly consist of two types of polysaccharides: amylose (linear chain) and amylopectin (branched chains).

3.2 Aqueous graphene dispersions and composites

3.2.1 Preparation of aqueous graphene dispersions

The aqueous FMN-graphene dispersion was developed for fundamental studies of the molecular interaction between FMN and graphene (**Paper I**). The FMN molecule was treated as an amphiphilic dispersing agent for dispersing graphene in water and used as received (**Figure 12**). In general, FMN powder (10 mg) was first dissolved in Milli-Q water (10 mL) to obtain an aqueous FMN solution (1 mg mL^{-1}). Then graphene powder (5 mg, AV-70-1-2.5i) was mixed in the FMN solution. The aqueous suspension of FMN-graphene was processed by ultrasonication using a Vibra-Cell VCX 750 processor (Sonics, US) with a solid probe (tip diameter 6 mm, amplitude 40%) under cooling for 6-9 min to disperse the graphene powder. To remove excess FMN molecules, the aqueous FMN-graphene dispersion was subjected to ultracentrifugation using an Optima L-90K (Beckman Coulter, US) at 13,000-14,000 rpm for 20 min. The top 75% supernatant was discarded, while the resulting sediment of FMN-graphene sheets was re-dispersed in water to obtain a purified FMN-graphene dispersion with a minimal amount of the FMN. The FMN-graphene dispersion was stored at room temperature when not in use. To optimize the FMN-graphene dispersion (**Paper I**), a set of ten FMN-graphene suspensions was prepared with a fixed amount of starting graphene powder (0.5 mg) and varied FMN (0.1, 0.2, 0.3, 0.4, 0.5, 1.0, 2.0, 3.0, 4.0, 5.0 mg) in water (5 mL). Each suspension was processed by ultrasonication via the same probe design for 5 min to disperse graphene. The dispersed graphene concentration was evaluated by UV-vis spectroscopy. The starting mass ratio condition was determined based on dispersion with the highest graphene concentration. Then with the selected mass ratio, an aqueous FMN-graphene suspension was prepared accordingly, and the graphene

concentration was further investigated with sonication time between 0-18 min. Finally, the colloidal stability was evaluated by observing the sedimentation over time.

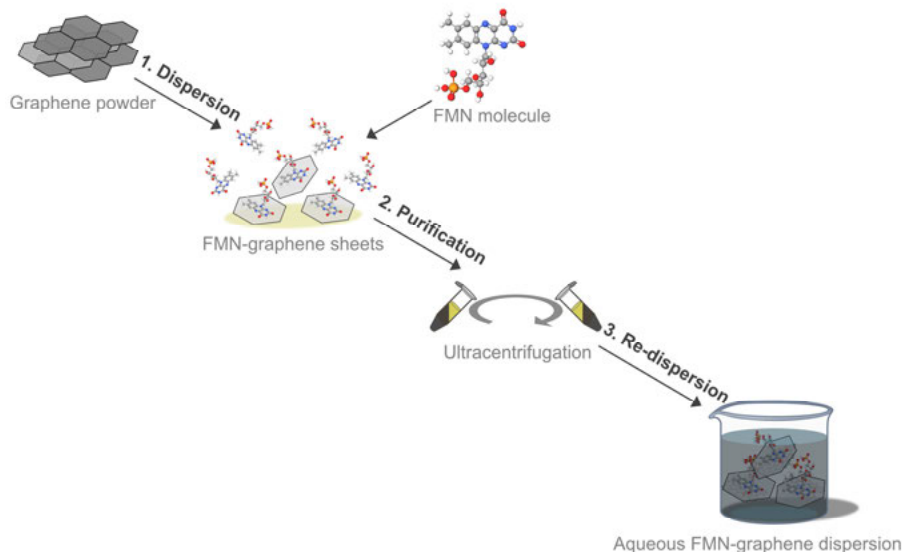


Figure 12. The dispersion process of the aqueous FMN-graphene dispersions (**Paper I**).

The aqueous SNP-graphene dispersion was first developed for fundamental studies of the starch-graphene interaction (**Paper II**), and then further customized for gas barrier applications (**Paper III**) and inkjet printing (**Paper IV**). To obtain SNPs as a dispersing agent for dispersing graphene in water, the starch powder was first pre-treated by a two step-process involving gelatinization and ultrasonication (**Figure 13**). The preparation principle is based on extracting the starch polysaccharides within the starch granules. In general, starch powder (0.1 or 3 g) was added to Milli-Q water (10 or 50 mL) in a glass bottle. To gelatinize the starch granules, the aqueous suspension of starch was heated in the glass bottle with a tightly sealed screw cap at 95 °C for 20 or 30 min under constant magnetic stirring at 1000 rpm. To form SNPs as well as lower the viscosity efficiently, the gelatinized starch was transferred to a narrow cylindrical glass vial and treated by ultrasonication using a Vibra-Cell VCX 750 processor (Sonics, US) with a larger solid probe (tip diameter 13 mm, amplitude 50%) for 3 min to obtain an aqueous SNP solution. Then graphene powder (5 or 150 mg, AV-70-1-1.5) was mixed in the SNP solution. The SNP-graphene mixture was processed by ultrasonication via probe under cooling for 30-60 min. Finally, residual graphene powder or impurities in the resulting SNP-graphene dispersion were removed by centrifugation at 1000 rpm for 10 min. The resulting SNP-graphene dispersion was stored at room

temperature when not in use. For the aqueous SNP-graphene dispersions (**Paper II** and **III**), the amount of graphene was fixed (5 mg), while varying the starch (5, 50, 100, 150, and 200 mg) in water (10 mL). Each suspension was processed by ultrasonication via the same probe design for 10 min. The dispersed graphene concentration was evaluated by UV-vis spectroscopy. Based on the selected mass ratio, an aqueous FMN-graphene suspension was prepared accordingly, and the graphene concentration was further investigated with sonication time between 0-60 min. The colloidal stability was evaluated by UV-vis spectroscopy over time.

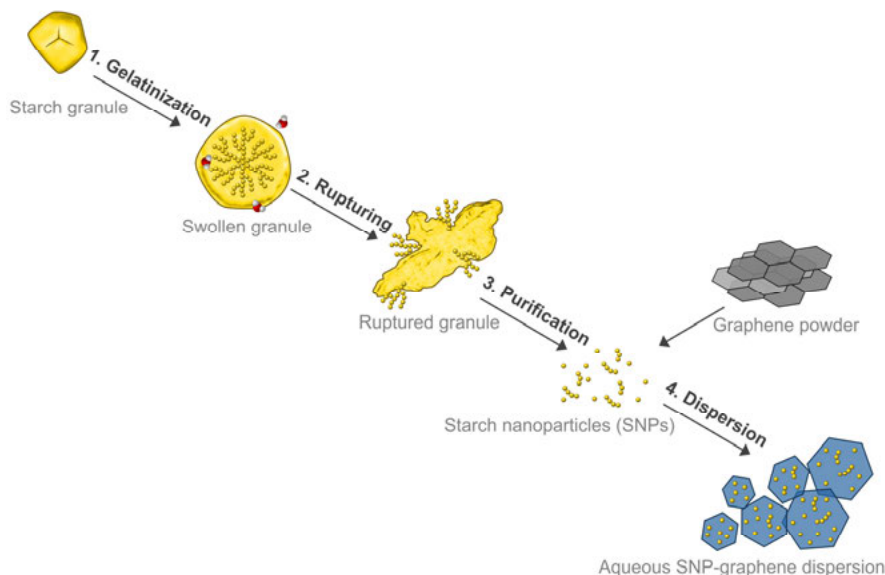


Figure 13. The dispersion process of the aqueous SNP-graphene dispersions (**Paper II**).

3.2.2 Fabrication of graphene composite films

The starch/SNP-graphene composite films for gas barrier applications (**Paper III**) were prepared by solution deposition of a formulation comprising the SNP-graphene dispersion (filler) and a starch gel with sorbitol (polymer matrix) (**Figure 14**). To overcome the brittleness of starch films, a sugar alcohol molecule sorbitol was added to the starch matrix as a plasticizer. For the starch matrix, the starch:sorbitol mass ratio was fixed at 5:3. In general, starch powder (1.95 g) and sorbitol powder (1.17 g) were dissolved in water (50 mL) and heated at 95 °C under constant stirring at 1000 rpm for 30 min. This gelatinized starch gel was drop-cast into petri dishes (8 mL/dish) and then dried under ambient conditions at 25 °C to form starch films for reference. For the starch/SNP-graphene composite films, the sorbitol content was adjusted

based on the total starch in the final film to maintain the plasticization. For instance, the composite film formulation (64 mL) of 8 film replicates with the highest graphene content (3.0 wt%) was prepared by mixing the SNP-graphene dispersion (40 mL) of graphene (0.12 g) and SNPs (2.40 g) to the starch matrix (24 mL) of starch (0.03 g) and sorbitol (1.46 g). Similarly, a series of starch/SNP-graphene films (0.75 wt%, 1.5 wt%, and 3.0 wt%) were prepared by the same approach. After the drying process, all the final films had a consistent weight (0.5 g) and a fixed diameter of 8.5 cm.

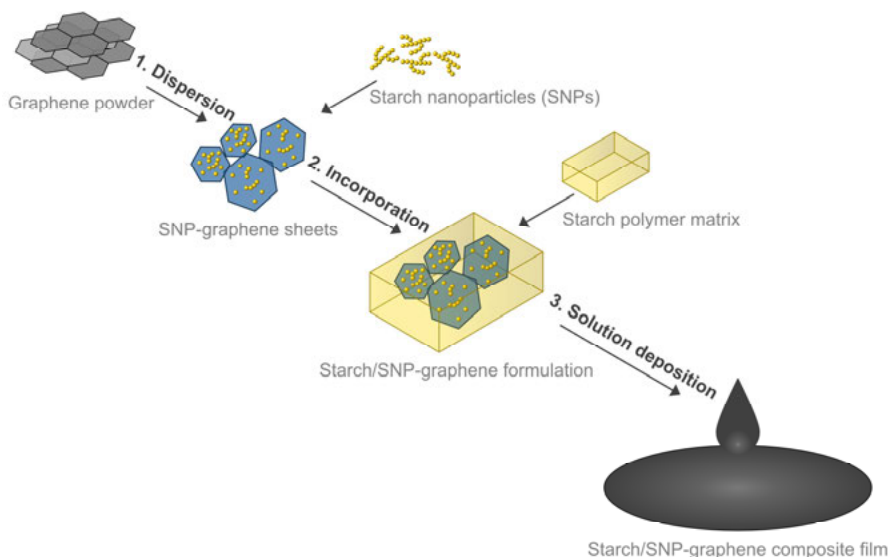


Figure 14. The fabrication process of the starch/SNP-graphene composite films for barrier applications (**Paper III**).

3.3 Characterization techniques

3.3.1 Spectroscopic analysis

Graphene concentration and colloidal stability

UV-vis spectroscopy measures the intensity of light absorbed by a sample in the UV region (200-400 nm) and the visible region (400-900 nm), or in other words, the intensity of light transmitted through the sample (**Figure 15**). This technique is commonly used for the identification and quantification of particles in a solution. When the light of different wavelengths interacts with a particle, the energy from the photons (inversely proportional to the wavelength) can promote electrons of that particle from their ground state to

an excited state, thus resulting in an absorption. Since different particles can have a varied magnitude of discrete electronic energy levels, the absorption is only permitted when the electronic transition matches the specific irradiated wavelength, thus providing useful information in the absorption spectrum. For aqueous graphene dispersions, the UV-vis absorption spectrum provides information that can be related to the dispersed graphene concentration[21], dimension[105], and electronic conjugation level[106]. In this thesis work, the UV-vis absorption of the graphene dispersions was measured between 200-800 nm using a UV-vis spectrophotometer Lambda 650 (PerkinElmer, US). In general, the graphene dispersions were diluted by a factor of 100 and equilibrated for 1 min prior to measurement. The aliquots used for the dilutions were extracted from the top (surface) of the graphene dispersions. The measured optical absorbance in the visible region at 660 nm was selected to calculate the dispersed graphene concentration. The graphene concentration is related to the changes in the intensity of the absorbed light as given by equation (3.1) and can be written as in equation (3.2), known as the Beer-Lambert's law.

$$A = -\log_{10} T = -\log_{10} \frac{I}{I_0} \quad (3.1)$$

$$A = \alpha cl \quad (3.2)$$

In this equation, the absorbance (A) is directly proportional to the attenuation coefficient (α), concentration (c), and the light path length (l). The attenuation coefficient, α , is unique for each aqueous dispersion system and can be determined experimentally. In addition, the variation in the graphene concentration via the absorbance over time was also applied as an indication of the colloidal stability.

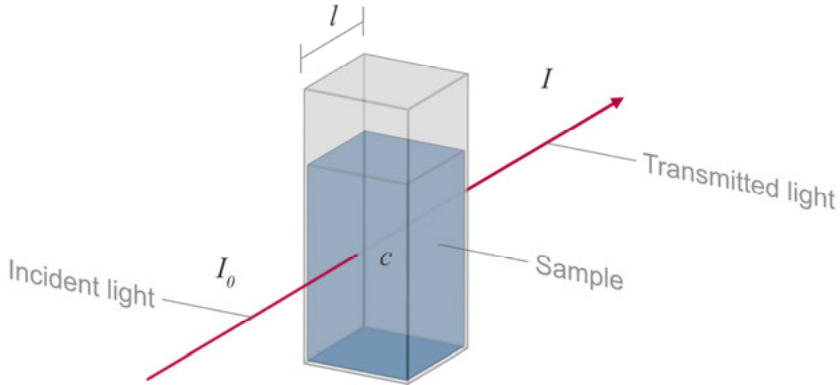


Figure 15. The intensity of an incident light (I_0) that is absorbed (I) by a sample is directly proportional to the concentration of the sample (c) and the path length (l).

Particle size

Laser diffraction-based particle size analysis is a technique that can measure particle size distributions over a wide range from 10 nm up to 3.5 mm. To measure across such a wide range, a sequential combination of measurements is performed with a red laser (4 mW, He-Ne, 632.8 nm) and a blue laser (10 mW, LED, 470 nm). When a laser beam interacts with particles, the incident beam scatters with varied angles and intensities depending on the particle size, thus producing a diffraction pattern at the focal plane detector (**Figure 16**). The scattering angle relative to the incident beam is inversely proportional to the particle size. The particle size is described by the concept of the diameter of an imaginary sphere with equivalent volume. In this thesis work, the particle size analysis was performed using a Mastersizer 3000 instrument with a Hydro SV measurement cell (Malvern, UK). The volume-weighted particle size distributions were calculated by the instrument software using the Mie theory of light scattering. For this purpose, the refractive index and the absorption for graphene were 2.73 and 1.36, respectively, while for starch 1.53 and 0.01, respectively.

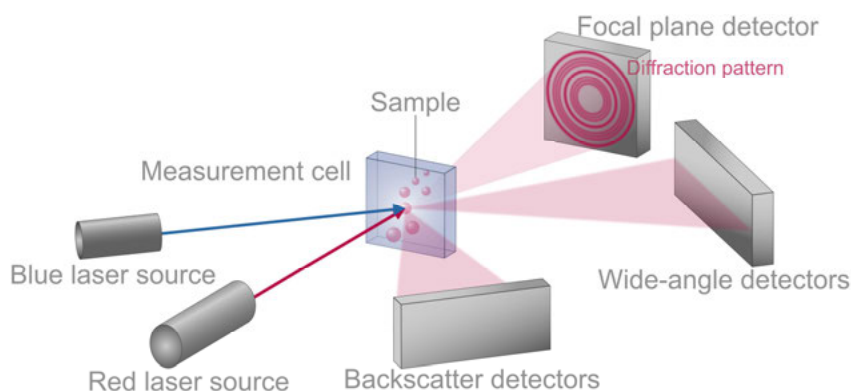


Figure 16. As light travels through the measurement cell and interacts with the particles, the intensity of scattered light associated with the particles size is measured by a series of photosensitive detectors at different positions and then interpreted by mathematical models.

Molecular interactions

Fourier-transform infrared spectroscopy (FT-IR) measures infrared absorptions associated with molecular vibrations in a sample, such as specific chemical bonds or functional groups. In the attenuated total reflectance (ATR) mode, a sample is placed in contact with an optically dense crystal (**Figure 17**). When an incident IR light is reflected internally at the interface between the crystal and the sample, an electric field (evanescent wave) extends into the sample and become absorbed by the vibrations in the sample close to the

surface. The penetration depth of the evanescent wave is typically 1-3 μm . In this thesis work, FT-IR spectra of the aqueous graphene dispersions and the composite films were obtained using an FT-IR spectrometer Spectrum One in the ATR mode (PerkinElmer, US). For each sample, 16 scans were collected at a resolution of 4 cm^{-1} and then averaged. Data processing and analysis, such as baseline corrections and deconvolutions, were performed in OriginPro 2020 software.

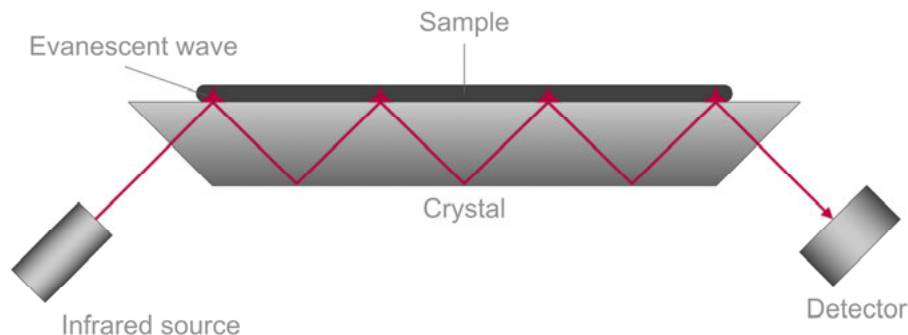


Figure 17. Infrared light interacts with a sample via an evanescent wave that extends into the sample, whereby the infrared carries chemical information to the detector.

Graphene quality and chemical composition

Confocal Raman spectroscopy is a versatile imaging technique that has become an integral part of the graphene research community. In 1928, Chandrasekhara Venkata Raman first described the discovery of inelastic scattering of light from chemical bonds of molecules, later known as the Raman effect[107]. When an incident light interacts with molecules, the vibrations in the chemical bonds cause specific energy shifts in the backscattered light (**Figure 18**). These shifts result in defined Raman spectra that provide chemical information of the investigated sample. For graphene samples, the characteristic Raman peaks are 1350 cm^{-1} (D peak), 1580 cm^{-1} (G peak), and 2700 cm^{-1} (2D peak)[108]. Among these peaks, the D peak is related to the breathing mode of aromatic carbon rings and require a disorder to become active. The G peak is related to the in-plane stretching of the carbon atoms. This peak is therefore a common feature for all sp^2 -hybridized carbon allotropes. Finally, the 2D peak is the overtone of the D peak and does not require any disorders to be activated[109]. In this thesis work, the Raman measurements of graphene sheets and graphene composite films was performed using a WITec alpha300 confocal Raman system (WITec GmbH, Germany) with an excitation wavelength of 532 nm and a low laser power of 2.5 mW. The obtained spectra were corrected for cosmic ray noise and then averaged in the WITec Project 5.1 software. Furthermore, baseline corrections and deconvolutions were performed in the OriginPro 2020 software.

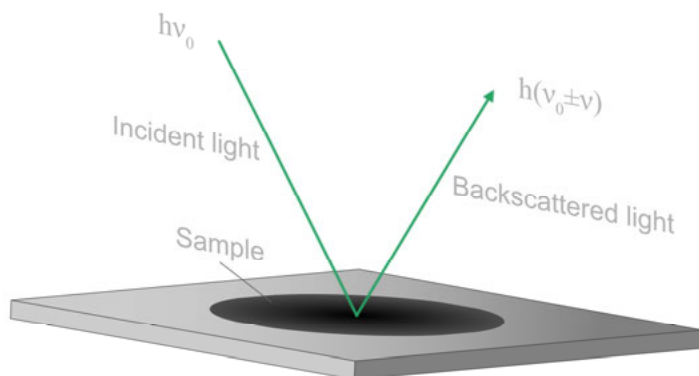


Figure 18. The Raman effect is the interaction of incident light ($h\nu_0$) with the chemical bonds within a sample that results in backscattered light with a specific energy shift ($h\nu_0 \pm \nu$).

3.3.2 Microscopy imaging

Morphology and lateral size

Scanning electron microscopy (SEM) is an imaging technique that can provide morphological and compositional information of a sample with a resolution down to the nanoscale. The SEM employs a focused beam of electrons with high kinetic energy to scan the surface of the sample, whereby different types of scattered electrons from the sample are collected as a function of position by designated detectors (**Figure 19**). The obtained signals from the backscattered electrons, secondary electrons, or the combination of the two are then used to construct images. In the scanning transmission electron microscopy (STEM), the focused electron beam is transmitted through the sample and collected by detectors at different angular regions, such as the bright-field (BF), the dark-field (DF), and the high-angle annular dark-field (HAADF). At wider angles, the intensity becomes proportional to the atomic number, thus providing higher contrast between elements. In this thesis work, the morphology of graphene sheets and the cross-section of graphene composite films were investigated by a Quanta 250 FEG operated in SEM and STEM mode (FEI, US), respectively. For the graphene sheets, a dilution of the aqueous dispersion was spin-coated on Si/SiO₂ substrates for the SEM analysis, while drop-cast on copper grids for the STEM. For the cross-section analysis of the films, the films were mechanically cleaved after immersion in liquid nitrogen and then attached to carbon tapes.

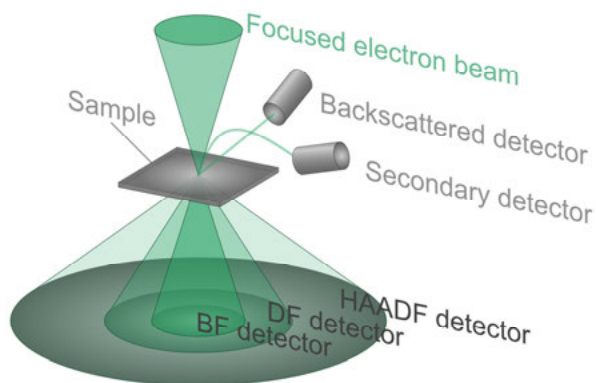


Figure 19. For SEM imaging, a focused beam of electrons is scattered from the surface of a sample and then collected by detectors (backscattered and secondary). For STEM imaging, the focused electron beam is transmitted through the sample and then collected by detectors at varied angles (BF, DF, and HAADF).

Topography and height profile

The atomic force microscopy (AFM) is one of many scanning probe techniques that can provide topographical information of particles at the nanoscale. The AFM utilizes a fine tip on a cantilever to scan across the surface of a sample and probe the physicochemical interactions between the tip and the surface (**Figure 20**). In this thesis work, the topographical imaging of the graphene sheets was performed in the PeakForce tapping mode using a MultiMode 8 (Bruker, US). The cantilever ScanAsyst-Air (Bruker, US) with a nominal spring constant of 0.4 N m^{-1} and a nominal tip radius of 2 nm was used. The data analysis and processing were performed in Nanoscope Analysis 1.8 software (Bruker, US).

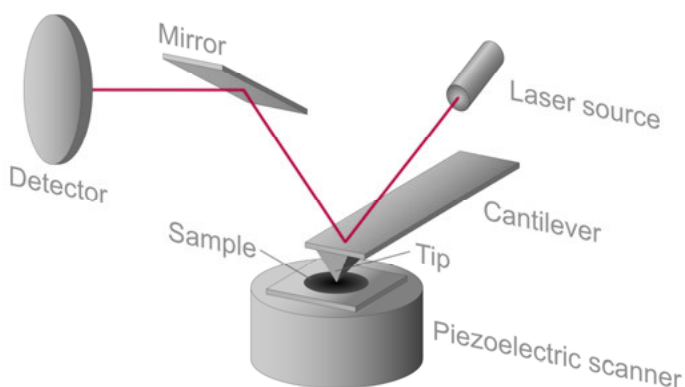


Figure 20. A focused laser beam detects the motions of the cantilever as a response of the interaction between the tip and the sample surface.

3.3.3 Surface charge and energy

Zeta potential

The zeta potential of colloidal particles in solution is a function of the electrical potential at the slipping plane. The magnitude of the electrical potential can be quantified by the electrophoretic mobility of the particles under an electric field. When under the electric field, each particle and its associated ions move as a single unit, whereby the electrophoretic mobility governs the velocity at which the particles travel between the electrodes (**Figure 21**). This velocity is independent of particle size or shape, and can therefore be measured by dynamic light scattering techniques. In this thesis work, the zeta potential was determined using a Zetasizer Nano ZS (Malvern, UK). In general, the graphene dispersion was diluted by 100-300 times to obtain a suitable graphene concentration range ($\sim 0.01 \text{ mg mL}^{-1}$). The dilutions were equilibrated in a folded capillary cell for 30 s prior to measurements. For each measurement, six replicates were recorded with a minimum of 20 runs and then averaged. The zeta potential was calculated using the Smulochowski approximation, given by equation (3.3).

$$\zeta = \frac{\mu_e \eta}{\epsilon_r \epsilon_0} \quad (3.3)$$

In this equation, the zeta potential (ζ) is related to the electrophoretic mobility (μ_e) of the colloidal particles, the viscosity (η) of the solution, over the relative permittivity of the solution and free space ($\epsilon_r \epsilon_0$), respectively.

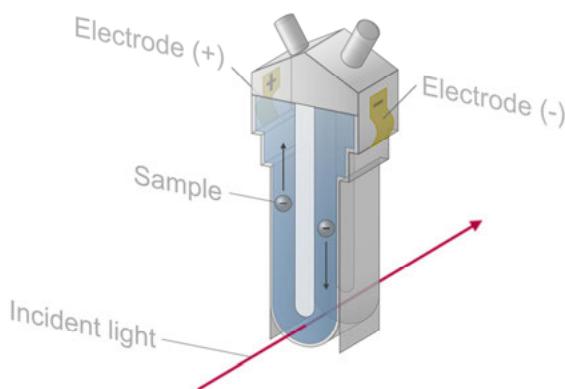


Figure 21. A folded capillary cell and the working principle of zeta potential. Negatively charged colloidal particles travel away from the negative electrode and towards the positive electrode when under an electric field. The velocity of the particles reflects the magnitude of the zeta potential.

Surface tension

Wilhelmy plate method is one of many tensiometer techniques to measure the surface tension of solutions. The working principle relies on measuring the force acting on a vertically suspended plate that is partially immersed into the solution (**Figure 22**). When the plate is in contact with the surface of the solution, the solution will adhere to the plate by a capillary effect and pull the plate downwards with a force that is recorded by a microbalance. The magnitude of this force is directly related to the surface tension, given by equation (3.4).

$$\gamma = \frac{F}{L \cos \theta} \quad (3.4)$$

In this equation, the surface tension (γ) is proportional to the pulling force (F) over the wetted plate length (L) and the contact angle (θ). For aqueous graphene dispersions, the surface tension provides information on the cohesive intermolecular forces in the dispersion system. In this thesis work, the surface tension was measured using the Wilhelmy plate method with a platinum plate at 25 °C (K100 Force Tensiometer, KRÜSS). In general, the platinum plate (19.9 mm x 10.1 mm x 0.2 mm) was partially immersed into the liquid for 300 seconds to reach a steady-state and then the last five measured values (out of 50) were averaged.

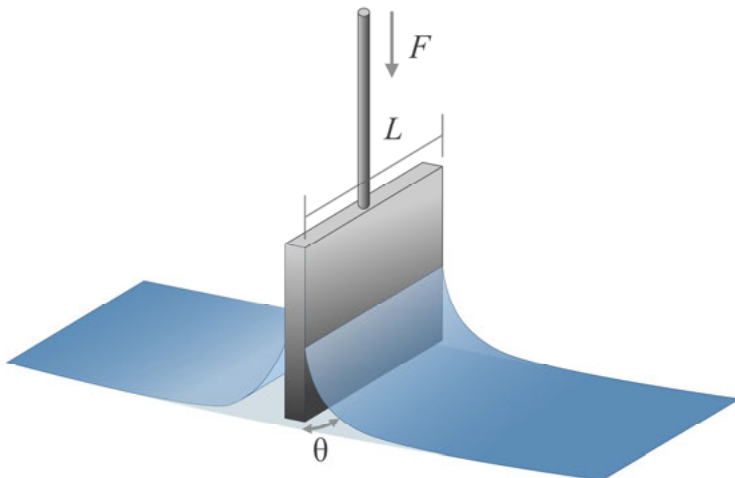


Figure 22. The working principle of the Wilhelmy plate method. The surface tension of aqueous dispersion systems is determined by the amount of force that is applied on the plate by the solution.

3.3.4 Thermal properties

Thermal stability and solid content

The thermogravimetric analysis (TGA) is a technique that measures the weight changes of a sample as a function of temperature under a controlled atmosphere (**Figure 23**). In general, the TGA systems can detect weight changes at a resolution of $0.1\ \mu\text{g}$ over the temperature range from ambient to $1600\ ^\circ\text{C}$, thus involving a relatively small sample size (2-50 mg). The obtained TGA curves can provide information on the aqueous graphene dispersions as well as the composite films, such as solid content, chemical composition, and thermal stability. Furthermore, the derivative thermogravimetric (DTG) curves (first derivative of the TGA curves) can provide additional information on the decomposition rate. The peak temperature in the DTG curves indicates the point at which the rate of weight loss is maximum, while the peak width can be used to calculate the stepwise weight loss of the dispersion system as well as compare the thermal stability between two components. In this thesis work, the TGA measurements were performed using a TGA 2 STARe System (Mettler-Toledo, Switzerland). In general, samples with a fixed amount (5 mg) were equilibrated in the oven at $105\ ^\circ\text{C}$ for 24 hours prior to measurements. The measurements were recorded in alumina crucibles with a volume of $70\ \mu\text{L}$ from $25\ ^\circ\text{C}$ up to $900\ ^\circ\text{C}$ at a constant heating rate of $10\ ^\circ\text{C}\ \text{min}^{-1}$. The selected atmosphere was either oxygen or nitrogen with a gas flow rate of $50\ \text{mL}\ \text{min}^{-1}$. Data processing and analysis, such as calculations of the decomposition steps and the residues, were performed in the STARe Evaluation software 16.0 (Mettler-Toledo, Switzerland).

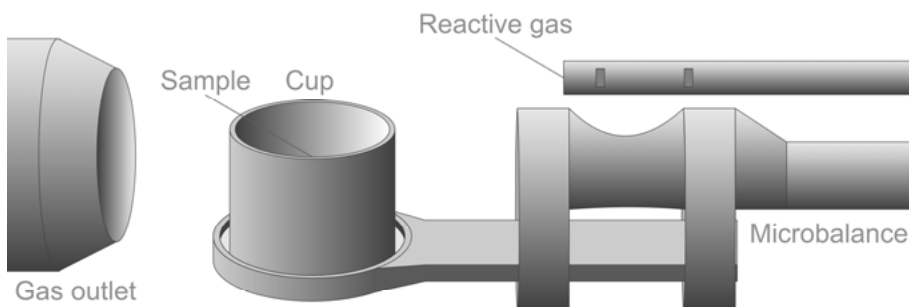


Figure 23. A TGA cup is filled with a sample and placed on a microbalance inside a high-temperature furnace under controlled conditions. The weight loss of the sample is recorded as a function of temperature by the microbalance.

3.3.5 Electrical properties

Sheet resistance and electrical conductivity

The four-point probe method is one of the most used techniques to measure the sheet resistance of composite films. This technique involves physical contact between the films and four co-linear probes that are equally spaced apart (**Figure 24**). To measure the sheet resistance, a direct current (I) is applied between the outer two probes, while a voltage drop (V) is measured between the inner two probes. For wide (lateral size \gg probe spacing (s)) and thin (thickness $\ll s$) films, the sheet resistance is then given by equation (3.5). The electrical conductivity (σ) can be determined via the sheet resistance (R_s) and the thickness (d) by the relation in equation (3.6).

$$R_s = \frac{\pi}{\ln 2} \left(\frac{V}{I} \right) \quad (3.5)$$

$$\sigma = \frac{1}{R_s d} \quad (3.6)$$

In this thesis work, the sheet resistance was measured using an Ossila four-point probe system (Ossila, UK). In general, two replicates per film with an area of $2 \times 2 \text{ cm}^2$ (**Paper IV**) or $5 \times 5 \text{ cm}^2$ (**Paper III**) were measured. The sample thickness was measured using an optical profilometer PLu neox (Sensofar, Spain).

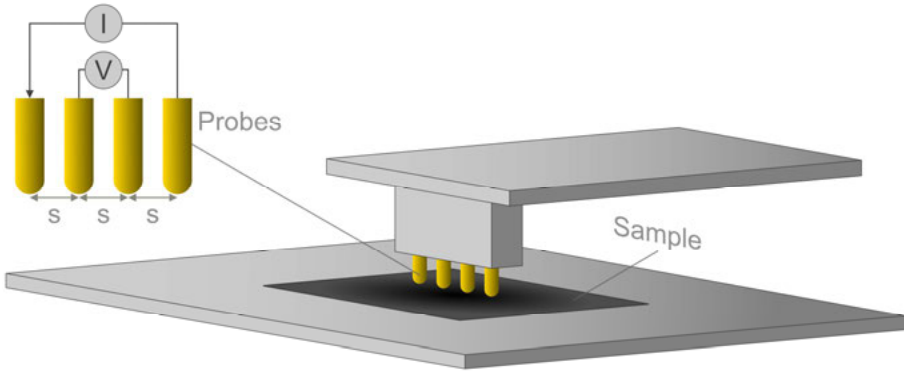


Figure 24. Four-point probe method and measurement setup on a composite film.

3.3.6 Gas barrier performance

Gas permeation

Gas permeation instruments can measure the amount of gas transmitted through a barrier film over time under controlled conditions based on various sensor techniques (**Figure 25**). For a gas barrier measurement, in general, the film is mounted inside a test cell between two chambers with different relative humidity (RH). On the feed side (high RH), the gas of interest is continuously fed. On the opposite permeate side (low RH), the gas of interest is continuously fed. On the opposite permeate side (low RH), gas permeant is detected by a sensor. The partial pressure difference between these two chambers drives the gas permeation from the high RH to the low RH. For the WVTR, the amount of transmitted water vapour over time is detected by an infrared sensor. For the OTR, the amount of transmitted oxygen gas over time is detected by a coulometric sensor. In this thesis work, the WVTR was measured using a MOCON PERMATRAN instrument (MOCON, US) according to the ISO 15106-1 standard, while the OTR was measured using a MOCON OX-TRAN instrument (MOCON, US) according to the ASTM F1927-14 standard. At least six replicates per composite film were measured for both the OTR and the WVTR measurements. The composite films were masked to reduce the test area down to 5 cm² and to prevent edge leakage. The test conditions were set to 23 °C with 50% RH or 80% RH, respectively.

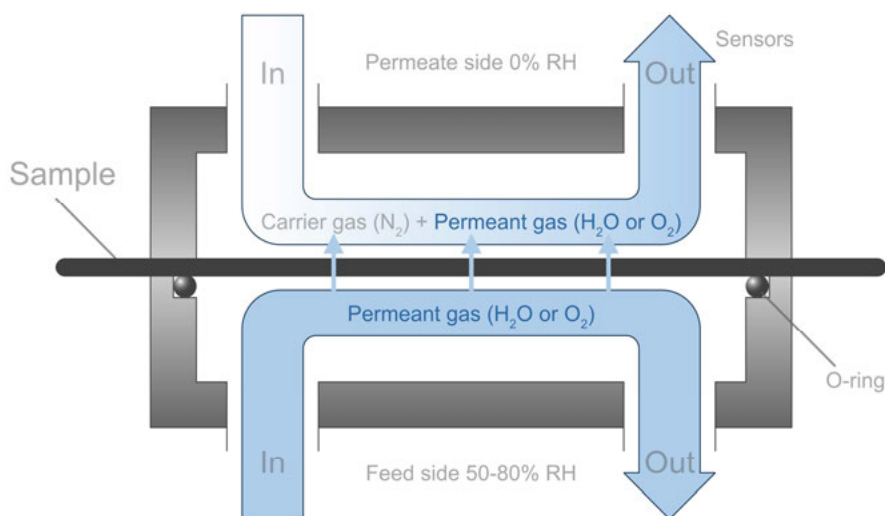


Figure 25. Schematic illustration of a general gas barrier measurement. The higher pressure at the feed side (typically 50-80% RH) drives the permeant gas (water vapour or oxygen) towards the permeate side (0% RH), whereby a carrier gas (N₂) transports the permeant gas to the sensor (infrared or coulometric).

Barrier parameters and units

Assuming steady-state condition, the equation (2.7) for the diffusive flux derived in chapter (2.3.1) is the same for the WVTR and the OTR. Equation (3.7) describes the amount of gas (Q) that has passed through an area (A) over time (t). For the WVTR, the amount of permeated gas through a film is reported as a weight. To obtain the permeance unit, the WVTR is normalized to the water vapour partial pressure across the film, according to equation (3.8). The water vapour partial pressure is a function of the vapour saturation pressure (S) at the test temperature multiplied by the RH difference between the feed side (RH_1) and the permeant side (RH_2). To obtain the WVP, the permeance is normalized to the film thickness (l), as shown in equation (3.9) and can be written as equation (3.10). These steps are summarized in the table below (**Table 1**).

Table 1. Water vapour gas barrier equations and units

Equations	Units	
$WVTR = J = \frac{Q}{At}$	$\text{g m}^{-2} \text{ day}^{-1}$	(3.7)
$Permeance = \frac{WVTR}{S(RH_1 - RH_2)}$	$\text{g m}^{-2} \text{ day}^{-1} \text{ kPa}^{-1}$	(3.8)
$WVP = Permeance \cdot l$	$\text{g } \mu\text{m m}^{-2} \text{ day}^{-1} \text{ kPa}^{-1}$	(3.9)
$WVP = \frac{WVTR}{S(RH_1 - RH_2)} \cdot l$	$\text{g } \mu\text{m m}^{-2} \text{ day}^{-1} \text{ kPa}^{-1}$	(3.10)

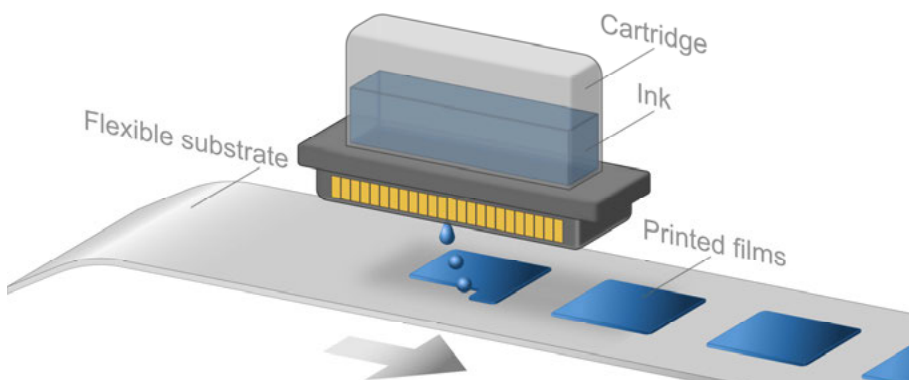
For the OTR, the amount of permeated oxygen gas through a film is reported as a volume. To obtain the permeance, the OTR in equation (3.11) is normalized to the oxygen partial pressure across the film, according to equation (3.12). In this equation, the oxygen partial pressure is the fraction of the permeant oxygen gas ($O_2\%$) multiplied by the total pressure including the atmospheric pressure at sea level ($P_{atm} = 101.3 \text{ kPa}$ or $\sim 1 \text{ atm}$), the partial pressure from water vapour ($P_{H_2O} = S \cdot RH_1$). To obtain the OP, the permeance in equation (3.13) is normalized to the film thickness (l) and can be written as equation (3.14). These steps are summarized in the table below (**Table 2**).

Table 2. Oxygen gas barrier equations and units

Equations	Units	
$OTR = J = \frac{Q}{At}$	$\text{cm}^3 \text{ m}^{-2} \text{ day}^{-1}$	(3.11)
$Permeance = \frac{OTR}{O_2\% \cdot (P_{atm} - P_{H_2O})}$	$\text{cm}^3 \text{ m}^{-2} \text{ day}^{-1} \text{ atm}^{-1}$	(3.12)
$OP = Permeance \cdot l$	$\text{cm}^3 \text{ m}^{-2} \text{ day}^{-1} \text{ atm}^{-1}$	(3.13)
$OP = \frac{OTR}{O_2\% \cdot (P_{atm} - P_{H_2O})} \cdot l$	$\text{cm}^3 \mu\text{m m}^{-2} \text{ day}^{-1} \text{ atm}^{-1}$	(3.14)

3.3.7 Inkjet printing

For printing, a cartridge is loaded with an ink and then mounted into an inkjet printer that can create patterns on-demand (**Figure 26**). In this thesis work, the aqueous SNP-graphene dispersion was modified with propylene glycol (0.0-1.5 wt%) to adjust the viscosity. The dispersion was further processed by ultrasonication using a Sonic Dismembrator (Fisher Scientific, US) with a probe (tip diameter 12.7 mm) for 70 min, and then filtrated with a cut-off size of 2 μm . The resulting SNP-graphene ink was loaded into a cartridge (Dimatix DMC 11610) that was mounted into a CeraPrinter F-Serie inkjet printer (CeraDrop, France). The printed films were annealed by photonic-sintering method using a Pulse Forge system (NovaCentrix, US). The photonic pulse energy from a xenon flash lamp (spectrum 200-1500 nm) was varied between 0.04-3.08 J cm^{-2} corresponding to bias 100-320 V. The pulse duration was 1 ms and the firing frequency was 1 Hz.

**Figure 26.** Inkjet printing of thin films on a flexible substrate.

4 Results and Discussion

4.1 Aqueous graphene dispersions

4.1.1 Graphene concentration

UV-vis absorption

As a starting point, the degree of dispersibility and concentration of graphene in aqueous dispersion systems can be evaluated by UV-vis spectroscopy (**Figure 27**). For the graphene dispersibility, an absorption peak around 270 nm in the UV region and an absorbance over the visible region are the spectroscopic features of stable and uniformly distributed graphene sheets in aqueous dispersion systems. For the aqueous FMN-stabilized graphene dispersions (FMN-graphene dispersions) (**Paper I**), the UV-vis absorption spectra before and after purification by ultracentrifugation were compared (**Figure 27a**). The FMN-graphene dispersion before the purification (dark orange) showed multiple absorption bands that originate from the FMN molecules (orange). The characteristic FMN absorptions are commonly located near 223 nm, 267 nm, 374 nm, and 445 nm[110], among which the maximum peak at 267 nm in the UV region is overlapping with that from graphene. After the FMN-graphene dispersion was purified (black), the intensity of these FMN bands dropped, thus indicating removal of excess FMN molecules in the dispersion. Moreover, a single absorption peak at 270 nm emerged. This peak is associated with the π - π^* transition of C=C that is expected for sp^2 -hybridized graphene sheets with conjugated π -systems[106]. These spectroscopic features indicate that the FMN-graphene sheets were dispersed in water with the aid of the FMN molecules, while the excess FMN in the dispersion was removed. For the aqueous SNP-stabilized graphene dispersions (SNP-graphene dispersions) (**Paper II and III**), the UV-vis absorption spectra were compared to that of an SNP reference and a graphene reference that were processed under the same conditions (**Figure 27b**). The SNP-graphene dispersion (blue solid line) that is more concentrated, showed a substantially higher absorbance of ~ 1 au in the visible region and a single absorption peak at 273 nm in the UV region, consistent with the FMN-graphene dispersion. This absorption peak is also associated with the π - π^* transition of the C=C, thus indicating that the sp^2 -hybridization of the carbon

atoms was not adversely affected by the SNPs. These are the main spectroscopic features expected of a stable aqueous graphene dispersion. For contrast, the absorption spectra of the SNPs (yellow solid line) and the graphene reference (grey dashed line) were both featureless in that wavelength range. The graphene reference spontaneously aggregated without the SNPs in the suspension, thus confirming the role of the SNPs as dispersing agents. For both the FMN-graphene dispersion and the SNP-graphene dispersion, the absorbance at wavelength 660 nm was used for the determination of the graphene concentration. At this wavelength, the spectroscopic features from the dispersing agents will not interfere with that from the dispersed graphene.

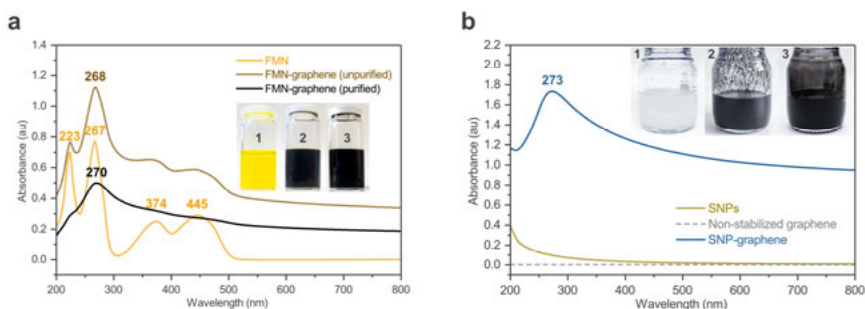


Figure 27. UV-vis absorption spectra of the aqueous graphene dispersions. **a** The aqueous FMN-graphene dispersion (**Paper I**). Inset: **1** FMN. **2** FMN-graphene (unpurified). **3** FMN-graphene (purified). **b** The aqueous SNP-graphene dispersion (**Paper III**). Inset: **1** SNPs. **2** Non-stabilized graphene. **3** SNP-graphene.

Attenuation coefficient

To determine the graphene concentration via the optical absorbance, the attenuation coefficient, α (Beer-Lambert's law, **3.3.1**), is needed for each aqueous dispersion system at a specific wavelength (**Paper I and II**). For this purpose, a set of six dilutions from an aqueous graphene dispersion with a known graphene concentration was prepared and the absorbance of these dilutions at wavelength 660 nm was measured to construct a calibration curve comprising the absorbance plotted against the graphene concentration. (**Figure 28**). The graphene concentration, in general, was determined by thermogravimetric analysis (TGA). For instance, an aliquot (3 mL) from the known graphene dispersion was dried at 105 °C 24 h and then weighed to find the total solid content (~ 28 mg). In this solid content, the graphene fraction (5%) was determined from the TGA curves at 700 °C based on the residual weights. Based on the graphene fraction, the graphene concentration could then be calculated (~ 0.5 mg mL⁻¹). Consequently, the attenuation coefficient was determined from the slope of the calibration curve to 6,733 m⁻¹ mg⁻¹ mL for the aqueous FMN-graphene dispersion system (**Paper I**) and to 3,384 m⁻¹ mg⁻¹ mL for the aqueous SNP-graphene dispersion system (**Paper II**), respectively. The theoretical value for graphene has been predicted to be 4,237

$\text{m}^{-1} \text{mg}^{-1} \text{mL}[111]$, which is close to the midpoint of these experimental values obtained here. The variation in the value for the coefficient is not fully understood and could be attributed to the different dielectric constants in the surrounding media.

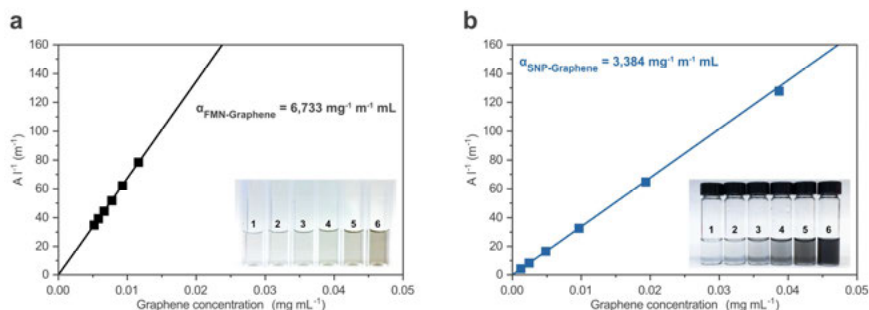


Figure 28. Determination of the attenuation coefficient, α , from the slope of the calibration curves. **a** The calibration curve for the aqueous FMN-graphene dispersion (**Paper I**). Inset: **1-6** Six dilutions by factor 225, 200, 175, 150, 125, and 100. **b** The calibration curve for the aqueous SNP-graphene dispersion (**Paper II**). Inset: **1-6** dilutions by factor 400, 200, 100, 50, 25, and 12.5.

4.1.2 Starting concentration parameters

With the attenuation coefficient for the aqueous dispersion systems known, the intensity of the absorbance at wavelength 660 nm can be utilized to evaluate the dispersion conditions, such as starting concentrations, sonication time, and colloidal stability. For the starting concentration study, a set of ten aqueous FMN-graphene dispersions were prepared with a fixed amount of starting graphene powder (0.10 mg mL^{-1}) and varied FMN concentrations ($0.02, 0.04, 0.06, 0.08, 0.10, 0.20, 0.40, 0.60, 0.80$, and 1.00 mg mL^{-1}). Each dispersion was processed by ultrasonication via probe (tip diameter 6 mm, 40% amplitude) for 5 min (**Figure 29a**). When the FMN concentration in the dispersions was increased from 0.02 up to 0.20 mg mL^{-1} , the dispersed graphene concentration was efficiently increased from ~ 0.04 up to $\sim 0.12 \text{ mg mL}^{-1}$ and then remained constant with additional FMN. This trend demonstrates that a starting FMN:graphene mass ratio condition of 2:1 is needed. For the SNP-graphene dispersions, a similar approach was applied with a higher starting graphene concentration. A set of five aqueous SNP-graphene dispersions were prepared with fixed amount of starting graphene powder (0.5 mg mL^{-1}) and varied starch concentrations ($0.5, 5.0, 10.0, 15.0, 20.0 \text{ mg mL}^{-1}$). These dispersions were processed by ultrasonication via the same probe design (tip diameter 6 mm, 40% amplitude) for 10 min. In addition, the colloidal stability of these dispersions was initially evaluated over 12 hours of storage time (**Figure 29b**). When the starch concentration in the dispersion was 10 mg mL^{-1} and higher, a more stable graphene dispersion

was achieved. This starch concentration corresponds to a starting starch:graphene mass ratio condition of 20:1 (**Paper II**). Overall, the optimal mass ratio condition for the aqueous dispersion systems was identified at 2:1 for the FMN:graphene and at 20:1 for the starch:graphene, respectively. Although the starting graphene concentration in the aqueous FMN-graphene suspension was lower than in the SNP-graphene, the relatively smaller amphiphilic FMN molecule could disperse graphene efficiently using a lower amount. This amount is also lower compared with what is typically needed using other traditional dispersing agents[112].

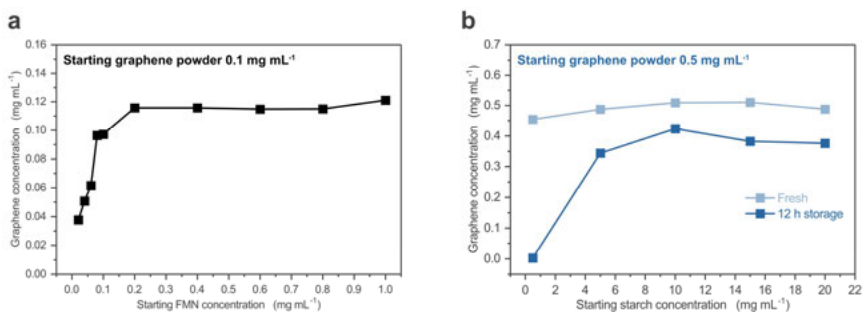


Figure 29. Starting concentration conditions. **a** The dispersed graphene concentration with varied starting FMN concentration (**Paper I**). **b** The dispersed graphene concentration with varied starting starch concentration (**Paper II**).

4.1.3 Processing parameters

Once the optimal mass ratio conditions were determined, the ultrasonication processing time can be investigated. For the aqueous FMN-graphene dispersions (**Paper I**), the processing time with a probe (tip diameter 6 mm, 40% amplitude) was varied under cooling from 0 to 18 min. For this purpose, a suspension with a starting graphene concentration of 0.5 mg mL⁻¹ was prepared according to the condition FMN:graphene mass ratio 2:1. When the mass ratio condition was met, the maximum dispersed graphene concentration was efficiently achieved after only 6 min of sonication time (**Figure 30a**). For the SNP-graphene dispersions (**Paper III**), the processing time was investigated with a larger probe design (tip diameter 13 mm, 50% amplitude) and varied under cooling from 2.5-60 min. Here, the starting graphene concentration in the suspension was increased (3 mg mL⁻¹) according to the condition starch:graphene mass ratio 20:1. When this condition was assured, the dispersed graphene concentration could be increased with extended sonication time and then reach a maximum between 30-60 min (**Figure 30b**). In addition, the corresponding median particle size of the SNP-graphene sheets in the dispersion was measured. The particle size, on the other hand, decreased with sonication time and then remained relatively constant around 3-5 μ m. This trend is related to the ultrasonication-induced separation and

scissoring effects on the graphene sheets, thus leading to thinner sheets and smaller lateral sizes[113]. In addition, extended sonication time can also lead to ultrasonication-induced defects. Although these defects are predominantly introduced at the graphene edges rather than the basal plane[114], the balance between the colloidal stability and the particle size needs to be considered based on the intended applications and end-uses of the dispersed graphene.

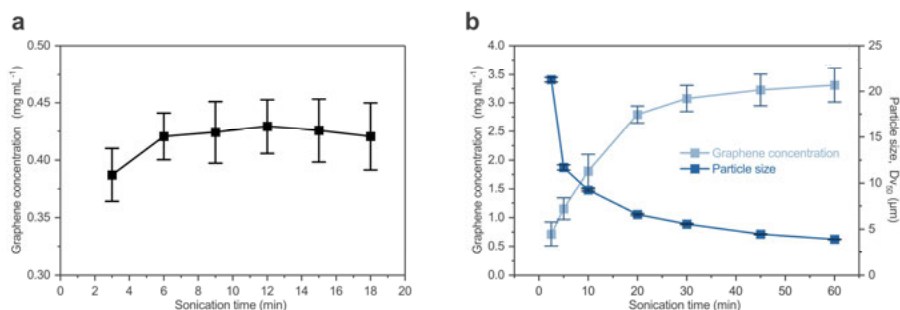


Figure 30. Ultrasonication processing conditions. **a** The aqueous FMN-graphene dispersion concentration with sonication time (**Paper I**). **b** The aqueous SNP-graphene dispersion concentration and median particle size (Dv₅₀) with sonication time (**Paper II**).

4.1.4 Colloidal stability

After the dispersion conditions were optimized, the colloidal stability of the aqueous graphene dispersions was further evaluated. The fundamental principle of the colloidal stability of an aqueous graphene dispersion is defined by how well the graphene sheets can remain dispersed over time. The main concern over time is the attractive forces that induce the graphene sheets to restack and form larger aggregates, and consequently sediment faster. Therefore, the colloidal stability can be evaluated by either observation or measurement of the change in graphene concentration over time. For the aqueous FMN-graphene dispersions (**Paper I**), the dispersions from the concentration study described in chapter (4.1.2) were stored at room temperature and observed for six months (**Figure 31a**). With the storage time, only a few aqueous graphene dispersions remained dispersed with the varied FMN concentration. At a lower FMN concentration (samples 1-3), fewer FMN molecules were expected to be available for adsorption on the graphene surface. When the FMN concentration (sample 4-6) was closer to the FMN:graphene mass ratio condition 2:1 (sample 6), more graphene was stable. Interestingly, at a higher FMN concentration (sample 7-10), less graphene was stable despite excess FMN molecules available in the dispersion. A similar trend is typically observed for ionic surfactants used for aqueous graphene dispersions[23,82]. As the ionic surfactant concentration in the dispersion increases, so does the ion concentration. According to the

DLVO theory explained in chapter (2.2.1), the Debye screening length decreases with the ion concentration, thus progressively lowering the overall potential energy barrier between the graphene sheets[115]. Consequently, the graphene sheets without a potential energy barrier to overcome the attractive forces will spontaneously aggregate and sediment, as observed for the aqueous FMN-graphene dispersions with higher FMN concentration. For the concentrated aqueous SNP-graphene dispersion (**Paper III**), the colloidal stability was evaluated by the optical absorbance with time (**Figure 31b**). In addition, two storage temperature conditions 4 °C and 23 °C were compared. The SNP-graphene dispersion stored at the colder temperature (4°C) dropped 89.2% of its original graphene concentration after 1 month, while that in the room temperature remained stable. As a result, the colloidal stability of the dispersed SNP-graphene sheets was found temperature-dependent. This temperature factor could be attributed to the retrogradation process of starch gels, whereby the starch polysaccharides form intra- and intermolecular interactions via hydrogen bonding over time. Immediately after gelatinization during the first 5-7 days of storage, the retrogradation rate is initially rapid and then slowing down[116,117]. Furthermore, the storage of starch gels under a colder temperature condition can induce an accelerated retrogradation process[118]. Nevertheless, upon ultrasonication, the SNP-graphene dispersion stored at the colder temperature was readily re-dispersed.

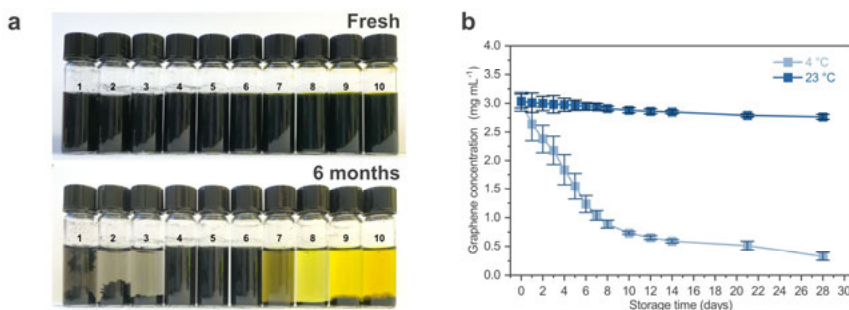


Figure 31. Colloidal stability of the aqueous graphene dispersions. **a** The aqueous FMN-graphene dispersions with fixed graphene (0.1 mg mL⁻¹) and varied FMN concentration (0.02-1 mg mL⁻¹). **b** The colloidal stability of the concentrated aqueous SNP-graphene dispersion (60 min ultrasonication) stored at 4°C and at room temperature 23 °C (**Paper III**).

4.1.5 Particle size distribution

The particle size distribution of the aqueous graphene dispersions can be estimated by laser diffraction (**Figure 32**). This technique can provide statistical information on the whole dispersion for a wide range of particle sizes (10 nm-3.5 mm). In this approach, an optical model based on the Mie theory was applied to derive the graphene particle size by assuming the

diameter of a sphere with equivalent volume. For the aqueous FMN-graphene dispersions, the FMN-graphene sheets (**Figure 32a**) showed a median particle size (Dv50) of $13.8 \pm 3.1 \mu\text{m}$. This means that 50% of the graphene sheets population is below this particle size. The median particle size of the SNP-graphene sheets (blue) measured $3.4 \pm 0.0 \mu\text{m}$ (**Figure 32b**). The graphene reference without SNPs (grey), in contrast, measured the largest median particle size of $53.6 \pm 0.4 \mu\text{m}$ as well as the broadest particle size distribution. This contrast in particle size suggests that the SNPs (yellow), with the median particle size $0.3 \pm 0.0 \mu\text{m}$ in the dispersion, play an important role in aiding the dispersion of graphene in water and preventing the restacking into larger aggregates. Moreover, the smaller particle size of the SNP-graphene sheets compared with the FMN-graphene sheets could be attributed to the extended sonication time during the preparation of the SNP-graphene dispersion.

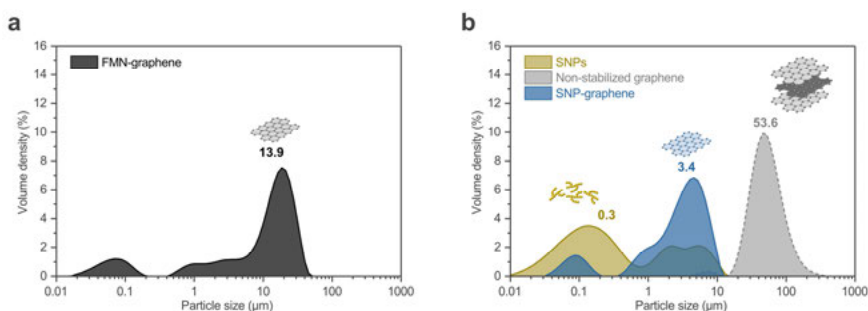


Figure 32. Volume-weighted particle size distribution of the aqueous graphene dispersions. **a** The aqueous FMN-graphene dispersion with the median particle size highlighted. **b** The aqueous SNP-graphene dispersion (blue), SNP reference (yellow), and a non-stabilized graphene reference (grey) (**Paper III**).

4.1.6 Morphology

The morphology and thickness of the dispersed graphene sheets can be analysed by SEM and STEM (**Figure 33**). In the SEM images (**Figure 33a,b**), SNP-graphene sheets were observed in the size range of $\sim 3 \mu\text{m}$, consistent with the particle size distribution measured by the laser diffraction, as shown in chapter (4.1.5). Furthermore, a magnified view on the SNP-graphene sheets also revealed extensive surface features, such as ripples and wrinkles[119]. In the STEM images (**Figure 33c,d**), relatively large surface areas of the SNP-graphene sheets showed the same intensity, thus indicating a uniform thickness. By counting the graphene sheet edges, it is possible to quantify the number of graphene layers[114]. However, this approach can become challenging when the graphene sheets have surface features, such as self-folding events. Nevertheless, the SNP-graphene sheets have an estimated number of layers in the range of 1-5. In addition, few round-shaped nanoparticles in the size range of a few tens of nanometres were observed on

the graphene surface, as shown in both the BF and the HAADF images, thus indicating structures with a different crystal structure and mass than the SNP-graphene sheets.

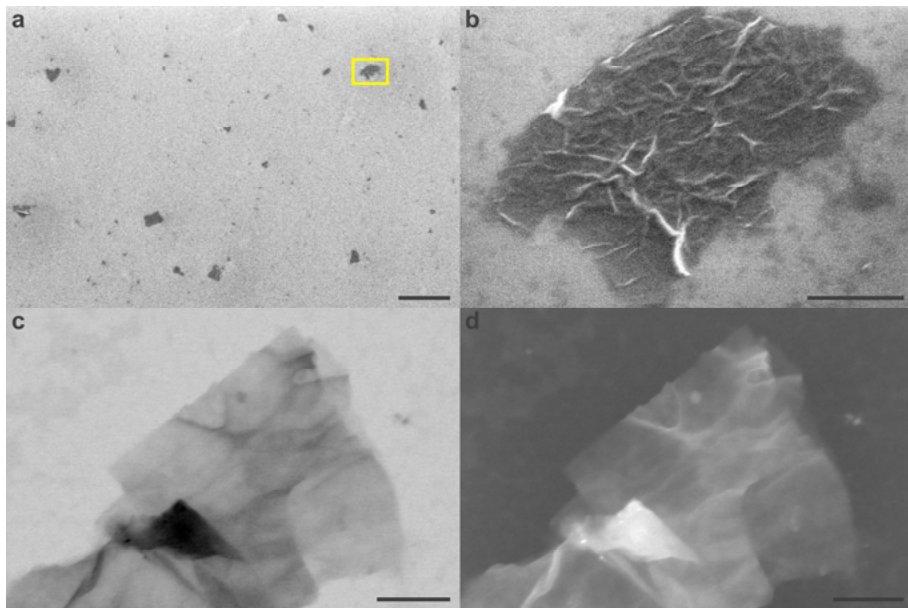


Figure 33. Morphology of the SNP-graphene sheets. **a** An SEM image of SNP-graphene sheets. Scale bar: 5 μm . **b** Magnified view of an individual SNP-graphene sheet from the yellow box. Scale bar: 500 nm. STEM images of the SNP-graphene sheets. **c** BF mode. Scale bar 200 nm. **d** HAADF mode. Scale bar 200 nm (**Paper II**).

4.1.7 Topography

SNP-graphene sheets were further investigated on freshly cleaved mica substrates at the nanoscale using AFM (**Figure 34**). In the topographical image of a representative SNP-graphene sheet (**Figure 34a**), the lateral size is $\sim 1\ \mu\text{m}$ and the height is $\sim 5\ \text{nm}$. An isolated graphene reference that was processed under the same conditions without the SNPs, in contrast, showed a clean surface (**Figure 34b**). Therefore, the round-shaped structures spread over the surface on the SNP-graphene sheets were identified as the SNPs. In addition, a few of these SNPs were also observed on the mica substrate. The height of the SNPs on the graphene surfaces measured $\sim 5\ \text{nm}$ in the dry state. This height of the SNPs extends beyond the interlayer distance (0.335 nm) between stacked graphene layers that are held by van der Waals forces. Therefore, the SNPs are expected to prevent the restacking of graphene layers by steric hindrance. This could, in parts, explain the dispersion mechanism of the SNPs.

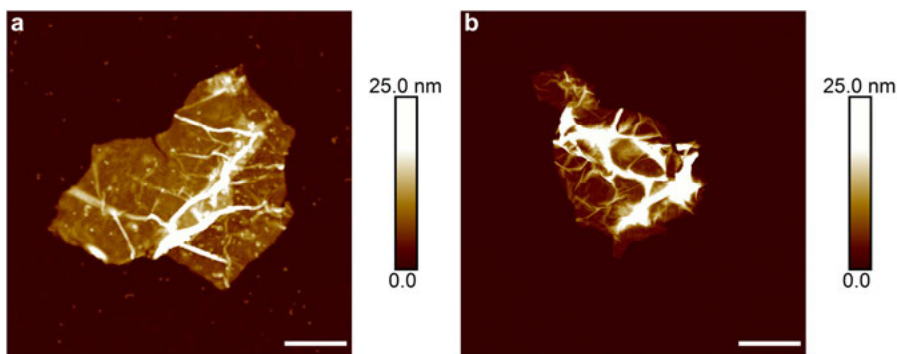


Figure 34. Topography of the SNP-graphene sheets by AFM. **a** The AFM image of an SNP-graphene sheet decorated with SNPs on the graphene surface. **b** The AFM image of a graphene reference processed under the same conditions without SNPs. Scale bar: 400 nm (**Paper II**).

4.1.8 Physicochemical properties

Confocal Raman spectroscopy

The quality of the dispersed graphene sheets can be evaluated by confocal Raman spectroscopy (**Figure 35**). For the SNP-graphene sheets (**Paper II**), the adsorption of the SNPs onto the graphene surface is expected to influence the breathing mode of the aromatic carbon rings, and thus activating the D peak at 1350 cm^{-1} . Therefore, the intensity ratio of $I(\text{D})/I(\text{G})$ can be used to estimate the degree of disorder caused by the SNP adsorption. Indeed, when the SNPs were adsorbed, the intensity ratio $I(\text{D})/I(\text{G})$ typically increased from 0.4 up to 0.6, thus indicating a higher degree of disorder. In addition, adjacent to the G peak at 1580 cm^{-1} , a weak shoulder peak emerged more prominent at 1620 cm^{-1} (D' peak). The D peak (intervalley process) and the D' peak (intravalley process) are both activated by disorders[109]. After deconvolution using the Voigt function, this intensity ratio $I(\text{D})/I(\text{D}')$ can provide a deeper insight into the nature of the disorders based on the scale: 3.5 (boundaries), 7 (vacancies), and 13 (sp^3 defects)[120]. The intensity ratio of both the SNP-graphene sheets and the graphene reference were both in close range, 2.4 and 2.6, respectively. This range indicates boundary effects, such as various surface features and edges. Furthermore, with the versatility of the Raman spectroscopy, the thickness of the graphene can also be estimated based on the peak position of the G peak[121,122] or the peak shape of the 2D peak[108,123]. Accordingly, based on the G peak position of supported graphene, an average peak position of 1584 cm^{-1} for the SNP-graphene sheets indicates a bilayer. Based on the 2D peak, an average of FWHM of 66 cm^{-1} indicates 4-5 layers. However, the estimation of the thickness based on these two metrics is qualitative and require caution, since disorders can influence

the characteristics of the G peak and the 2D peak[124,125]. Overall, the Raman analysis suggests that the SNPs could disperse thin graphene sheets with a relatively low degree of disorders.

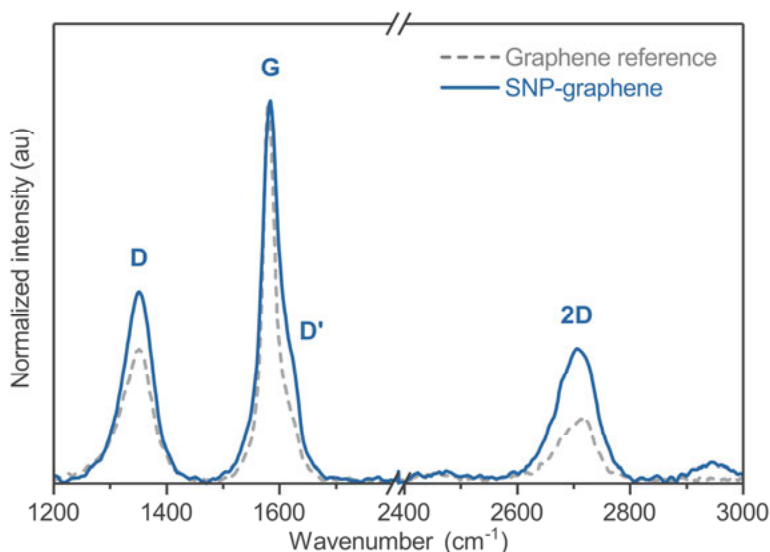


Figure 35. Raman spectra of SNP-graphene sheets (blue) compared with a graphene reference without SNPs (grey) (**Paper II**).

FT-IR analysis

The molecular interactions in the aqueous graphene dispersion can be investigated by FT-IR spectroscopy (**Figure 36**). The obtained FT-IR spectra can provide information on the vibrational motions of molecules related to intra- and intermolecular interactions, such as hydrogen bonding. FT-IR was performed to gain deeper insight into the FMN-graphene interaction and the FMN molecular conformation on the graphene surface (**Paper I**). In the FT-IR spectra for the aqueous FMN-graphene dispersions (**Figure 36a**), the FT-IR peaks of the FMN molecule (orange solid line) are associated with vibrations from the carbonyl groups at 1716 cm^{-1} ($\text{C}_4=\text{O}$) and 1645 cm^{-1} ($\text{C}_2=\text{O}$). In the vicinity are the peaks associated with the conjugated π -system in the isoalloxazine at 1573 cm^{-1} , 1533 cm^{-1} , and 1499 cm^{-1} ($\text{C}=\text{C}$, $\text{C}_{4a}=\text{N}_5$, and $\text{C}_{10a}=\text{N}_1$)[126]. Among these peaks, the carbonyl groups $\text{C}_4=\text{O}$ and $\text{C}_2=\text{O}$ are the most sensitive to intermolecular interactions[127], especially with water molecules via hydrogen bonding. When hydrogen bonds between FMN molecules and water molecules are allowed, this type of interaction could induce a strong downshift of the carbonyl peaks by $57\text{--}69\text{ cm}^{-1}$ [128]. For the FMN-graphene sheets (**Paper I**), when the FMN molecules were absorbed onto the graphene surface via π - π interactions, these carbonyl peaks $\text{C}_4=\text{O}$ and

C₂=O showed, on the contrary, strong upshifts to the higher wavenumbers. These upshifts indicate weaker intermolecular interactions between the FMN molecules and the water molecules. This trend suggests a parallel conformation of the FMN molecules on the graphene surface[129,33]. As for the aqueous SNP-graphene dispersions, hydrogen bonding also plays an important role between the starch and the water molecules (**Paper II**). Since starch is hygroscopic and absorbs moisture from the ambient environment, all the dispersions and reference samples were dried and then pre-conditioned in an oven at 105 °C for 24 h prior to measurement. In the FT-IR spectra (**Figure 36b**), the distinct peak at 1572 cm⁻¹ was assigned to the C=C stretching vibrations of graphene, commonly found in this region for conjugated π -systems[130]. The presence of graphene changed the vibrational motions of the SNPs. The FT-IR peaks of the SNPs were identified at 1149 cm⁻¹ (C—O, C—C stretching, and partially C—O—H contributions), 1078 cm⁻¹, and 995 cm⁻¹ (C—O—H bending)[131]. Among these peaks, the largest peak at 995 cm⁻¹ consists of three overlapping peaks, which after deconvolution can provide a deeper insight into the starch structure. After deconvolution (**Figure 36c**), these peaks were identified at 1047 cm⁻¹ (crystalline), 1022 cm⁻¹ (amorphous), and 995 cm⁻¹ (hydrated)[132]. The intensity ratio of 1047/1022 (crystalline-to-amorphous) for the SNPs (0.25) and the SNP-graphene sheets (0.33) was lower than for the starch granules (0.37). This indicates that the polysaccharide chains in the SNPs were less ordered after the two-step process involving gelatinization and ultrasonication. Furthermore, the intensity ratio of the 995/1022 (hydration-to-amorphous) for the SNP-graphene sheets (0.74) was the lowest compared to that for the SNPs (1.10) and the starch granules (1.31) (**Figure 36d**). Since the starch peak at 995 cm⁻¹ is mainly associated with the intra- and intermolecular hydrogen bonding at the hydroxyl group at C(6)—O—H, this peak is therefore sensitive to the water content. This indicates that the presence of graphene changed the molecular environment for the hydroxyl groups of the adsorbed SNPs to interact with water. This was consistent with the reduced peak intensity at 1640 cm⁻¹ associated with the weaker vibrational motions of bound water in the SNP-graphene.

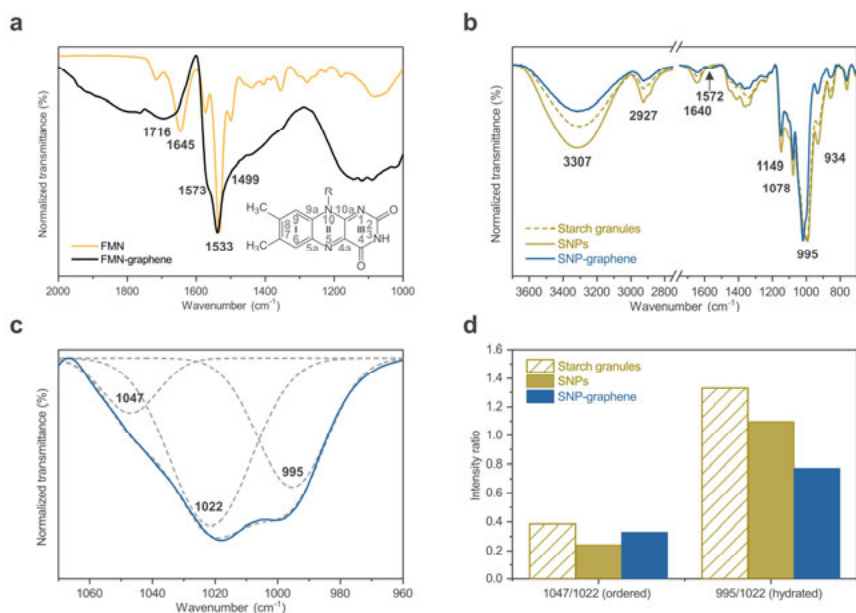


Figure 36. FT-IR analysis of the aqueous graphene dispersions in a dry state. **a** The FT-IR spectra of the aqueous FMN-graphene dispersion (black) compared with an aqueous FMN solution (orange). **Inset:** Chemical structure of the isoalloxazine (**Paper I**). **b** The FT-IR spectra of the aqueous SNP-graphene dispersion. The SNP-graphene dispersion (blue) is compared to starch granules (yellow dashed) and SNPs (yellow). **c** An example of deconvoluted peaks of the starch peak at 995 cm^{-1} . The peaks were deconvoluted by a Gaussian fit. **d** A summary of the deconvoluted peak intensity ratio $1047/1022$ (ordered starch) and $995/1022$ (hydrated starch), respectively (**Paper II**).

Thermal properties

The thermal stability and solid content of the aqueous graphene dispersions were investigated by TGA (**Figure 37**). For the aqueous FMN-graphene dispersions (**Paper I**), the measurements were performed from $25\text{--}900\text{ }^{\circ}\text{C}$ under an oxygen atmosphere (**Figure 37a**). The TGA curve of the FMN (orange solid line) showed four decomposition steps associated with the desorption of water ($25\text{--}180\text{ }^{\circ}\text{C}$), the dehydroxylation of the ribityl side chain of the FMN molecule ($180\text{--}320\text{ }^{\circ}\text{C}$), the decomposition of the isoalloxazine to carbon black ($320\text{--}500\text{ }^{\circ}\text{C}$), and finally residual carbon black to gaseous state ($> 500\text{ }^{\circ}\text{C}$) [133]. The TGA curve of the starting graphene powder (grey dashed line) was relatively flat from $25\text{ }^{\circ}\text{C}$ and up to an inflection point at $685\text{ }^{\circ}\text{C}$, thus indicating a high degree of carbon purity [134]. The inflection point is the temperature at which the rate of weight loss is maximum and can be used to compare the thermal stability between two systems. In the DTG curves (**Figure 37b**), when the FMN molecules were adsorbed onto the graphene surface (black solid line), the infection point (DTG peak) was elevated from

685 °C and up to 829 °C (144 °C), thus enhancing the thermal stability of the graphene sheets. As a result of the strong π - π interaction between the FMN molecules and the graphene, the FMN could act as a protective layer on the graphene surface[135]. For the concentrated aqueous SNP-graphene dispersions (**Paper III**), the measurements were performed from 25-900 °C under a nitrogen atmosphere (**Figure 37c**). As with the FT-IR analysis, all the graphene dispersions were dried and then pre-conditioned in an oven at 105 °C for 24 h prior to measurement. The TGA curve of the starting graphene powder (grey dashed line) under a nitrogen atmosphere, compared with that under the oxygen atmosphere, was relatively flat throughout the whole heating process, thus confirming the high degree of carbon purity. The TGA curve for the starch granules (grey dashed line) and the SNPs (yellow solid line), in contrast, showed three decomposition regions. In general, the regions 25-170 °C is the weight loss associated with desorption of weakly adsorbed water, 200-400 °C is the depolymerization of the starch polymer backbone, and finally, 400 °C and higher is the formation of carbonaceous residues[136–138]. The boundaries for calculating the weight loss in each region were selected based on the DTG peaks widths (**Figure 37d**). Accordingly, in the first region, the weight loss associated with the water content in the starch references (grey dashed and solid) were in the range of 3-6%, while the SNP-graphene (black solid) was substantially lower 0.92%. Indeed, the presence of graphene reduced the moisture uptake of the starch, which is beneficial for gas barrier applications to prevent swelling. In the second region, the SNPs (grey and black solid) started to decompose at a lower temperature than the starch granules (grey dashed). Furthermore, the decomposition of the SNPs reached a maximum rate at 312 °C compared with the starch granules at 318 °C. This is beneficial for inkjet printing applications, as the resulting printed composites often require post-annealing to obtain competitive conductivity values. The decomposition behaviour of starch at lower temperatures has been attributed to the higher surface area as well as structural differences between amylose and amylopectin[139–141]. Finally, since graphene was relatively inert throughout the heating process, the residual weight can be associated with the graphene content. Therefore, graphene concentration could be determined to 0.48 mg mL⁻¹ for the initial SNP-graphene dispersion (**Paper II**) and 2.97 mg mL⁻¹ for the concentrated SNP-graphene dispersion (**Paper III**), respectively. In general, the thermal behaviour of concentrated SNP-graphene dispersion followed the same trend and motivates the preparation of composites for gas barrier and inkjet printing applications.

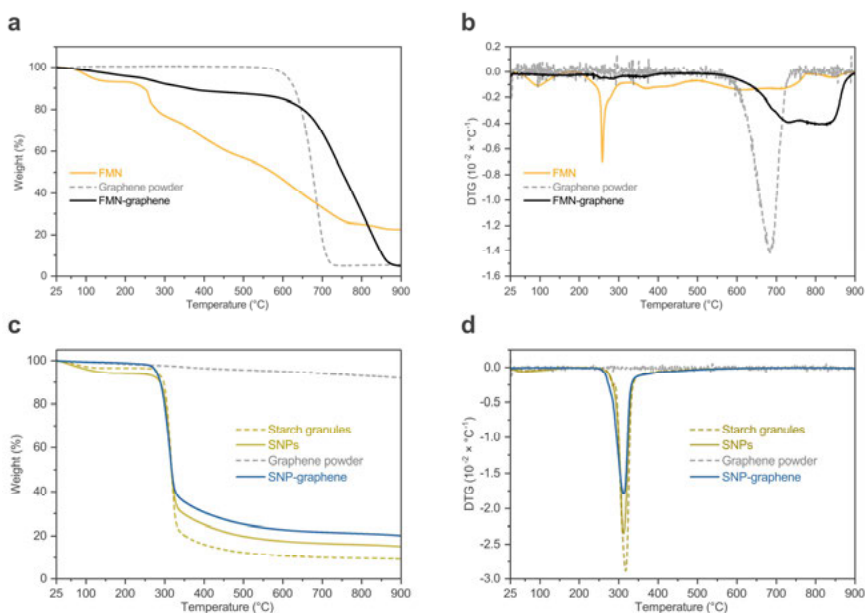


Figure 37. Thermal decomposition of the aqueous graphene dispersions in a dry state. **a-b** The TGA and The DTG curves of the aqueous FMN-graphene dispersion under an oxygen atmosphere (**Paper I**). **c-d** Similarly, the TGA and the DTG curves of the aqueous SNP-graphene dispersion under a nitrogen atmosphere (**Paper II**).

4.1.9 FMN-graphene interactions

To elucidate the FMN-graphene interaction, the effect of the aqueous graphene dispersion on the spectroscopic properties of the isoalloxazine was investigated (**Figure 38**). The isoalloxazine ring system in the FMN molecule can function as a chromophore and is naturally sensitive to the changes in the electronic states, conformation, and substituents from the environment. Therefore, the FMN spectroscopic properties owing to the isoalloxazine can provide deeper insight into the stabilization mechanism of FMN for aqueous dispersions of graphene. To this end, a set of ten dispersions was prepared with a fixed amount of starting graphene powder (0.10 mg mL^{-1}) and varied FMN concentrations ($0.02, 0.04, 0.06, 0.08, 0.10, 0.20, 0.40, 0.60, 0.80$, and 1.00 mg mL^{-1}), according to the previous protocol in chapter (4.1.2). The UV-vis absorption of these dispersions was measured from 250–600 nm (**Figure 38a**). When the starting FMN concentration (0.04 – 0.10 mg mL^{-1}) in the dispersion was equal or lower than the graphene (0.10 mg mL^{-1}), the corresponding absorption spectra 1–5 (from bottom to top) were dominated by the absorption from the dispersed graphene. Nevertheless, when the FMN concentration (0.20 – 1.00 mg mL^{-1}) was higher, the absorption spectra 6–10 revealed two adjacent FMN bands at 368 nm (band II) and 442 nm (band I) that progressively shifted towards the longer wavelengths 374 nm and 445 nm

with additional FMN, respectively. For the absorption spectra of the pure aqueous FMN solutions (**Figure 38b**), the band positions 374 nm and 445 nm correspond to the FMN bands of free FMN molecules and remained constant at all FMN concentrations. As a result, these FMN bands II and I in the aqueous FMN-graphene dispersions appeared blue-shifted in response to the FMN-graphene interactions. In general, blue shifts of these FMN bands occur when the two FMN molecules aggregate into dimers with their isoalloxazines stacked in a parallel conformation[142]. The aggregation of FMN is induced by concentration and accompanied by the degree of blue shift. The degree of blue shift increases with the FMN dimer fraction in the solution[143]. However, the FMN concentration needed to promote FMN dimers ($\sim 130 \text{ mg mL}^{-1}$) with a similar degree of blue shifts is well above the range used here (1 mg mL^{-1})[143]. Therefore, the strong FMN-graphene interactions suggest a parallel conformation that mimics that of the FMN dimers, thus promoting the observed blue shifts.

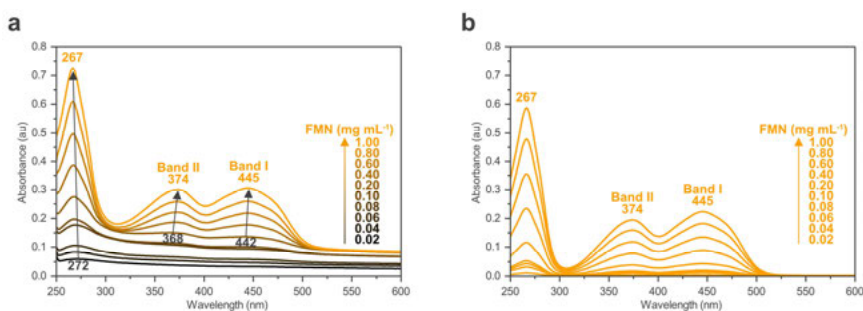


Figure 38. FMN-graphene interaction study by UV-vis spectroscopy. **a** UV-vis absorption spectra of the aqueous FMN-graphene dispersion with increased FMN concentration (indicated by arrow). **b** UV-Vis absorption spectra of the aqueous solutions of FMN in the same concentration range (indicated by arrow). The FMN solutions did not display spectroscopic shifts (**Paper I**).

From the gained understanding of the aqueous FMN-graphene dispersions, a stabilization mechanism of FMN is proposed (**Figure 39**). In the aqueous suspension containing graphene powder and FMN molecules during ultrasonication, relatively large graphene surfaces become available for adsorption. The hydrophobic isoalloxazine part of the FMN molecules is expected to stack on the hydrophobic plane of graphene in a parallel conformation via hydrophobic interactions, van der Waals forces, and π - π interactions. Such parallel conformation induces a change in the orientation of the transition dipole moments responsible for the absorption band II at 374 nm ($S_0 \rightarrow S_2$) and band I at 445 nm ($S_0 \rightarrow S_1$). These bands are predominantly associated with the $\pi \rightarrow \pi^*$ transition from the ground state to the lowest-lying excited states of the isoalloxazine[144]. In the FMN dimer case, the vector sum of parallel transition dipole moments permits raising the transition $S_0 \rightarrow$

S_2 , thus reflecting blue shifts of the absorption band II. The vector sum for the oblique transition dipole moments permits both lowering and raising of the transition $S_0 \rightarrow S_1$, thus reflecting an absorption peak splitting[142]. As these spectroscopic features were observed in the absence of FMN dimers, the FMN-graphene interactions are therefore responsible for these features.

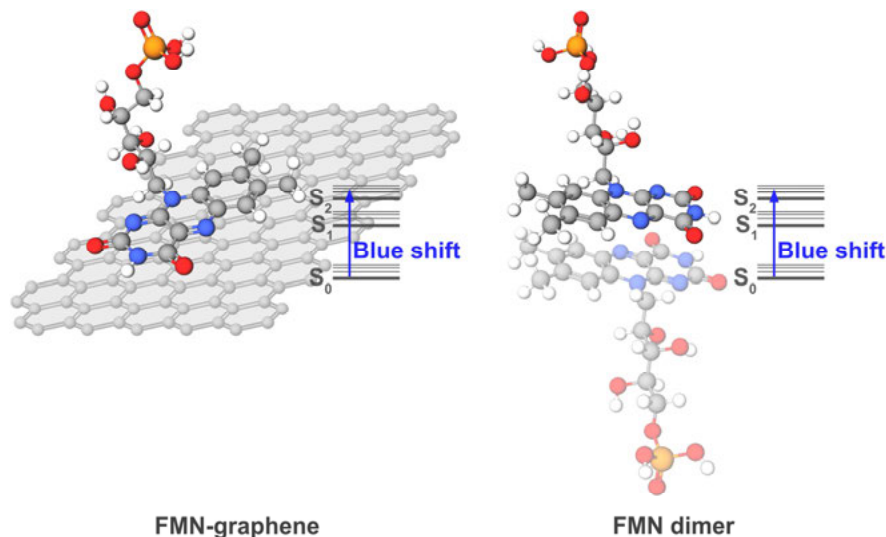


Figure 39. Schematic illustrations of the adsorption of the FMN molecule on the graphene surface in a parallel conformation, thus mimicking the conformation of an FMN dimer that results in spectroscopic shifts of the FMN absorption bands (**Paper I**).

4.1.10 SNP-graphene interactions

Preparation of the SNPs

The formation of SNPs by gelatinization and ultrasonication were investigated in a wet state on glass substrates using optical microscopy (**Figure 40**). First, an aqueous suspension of the corn starch powder was prepared. Under the microscope, the starch granules showed polygonal shapes with a particle diameter in the size range of 15-20 μm (**Figure 40a**), whereafter gelatinization appeared flat and swollen with a larger diameter up to 30-40 μm (**Figure 40b**). After ultrasonication was applied via probe for 3 min, the swollen granules were ruptured and fragmented (**Figure 40c**). In addition, the ultrasonication process also promotes leaching and chain scission of the starch polysaccharides. Therefore, the formation of SNPs was expected after extended ultrasonication for 30 min (**Figure 40d**).

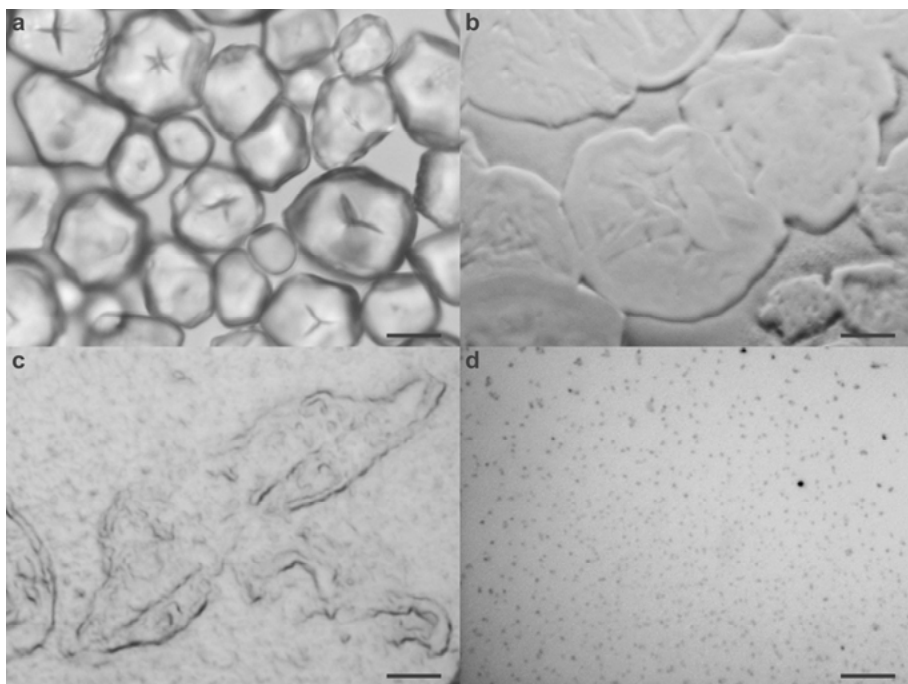


Figure 40. Optical microscopy of the preparation steps of the SNPs in a wet state. **a** Starch granules of native corn. **b** Gelatinized starch granules (95 °C for 20 min). **c** Ruptured starch granules after ultrasonication (3 min). **d** Resulting SNPs after extended ultrasonication (30 min). Scale bars: 10 μm (**Paper II**).

The morphology of the SNPs after the two-step process was further investigated in a dried state at the nanoscale using AFM (**Figure 41**). For this purpose, a dilute solution was spin-coated on a freshly cleaved mica substrate. The topographical image indeed showed round-like structures spread uniformly across the substrate (**Figure 41a**). In a magnified view (**Figure 41b**), the SNPs measured an average height of ~ 5 nm. As noted previously, there is a variation in particle size of the SNPs when measured in the dried state (AFM) compared with those in the wet state (Mastersizer). In the wet state, starch absorbs water via intermolecular interactions (hydrogen bonding), especially during gelatinization at high temperatures, thus leading to extensive swelling. On the contrary, during cooling or drying, the polysaccharide chains retrograde into denser structures and exude water, thus reducing particle size[118]. These phenomena explain the disparity in size between the SNPs in the wet (larger) and those in the dry state (smaller).

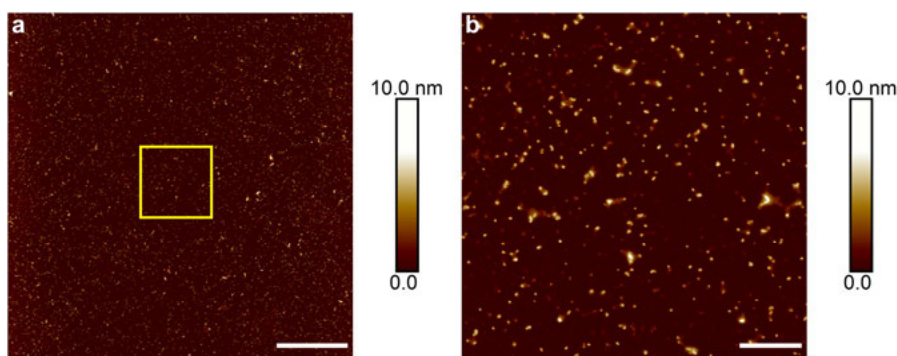


Figure 41. Topography of the SNPs by AFM. **a** The AFM image of SNPs with a relatively uniform particle size distribution. Scale bar: 2 μ . **b** A magnified view of the SNPs from the yellow box. The SNPs displayed round-like structures with an average height of ~ 5 nm. Scale bar: 400 nm (**Paper II**)

To gain deeper insight into the dispersing mechanism of the SNPs, the zeta potential distribution and the surface tension were investigated (**Figure 42a**). The mean zeta potential of the SNPs (yellow) was -17.6 ± 3.9 mV, while the SNP-graphene sheets (blue) -22.9 ± 4.8 mV. Although the SNPs were made from unmodified starch and considered non-ionic, they could indeed contribute to a negative zeta potential[145]. According to the DLVO theory explained in chapter (2.2.1), the magnitude of the zeta potential between two charged surfaces is proportional to the electrostatic repulsion and could aid the colloidal stability. For comparison, the zeta potential of graphene sheets that are stabilized by traditional ionic surfactants can vary from -64 mV (anionic) and up to 57 mV (cationic)[74]. Furthermore, graphene sheets that are stabilized by the non-ionic counterparts (uncharged) can also have a non-zero zeta potential as low as -24 mV[146]. In this thesis work, the SNP-graphene sheets demonstrated long-term colloidal stability despite the relatively low magnitude of zeta potential (-22.9 mV), thus suggesting that additional stabilization mechanisms may exist, such as steric hindrance. Moreover, the presence of SNPs reduced the surface tension of water from 72.3 mN m^{-1} down to a minimum of 56.9 mN m^{-1} (**Figure 42b**), thus making the dispersion of graphene in water more energetically favourable. A similar effect has also been reported using other relevant polysaccharides, such as chitosan and pullulan[41]. Overall, the SNPs play an important role in the colloidal stability of graphene in water. These results suggest that the SNPs can lower the amount of work required to disperse graphene in water as well as stabilize the graphene sheets mainly by steric hindrance and partly by electrostatic repulsion.

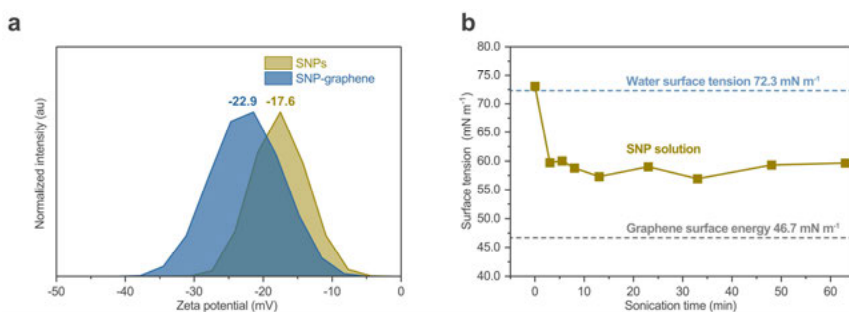


Figure 42. The zeta potential and the surface tension behaviour of the SNPs. **a** The zeta potential of SNPs (yellow) and an aqueous SNP-graphene dispersion (blue), respectively. **b** The surface tension of an aqueous solution of the SNPs (yellow) compared with that of water (grey) and the surface energy of graphene (grey)[20] (Paper III).

4.2 Graphene composite films

4.2.1 Fabrication and optimization of the films

Plasticization study of the starch films

The film-forming characteristics of starch were investigated with varied sorbitol content (**Figure 43**). In general, films and coatings made from starch, and many other common polysaccharides (e.g. cellulose, alginate, chitosan) are inherently brittle and fragile after drying. To increase the plasticization of the starch, sorbitol was added as a plasticizer during the gelatinization of starch to improve the film formation. Although plasticizers improve the structural properties of starch films, they can have two opposite effects on the barrier properties. On the one hand, the plasticizer can disrupt the interaction between polysaccharide chains and increase their mobility. However, this results in open pathways and impair the barrier properties. On the other hand, the plasticizer can also potentially reduce native defects in the film, thus improving the barrier properties locally. Therefore, to minimize the adverse effects on the barrier properties, a foldable film with the lowest amount of plasticizer content is preferred. This film was found at a starch:sorbitol mass ratio of 5:3, which amounts to 60% of starch or 38 wt% of total weight.

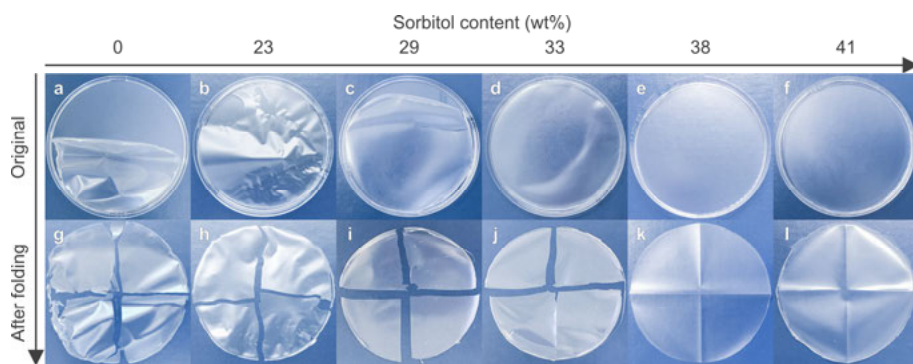


Figure 43. Optimization of the starch/SNP-graphene composite films with varied sorbitol content 0-41 wt%. The starch films with varied sorbitol concentration before (top row 1-6) and after folding tests (bottom row 7-12). The starch film with 38 wt% sorbitol demonstrated the lowest sorbitol content needed to achieve smooth and foldable films (**Paper III**).

Cross-section analysis of the starch films

To gain insight into the structural features of the starch films after the addition of sorbitol, the cross-section of the films was investigated by SEM (**Figure 44**). The surface of the cross-section for the starch film (**Figure 44a**) was free from residual starch granules, thus indicating sufficient gelatinization time and temperature at which the intermolecular hydrogen bonds between polysaccharide chains were disrupted. However, the surface was heterogeneous with local regions of varied roughness and smoothness. The plasticized starch films (**Figure 44b**), in contrast, showed an overall homogenous and smooth surface with oriented structural features in-plane with the film. As a result, the starch film composition with 38 wt% sorbitol serves as a suitable polymer matrix for composite films.

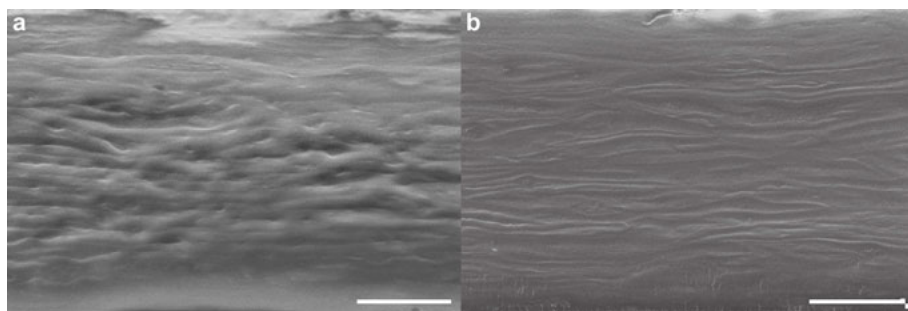


Figure 44. SEM cross-section analysis of the structural features of the starch films with the addition of sorbitol. **a** Starch film reference. **b** Starch film with 38 wt% sorbitol. Scale bars: 10 μm .

4.2.2 Graphene distribution in the composite films

Based on the plasticization condition, the SNP-graphene dispersion (**Paper III**) was mixed with the plasticized starch gel that was adjusted accordingly. The starch/SNP-graphene composite films were dried after 3 days and peeled off (**Figure 45a,b**). Similarly, these starch/SNP-graphene composite films also demonstrated a smooth surface and elasticity.

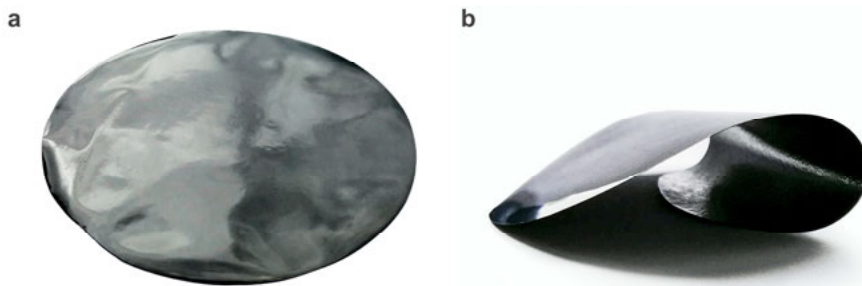


Figure 45. Photographs of the starch/SNP-graphene composite films. **a** Top-side view. **b** Side-view of a rolled film demonstrating the elasticity.

To gain insight into the graphene distribution and morphology within the starch/SNP-graphene composite films, cross-section analysis of the films was also performed by SEM and Raman spectroscopy (**Figure 46**). Along the cross-section in each film, the incorporated SNP-graphene sheets were uniformly distributed, both buried deep inside the film as well as partly protruded out from the surface (**Figure 46a,c,e**). These graphene sheets were outstretched with a high aspect ratio that was consistent with the particle size analysis of the graphene sheets in the dispersion ($\sim 3.4 \mu\text{m}$ lateral size/ $\sim 5 \text{ nm}$ thickness). Furthermore, the graphene sheets were aligned in-plane with the film, thus providing the largest surface area possible perpendicular to the gas diffusion direction. The high aspect ratio and the parallel orientation are two relevant factors that contribute to a denser network of graphene with extended tortuous pathways. Indeed, when the graphene content in the films increased (0.75 wt%, 1.5 wt%, 3.0 wt%), the density and tortuosity also increased. In addition, a graphene-rich region was formed at the bottom of the film with the highest graphene content (3.0 wt%). The SEM analysis was further supported with Raman mapping over the cross-sections to map the chemical distributions of graphene (blue) and starch (yellow) in the films (**Figure 46b,d,f**). When the graphene content increased, the relative Raman intensity of graphene was enhanced in proportion to the graphene content and eventually dominated the entire area. Although the starch fraction (60.6 wt%) in the film was larger than the graphene fraction (3.0 wt%), the backscattered light from the starch was relatively weaker. The graphene-rich region showed the highest Raman intensity. As a result, the mapping of the chemical compositions was consistent with the structural features observed in the SEM analysis.

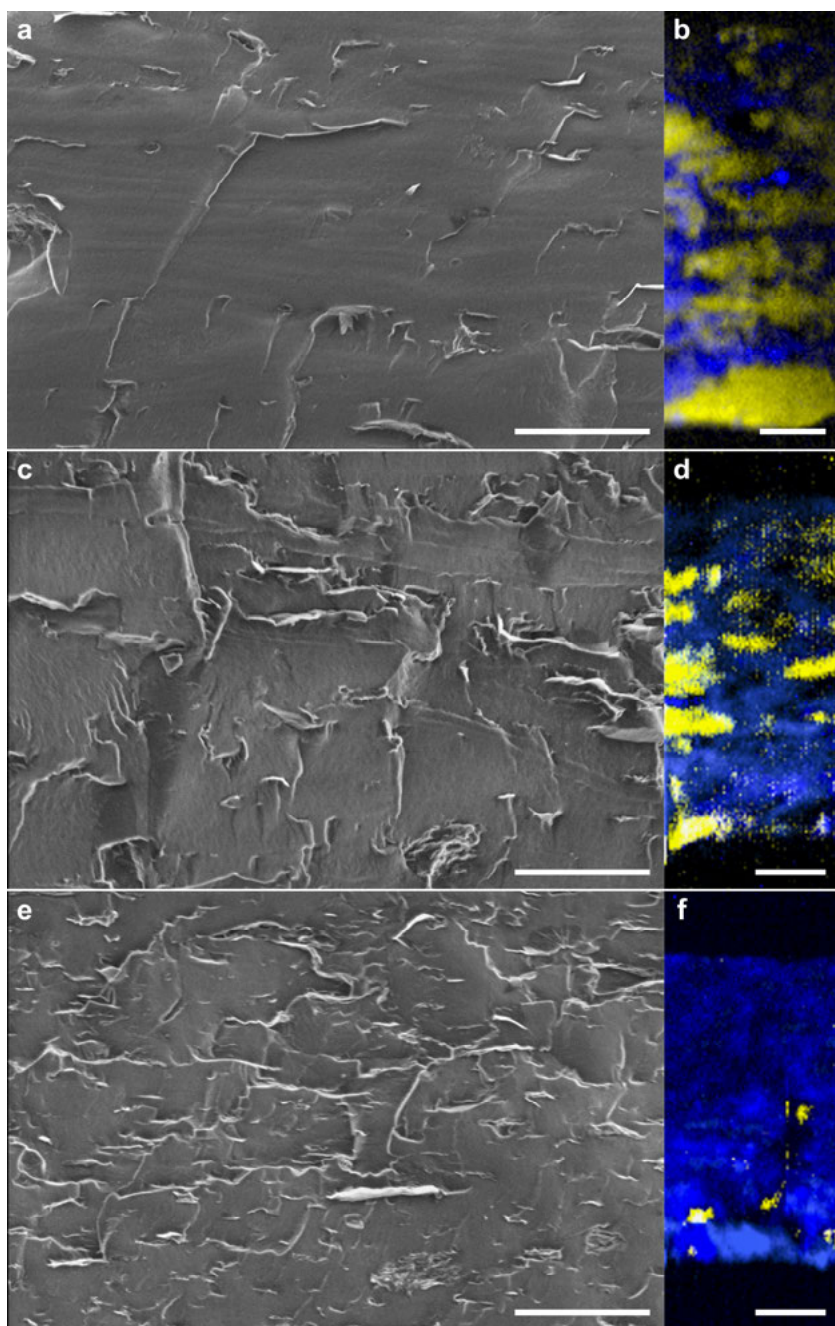


Figure 46. Graphene distribution and structural configuration within the starch/SNP-graphene composite films. From top row to bottom is the graphene content in the films: **a-b** 0.75 w%. **c-d** 1.5 wt%. **e-f** 3.0 wt%. From left to right column: **Left** SEM images of the cross-section. Scale bar 5 μm . **Right** Raman mapping of the graphene and the starch components. Scale bar 10 μm (**Paper III**).

4.2.3 Raman study on the graphene-matrix interaction

Statistical analysis of the Raman spectra

Interestingly, despite being the same incorporated SNP-graphene sheets into the starch matrix, the buried graphene sheets (blue) located deep inside the film showed distinctly different Raman spectra compared with the protruded graphene sheets (cyan) in terms of the G peak and the D peak (**Figure 47a**). These Raman spectra were averaged from the Raman mapping of the starch/SNP-graphene composite film with the highest graphene content 3.0 wt% (**Figure 47b**) and correlated well with the morphology observed in the magnified SEM image (**Figure 47c**). Since the G peak is associated with the relative motion of sp^2 -hybridized carbon atoms in the aromatic ring, the peak position and shape are therefore sensitive to stress. To estimate the degree of stress, the G peak position, FWHM, and intensity ratio $I(D)/I(G)$ were calculated based on statistical histograms (**Table 3**). The widest peak shift and peak broadening of the G peak for the buried graphene reflect a strong compression-induced effect[147]. This effect can be explained by the compressive stress transferred from the starch matrix onto the graphene sheets, thus increasing the vibration frequency. As a result, these findings indicate a dense network of incorporated SNP-graphene sheets with strong interfacial interaction with the starch matrix.

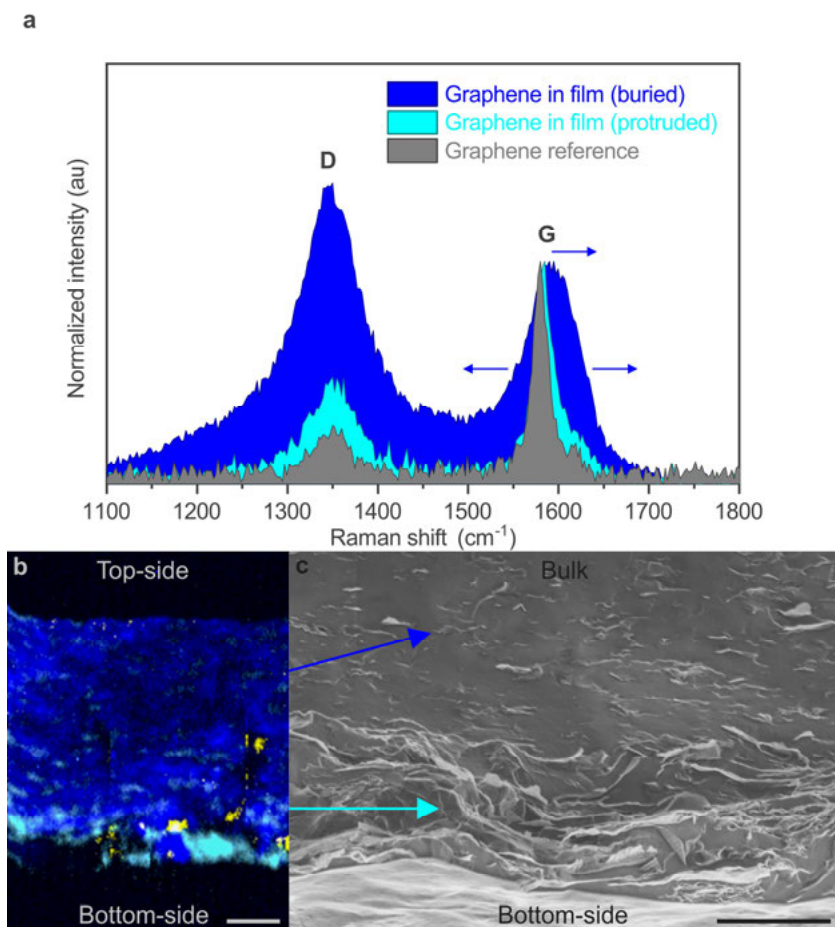


Figure 47. Raman and SEM analysis of the graphene-matrix interaction. **a** Raman spectra of buried graphene sheets (blue) and protruded graphene sheets (cyan) compared with a pure graphene reference supported on a Si/SiO₂ substrate (grey). **b** Raman mapping of starch/SNP-graphene composite film with 3.0 wt% graphene. Scale bar: 10 μm . **c** Magnified SEM image of the film cross-section with arrows pointing to examples of the buried graphene sheets (blue arrow) and the protruded graphene sheets (cyan arrow). Scale bar: 5 μm (**Paper III**).

Table 3. Statistical Raman data for the graphene sheets within the starch/SNP-graphene composite film (3.0 wt%)

Raman spectra	Peak position (G)	FWHM (G)	I(D)/I(G)
	(cm ⁻¹)	(cm ⁻¹)	
Buried graphene	1587 \pm 3.5	73	1.29
Protruded graphene	1581 \pm 1.7	29	0.77
Graphene reference	1583 \pm 1.7	20	0.58

Re-constructed Raman mapping of the compression-induced effects

To further visualize the statistical distribution of the compression-induced effects, the Raman mapping for the G peak position, the D peak position, and the intensity ratio $I(D)/I(G)$ were reconstructed (**Figure 48**). Since the G peak is associated with the relative motion of the sp^2 -hybridized carbon atoms, the width of the peak shifts can provide useful indications on the degree of compressive stress. In the colour map for the G peak position (**Figure 48a**), a wide variation up to $\sim 1593\text{ cm}^{-1}$ (yellow) was observed deep inside the film originated to the buried graphene, while in contrast, a more constant peak position around 1580 cm^{-1} (blue) was observed in the bottom of the film originated to the protruded graphene. The degree of compressive stress was relatively higher for the buried graphene than the protruded. For the D peak position (**Figure 48b**), the position at 1350 cm^{-1} (green) was constant across the entire film, consistent with the Raman analysis. On the other hand, since the D peak is activated by disorders, the intensity ratio $I(D)/I(G)$ provide useful information on the degree of disorder (**Figure 48c**). The highest degree of disorder up to ~ 1.4 (yellow) was distributed uniformly across the whole film and represented boundary effects, such as graphene edges[120]. The intensity from the boundary effects created highly oriented lines in-plane with the film. These lines originating from the graphene sheets suggest a continuous and uniformly distributed graphene network. Overall, the network of the SNP-graphene sheets in the film plays an important role in the gas barrier and the electrical conductivity.

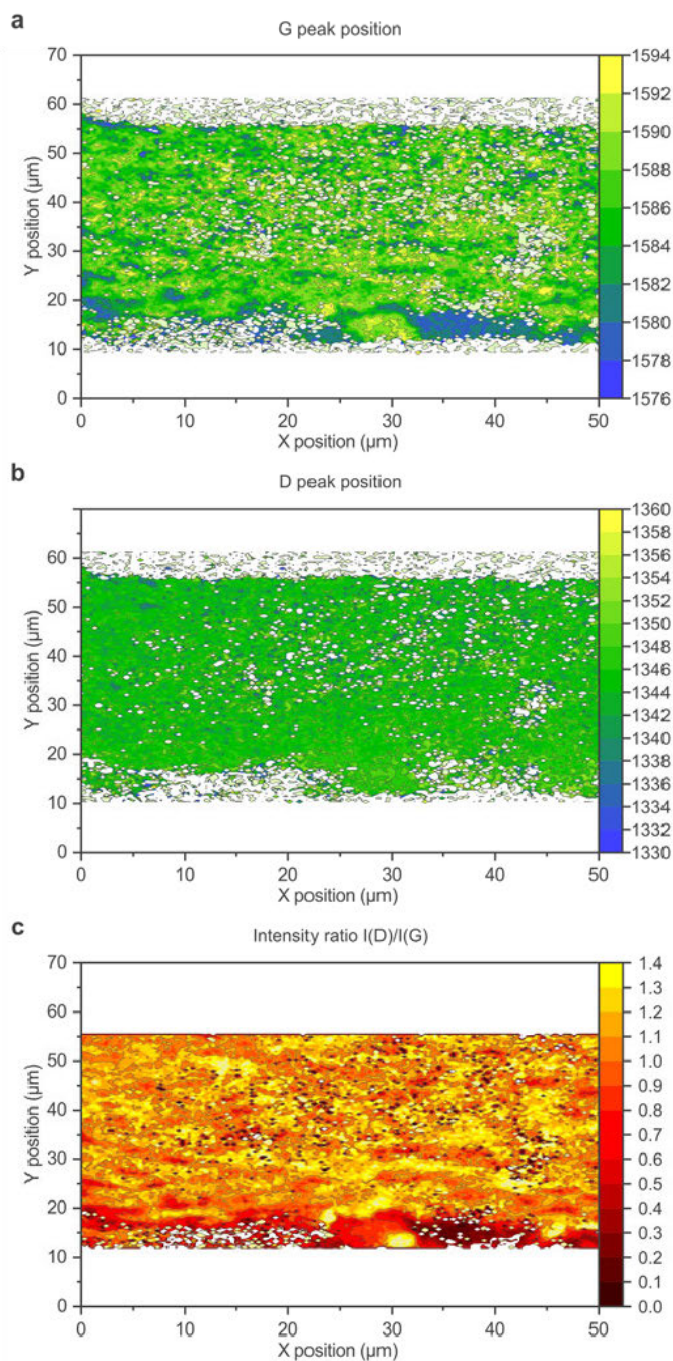


Figure 48. Reconstructed Raman mapping of the starch/SNP-graphene composite film 3.0 wt%, showing the distribution and variation of the Raman peaks associated with graphene. **a** The G peak position. **b** The D peak position. **c** The intensity ratio $I(D)/I(G)$ (**Paper III**).

4.2.4 Physicochemical properties of composite films

FT-IR analysis

The molecular interactions between the components in the starch/SNP-graphene composite films were investigated by FT-IR (**Figure 49**). The film-forming properties of the starch polymer matrix were maintained even after the incorporation of SNP-graphene sheets (**Figure 49a**). Moreover, the starch/SNP-graphene composite films were also foldable. In the FT-IR spectra (**Figure 49b**), the peak at 1572 cm^{-1} is attributed to graphene (blue solid line), while the 995 cm^{-1} to starch (yellow solid line). The broad peak around 3303 cm^{-1} (O—H stretching of free, intra-, and intermolecular interactions) is commonly used to probe the hydrogen bonding between the polysaccharide chains of starch. This peak was shifted towards the shorter wavenumbers from 3303 cm^{-1} down to 3285 cm^{-1} (-18 cm^{-1}) after the starch film was plasticized with sorbitol and from 3303 down to 3281 cm^{-1} (-22 cm^{-1}) after SNP-graphene sheets were incorporated. As a result, these relative downshifts reflect changes in the intermolecular vibrations that can be attributed to the stronger hydrogen bonding between the sorbitol and the starch in the composite films[148].

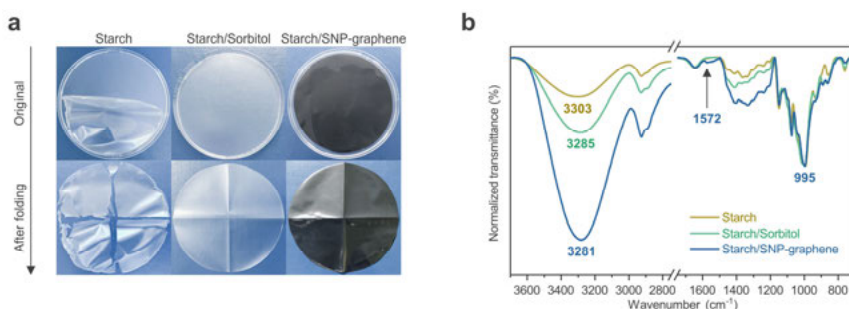


Figure 49. Molecular interactions in the starch/SNP-graphene composite films. **a** Photographs of the starch film, the plasticized starch film with sorbitol, and starch/SNP-graphene composite film before (top row) and after folding (bottom row). **b** FT-IR spectra of the films with spectroscopic features of starch and graphene, respectively (**Paper III**).

Thermal properties

The thermal stability and solid content of the composite films were further investigated by TGA (**Figure 50a**). The graphene content in the films was determined to be 2.6 wt% (slightly lower than the expected 3.0 wt%) based on the residual weight at $700\text{ }^{\circ}\text{C}$ (**Paper III**). Moreover, the thermal stability of the plasticized starch films and the starch/SNP-graphene films was slightly enhanced from $314\text{ }^{\circ}\text{C}$ to $326\text{ }^{\circ}\text{C}$ ($12\text{ }^{\circ}\text{C}$) (**Figure 50b**). This could be

attributed to the stronger hydrogen bonding between the sorbitol and the starch as well as the presence of graphene.

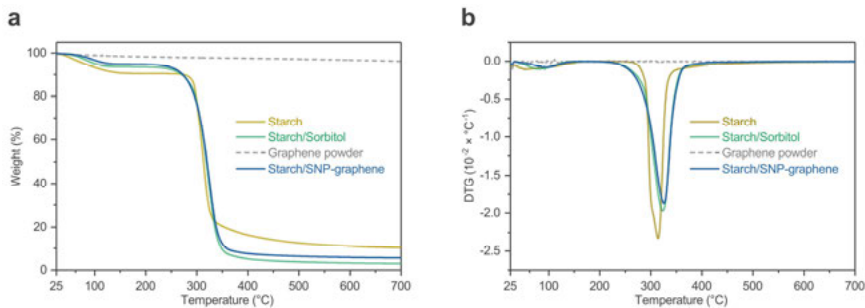


Figure 50. Thermal decomposition of the starch/SNP-graphene composite films. **a** TGA curves of the films and a starting graphene powder for reference (grey dashed line). **b** DTG curves showing the peak temperature at which the decomposition rate is highest (**Paper III**).

4.3 Graphene composite applications

4.3.1 Oxygen and water vapour permeability

To benchmark the gas barrier performance between films made from different materials, the gas transmission rates are first considered normalized to the film thickness and the partial pressure differences. Furthermore, classifications for the barrier performance are suggested based on the range of commercial polymers, compiled from the literature (**Table 4**). For instance, a barrier material that is rated as “very high” has OP values below 40 cm³ μm m⁻² day⁻¹ atm⁻¹ and WVP values below 40 g μm m⁻² day⁻¹ kPa⁻¹. On the other hand, a “poor” barrier material has an OP above 40,000 cm³ μm m⁻² day⁻¹ atm⁻¹ or a WVP above 3,000 g μm m⁻² day⁻¹ kPa⁻¹.

Table 4. Barrier performance ratings of common petrochemical-based commercial polymer films based on their OP and WVP, respectively[149,150]

Rating	OP*	Examples	WVP†	Examples
Very high	<40	EVOH	<40	HDPE, PVDC
High	40-400	PVDC	40-400	LDPE
Medium	400-4,000	PET	400-1,000	PS
Low	4,000-40,000	PVC	1,000-3,000	PLA
Poor	>40,000	PP	>3,000	PVOH

*: cm³ μm m⁻² day⁻¹ atm⁻¹, †: g μm m⁻² day⁻¹ kPa⁻¹

The gas barrier performance of the starch/SNP-graphene composite films based on aqueous SNP-graphene dispersion (**Paper III**) was evaluated using instruments (**Figure 51**). For the oxygen permeability, the OTR was measured using a MOCON OX-TRAN instrument following the ASTM F1927-14 standard. Similarly, for the water vapour permeability, the WVTR was measured using a MOCON PERMATRAN instrument following the ISO 15106-1 standard. Accordingly, all measurements were performed under the condition 23 °C and 50% RH. For the OTR, an additional condition at a higher humidity was also measured (23 °C and 80% RH). As the graphene content in the films was increased from 0 and up to 3.0 wt%, the OP was substantially reduced from 81 down to 21 cm³ μm m⁻² day⁻¹ atm⁻¹ (74.3% reduction) under 50% RH and from 14,003 down to 4,180 cm³ μm m⁻² day⁻¹ atm⁻¹ (70.2% reduction) under the higher humidity condition 80% RH (**Figure 51a**). The absolute value of the OP under 50% RH corresponds to ‘very high’ in the benchmark of barrier performance ratings (**Table 4**). In general, the barrier performance of starch, as many other hygroscopic polymers, is impeded by humidity. At higher humidity, the moisture uptake of the starch polysaccharide chains is accelerated and eventually disrupts their partial crystallinity[151]. This leads to swelling and loss of the starch native oxygen barrier properties. Nonetheless, in this thesis work, the oxygen barrier performance of starch was consistently enhanced by the incorporated SNP-graphene sheets, even under the higher humidity condition. This indicates that graphene, when incorporated as a hydrophobic and impermeable filler, reduces the moisture uptake of starch. Given that the graphene is well-mixed within the starch polymer matrix, the resulting film is also expected to function as a water vapour barrier. Indeed, with the same films, the increase in graphene content was also accompanied by a substantial reduction of the WVP from 852 down to 186 g μm m⁻² day⁻¹ kPa⁻¹ (78.2% reduction) under 50% RH (**Figure 51b**). This absolute value of the WVP corresponds to ‘high’ in the barrier performance ratings. As a result, the reduction of both the OP and the WVP indicates that the incorporated SNP-graphene sheets, when increased in content, successively formed a denser network within the starch matrix. These simultaneous improvements of the barrier performance can be correlated to the increased tortuosity in the films, as confirmed by the SEM and Raman analysis.

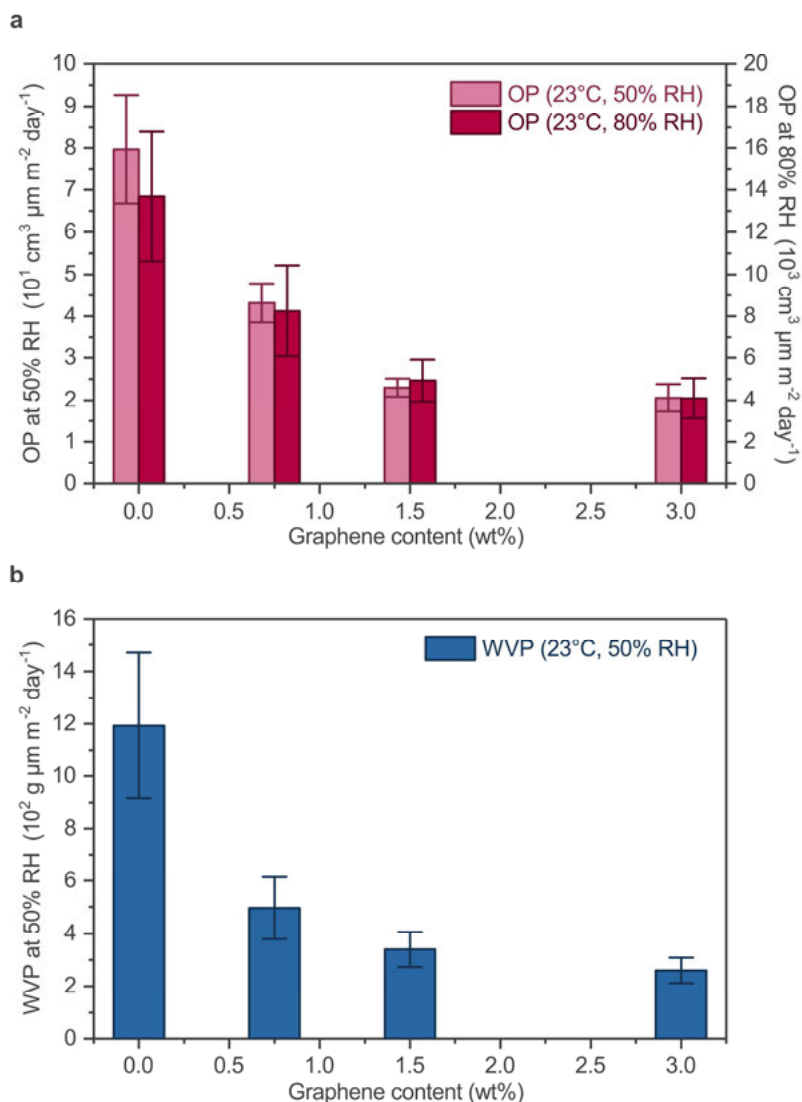


Figure 51. The barrier performance of the starch/SNP-graphene composite films with graphene content 0.0-3.0 wt%. **a** The OP as a function of the graphene content at 23 °C 50% RH (light red) and 80% RH (dark red), respectively. **b** The WVP as a function of the graphene content at 23 °C 50% RH (blue) (**Paper III**).

To the best of my knowledge, achieving a simultaneous reduction of both the OP and the WVP with the same film is unusual, especially with that made from bio-based polymers or a single coating formulation. The reduction of the OP and the WVP for starch-based composite films are among the highest reported in the literature (**Table 5**). In this thesis work, the barrier performance of the starch/SNP-graphene films is comparable to those of EVOH and PVDC (OP $\sim 20 \text{ cm}^3 \mu\text{m m}^{-2} \text{ day}^{-1} \text{ atm}^{-1}$), and to those of LDPE and PP (WVP ~ 150

g $\mu\text{m m}^{-2} \text{ day}^{-1} \text{ kPa}^{-1}$). The combined OP and WVP values make the starch/SNP-graphene films superior to most bio-based and biodegradable polymers, and on par with many commercial petrochemical-based polymers in terms of barrier performance. The starch/SNP-graphene perform as both oxygen and water vapour barrier simultaneously, while existing commercial films are optimized for one of these gases, thus requiring multi-layer sandwich structures.

Table 5. Gas barrier performance of starch-based composite films

Filler	Content (wt%)	OP (% reduction)	WVP (% reduction)	References
Graphene	3	74.3*	78.2*	This work
Graphene	3	70.2†		This work
RGO	1	66.0§		[152]
GO	1	44.0§		[152]
GO	4		43.7§	[52]
RGO	8		34.6§	[52]
RGO	1.774		26.7§	[53]
Graphene	3		24.1‡	[153]
GO	1		22.2§	[154]
Graphene	2.5		12.6‡	[155]

*, 23 °C/50% RH, †, 23 °C/80% RH, ‡, 25 °C/50% RH, §, 25 °C/75% RH

Thus far, research efforts to achieve multifunctional bio-based barrier films by incorporating carbon-based fillers have reduced the permeability of only one of the gases (oxygen and water vapour), while the other is permeated. Likewise, most commercial polymers for packaging, including the petrochemical-based, also have a limited function as either an oxygen barrier (e.g. EVOH) or a water vapour barrier (e.g. HDPE). Currently, while the common petrochemical-based polymers offer just one or the other barrier, PVDC could function as both oxygen and water vapour barriers. However, even though PVDC films have been used in the food-packaging industry for decades, this polymer is currently not recyclable at scale. Furthermore, the use in the industries is also discouraged by more stringent regulations due to its potential toxic effects on the environment and human health[156]. Sustainable alternatives are needed. However, to achieve combined gas barrier properties that meet the requirement for food packaging at an industrial scale, multi-layered films made from different coating formulations of barriers are needed. Therefore, the single formulation of bio-based and biodegradable starch incorporated with graphene is an attractive approach for combined gas

barriers, and when optimized, could be competitive with the conventional packaging films.

4.3.2 Electrical conductivity

The interconnected graphene network within the starch/SNP-graphene composite films leading to the improved gas barrier performance motivated an investigation on the electrical conductivity as a corollary result. To determine the electrical conductivity of the starch/SNP-graphene composite films, the sheet resistance was measured by the four-point probe method as described in chapter (3.3.5). The films with a graphene content in the range of 0.0-0.75 wt% were initially non-conductive, due to the large fraction of insulating sorbitol and starch (**Figure 52**). Nonetheless, when the graphene content was increased from 1.5 wt% to 3.0 wt%, the electrical conductivity of the film was substantially improved from 0.02 up to 9.5 S m^{-1} , thus indicating an interconnected network of graphene. To the best of my knowledge, the obtained electrical conductivity value is among the highest when compared with similar starch-based composite films reported in the literature (**Table 6**). For instance, 2.2 S m^{-1} has been achieved with graphene at extremely high content (25 wt%)[157] and 1 S m^{-1} with RGO (1 wt%)[52]. In this thesis work, the unprecedented electrical conductivity value achieved with relatively low graphene content (3.0 wt%) could be attributed to the compatibility between the incorporated SNP-graphene sheets and the starch matrix, thus leading to the efficient formation of a graphene network that provides conduction paths for electrons.

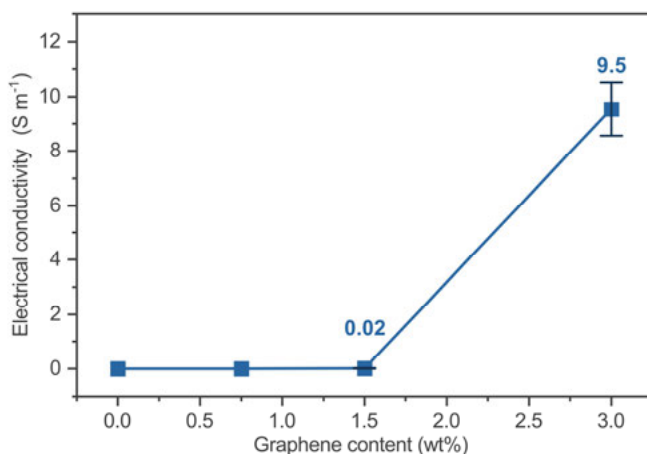


Figure 52. The electrical conductivity of the starch/SNP-graphene films with varied graphene content.

Table 6. Electrical conductivity of starch-based composite films with different carbon materials

Filler	Content (wt%)	Conductivity (S m ⁻¹)	Reference
Graphene	3	9.5	This work
Graphene	25	2.2*	[157]
RGO	2	1.0	[52]
RGO	1.774	0.097	[53]
Graphene	2	0.037 [†]	[158]
RGO	5	0.0017	[54]
RGO	5	0.0011	[159]
RGO	5	0.000032	[160]

*: at 10 Hz, [†]: at 10 kHz

4.4 Inkjet printable graphene inks

4.4.1 Formulation of SNP-graphene inks

To obtain inkjet printable SNP-graphene inks, the concentrated SNP-graphene dispersion (**Paper III**) was modified to meet the physical and the rheological requirements for the specific inkjet nozzles. The printability and drop formation from the nozzles was predicted by the inverse Ohnesorge number ($Z^{-1} = Oh = \sqrt{We/Re}$) [100]. Ideally, the ink is considered printable when the Z value is within $1 < Z < 10$. For this purpose, the surface tension and viscosity of the ink were the two most relevant parameters. The role of the SNPs, in addition to dispersing graphene in water, also lowers the surface tension of water from a value of 72.3 down to an average of ~ 58 mN m⁻¹, as shown in chapter (4.1.10), thus making the dispersion inherently suitable for stable drop formation. Therefore, the surface tension of the ink was adjusted without the need for additional surfactants, thus making the ink formulation surfactant-free and consequently eliminating the general complications that arise from surface migrations by these surface-active molecules. For the adjustment of the viscosity, a suitable amount of 1 wt% propylene glycol was added to the SNP-graphene dispersion that increased the viscosity from 1 mPa s⁻¹ to 5 mPa s⁻¹ (**Figure 53a**). To ensure stable viscosity of the ink during the piezoelectric ejection from the cartridges, the shear thinning behaviour of the ink was investigated at different shear rates (**Figure 53b**). The viscosity of the ink remained constant over the full range of shear rates tested. Overall, after

adjusting the physical and the rheological parameters, the ink formulation had a Z value of ~ 3.5 that is suitable for inkjet printing. This value fits well within the green region, known as the parameter space of inkjet printable fluids (**Figure 53c**). In addition, the formulated SNP-graphene ink remained stable over several weeks without signs of precipitation. Furthermore, the stability of the ink inside the cartridge was investigated after consecutive days of printing and no degradation of the jetting behaviour or the performance was observed.

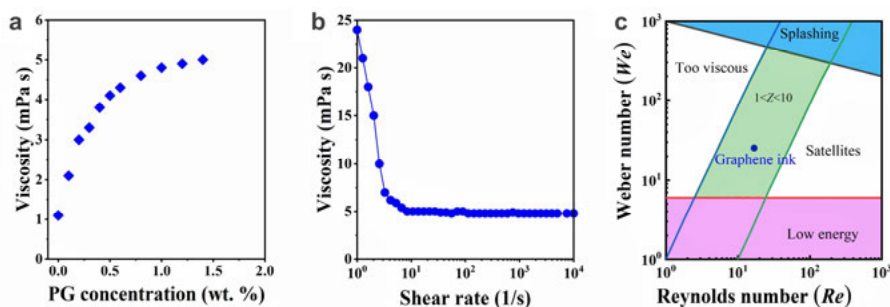
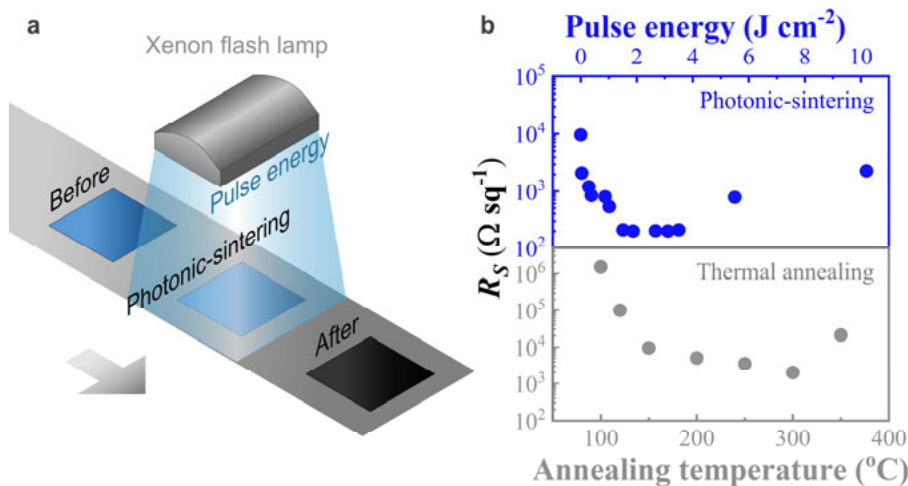


Figure 53. Formulation of SNP-graphene inks. **a** The change in viscosity with the propylene glycol concentration in the inks. **b** The change in viscosity with shear rates at the propylene glycol concentration of 1 wt%. **c** The dimensionless Z value of the graphene inks in the Weber number plotted against the Reynolds number (**Paper IV**).

4.4.2 Post-treatment conditions

To improve the electrical conductivity of the printed SNP-graphene composite films, the sheet resistance, R_s , was investigated with photonic pulse energy (**Figure 54a**). In addition, this photonic-sintering method (blue circles, top row) was compared to a conventional thermal annealing method in a convection oven (grey circles, bottom row) (**Figure 54b**). For this purpose, a set of two films were printed (4 layers each) on glass substrates. The film thickness measured 205 ± 25 nm (using 20 μ m drop-spacing). For the thermal annealing method, the R_s was evaluated as a function of the temperature between 100-350 $^{\circ}$ C. As the temperature was raised to 300 $^{\circ}$ C, the R_s was gradually lowered from an order of 10^6 down to $10^3 \Omega \text{ sq}^{-1}$. The decline of the R_s could be attributed to the removal of the additives and solvents in the film, thus leading to an improved connection between the graphene sheets[14]. On the contrary, with a further rise in the temperature up to 350 $^{\circ}$ C, the R_s was increased. This increase could be attributed to the decomposition of the films. Therefore, thermal annealing of the films in the temperature range between 250-300 $^{\circ}$ C enabled the most efficient charge transport through the graphene network. Similarly, for the photonic-sintering method, the R_s was evaluated as a function of the photonic pulse energy from 0-10 J cm^{-2} . To prevent the

bursting of solvent bubbles during the photonic annealing process, the films were first equilibrated in an oven at 150 °C for 30 min. When the photonic pulse energy was increased from 0.0-1.5 J cm⁻², the R_s was effectively lowered from an order of 10⁵ down to 10² Ω sq⁻¹. Under the rapid photonic irradiation, the incident light is selectively absorbed by the SNP-graphene sheets and consequently converted to heat that can promote the removal of additives and solvents as well as densification of the graphene network[161], thus leading to the lower value of the R_s . A SimPulse simulation tool was used to estimate the temperature associated with the photonic pulse energy. This photonic pulse energy of 1.5 J cm⁻² corresponds to an annealing temperature of 250 °C on the film surface, while 50 °C on the underlying substrate. As a result, this rapid irradiation was sufficient to initiate the removal of the additives and solvents, thus leading to the percolating graphene network. An optimal window of photonic pulse energy was identified between 1.5-2.0 J cm⁻², by which the lowest value of R_s was achieved. With higher photonic pulse energy, the corresponding temperature was >400 °C and also caused an increase in the sheet resistance. Overall, the value of the R_s in the optimal region was lowered down to 200 ± 15 Ω sq⁻¹, thus yielding an electrical conductivity value of 2.4·10⁴ S m⁻¹.



4.4.3 Surface morphology

To visualize the effects of the photonic annealing on the printed SNP-graphene composite films (205 ± 25 nm thickness), the surface morphology was investigated by SEM and the degree of disorder by Raman spectroscopy (**Figure 55**). The photonic cured film was compared with the thermally annealed film and a non-treated film. For the non-treated film (**Figure 55a**), overlapping SNP-graphene sheets were observed on the film surface. When the film was thermally annealed at $250\text{ }^{\circ}\text{C}$ for 1 h (**Figure 55b**), additional nanometer- to micrometer-sized pores were formed uniformly on the surface by the decomposition and evaporation of additives. For the photonic annealed film (**Figure 55c**), more SNP-graphene sheets emerged on the film surface with visible graphene surface features and interconnection. In addition, few microscale tears were also observed as an effect of the more rapid decomposition of the additives, thus inducing local stress. In the corresponding Raman analysis, the peak intensity ratio of the G peak (1580 cm^{-1}) over the D peak (1350 cm^{-1}) was calculated to investigate the degree of disorder (**Figure 55d**). The degree of disorder was lowered by the photonic-sintering method. This trend is associated with a lower density of disorders and restoration of the graphitic nature of graphene[109].

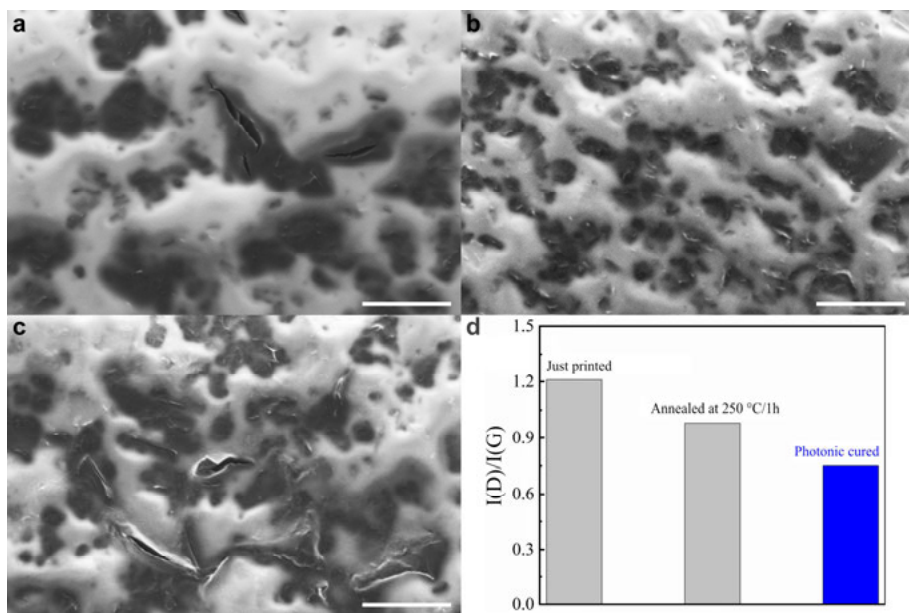


Figure 55. SEM and Raman analysis of the printed SNP-graphene films. **a** Just printed film. **b** Thermally annealed film at $250\text{ }^{\circ}\text{C}$ for 1 hour. **c** Photonic cured film. **d** Raman analysis of the intensity ratio $I(D)/I(G)$ for all the films (**Paper IV**).

4.4.4 Electrical conductivity

The application and mechanical flexibility of the photonic annealed SNP-graphene film were demonstrated by a simple electronic circuit on a flexible PET substrate (**Figure 56a**). On this circuit, an LED was mounted between two parallel electrodes made from the printed SNP-graphene films and when a proper voltage was applied, the LED was illuminated (**Figure 56a inset 1 and 2**), thus indicating conduction pathways for electrons. Furthermore, the brightness of the LED remained constant after bending the electronic circuit. To study the mechanical behaviour further, the variation in line resistance of these electrodes with bending cycles was investigated was measured over 1000 bending cycles at two radius of curvatures, 2 and 12 mm. After 1000 bending cycles, the line resistance for the larger bending radius of curvature 12 mm (less mechanical stress) only showed a deviation of 2.6%, while the smaller radius of curvature 2 mm (more mechanical stress) showed 13%. The increase in resistance (13%) with a smaller radius of curvature (2 mm) could be attributed to the formation of wrinkles on the films after more extensive mechanical stress. The electrical conductivity ($2.4 \cdot 10^4 \text{ S m}^{-1}$) achieved by the SNP-graphene inks after photonic annealing was compared with those reported for other types of formulations and graphene types (**Figure 56b**). These graphene types include liquid-phase exfoliated[14,161–164], electrochemically exfoliated[165,166], and RGO[167,168]. Among these types, the two highest reported electrical conductivity values ($\sim 4 \cdot 10^4 \text{ S m}^{-1}$) were achieved by the liquid-phase[14] and electrochemically[166] exfoliated graphene inks, respectively. Another report on rapid photonic annealed graphene ink reported an electrical conductivity of $2.5 \cdot 10^4 \text{ S m}^{-1}$ [164]. However, these inks were in general formulated using organic solvents that are toxic or consist of several additives, such as surfactants, viscosity modifiers, and binders. Therefore, reported in this thesis work, the formulation of water-based SNP-graphene inks combined with rapid photonic annealing provides a high electrical conductivity value that is on par with the highest reported in the literature, while offering an efficient and environmentally friendly approach.

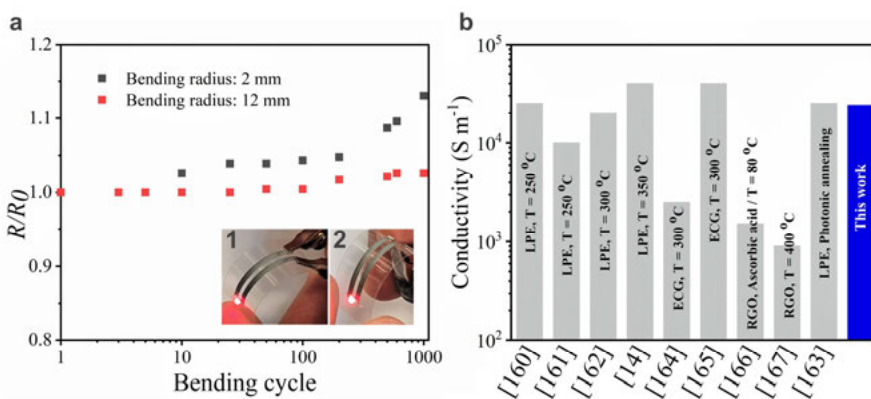


Figure 56. A demonstrator circuit and a comparison of electrical conductivity of SNP-graphene ink with previously reported inks. **a** Change of normalized line resistance (R/R_0) of the graphene electrodes with different bending cycles. Inset: **1** Large bending radius of curvature 12 mm (less mechanical stress). **2** smaller radius of curvature 2 mm (more mechanical stress). **b** The electrical conductivity value of the SNP-graphene ink after photonic annealing compared with those reported in the literature (Paper IV).

5 Conclusions and outlook

Aqueous graphene dispersions that are formulated with the aid of bio-based dispersing agents as alternatives to conventional synthetic molecules have come a long way. However, not all bio-based dispersing agents are suitable for large-scale applications or compatible with an intended coating formulation. Moreover, specific applications require tailored graphene qualities, such as morphology, surface chemistry, and stability among many others.

In this thesis work, the aim was to gain a deeper understanding of the preparation and the use of aqueous graphene dispersions for paper-packaging applications. In an early stage, initial experience with amphiphilic molecules was a crucial stepping stone towards understanding aqueous graphene dispersions. Relatively small molecules with high surface activity, such as conventional surfactants, could not fulfil the expectations of aqueous graphene dispersions for barrier films. Although surfactants have been essential in aiding the dispersion of graphene in water, they are often needed in excess and therefore tend to migrate to the interfaces within the resulting composite films, thus introducing defects that impair the barrier. Furthermore, removing the excess still counteracts the benefits brought by graphene. Therefore, these challenges led to the quest for alternatives beyond surfactants, such as bio-based materials. Among many bio-based materials, FMN and starch were selected as dispersing agents for graphene in water, both have their own unique set of properties.

The FMN biomolecule was found to disperse graphene in water via π - π interactions, thus changing the electronic configuration of the isoalloxazine aromatic ring system of the FMN molecule. This type of interaction was understood by spectroscopic blue shifts of the FMN bands in the UV-Vis absorption spectra. A model was proposed that describes FMN molecules adsorption on the graphene surface in a parallel conformation with their isoalloxazine ring system stacked with the graphene surface. This model is further supported by changes in the vibration modes associated with the binding sites on the isoalloxazine and enhanced thermal stability of the graphene. The starch, a complex long-chained biopolymer was processed into SNPs that were found to physically adsorb on the graphene surface and aid the dispersion of graphene in water to at least 3 mg mL⁻¹. The colloidal stability of the SNP-graphene sheets with a median particle size of 3.4 μ m was

substantially improved by the presence of the SNPs in the dispersion, retaining 91.1% of the graphene concentration after 1 month of storage at room temperature. Yet, the surface charge of the SNP-graphene sheets was relatively weak at -22.9 ± 4.8 mV, thus indicating a stabilization mechanism mainly by steric hindrance and most likely in a combination with electrostatic repulsion. Moreover, the aqueous SNP-graphene dispersion was formulated to surfactant-free composite films for barrier measurements. Starch films have native oxygen gas barrier properties originating from its semicrystalline structural features when its polysaccharides chains are organized. On the other hand, the hygroscopic nature of starch impairs the water vapour gas barrier properties. Therefore, achieving a combined gas barrier against both oxygen and water vapour may strike as a seemingly contradictory challenge. Nevertheless, at a low graphene content (3.0 wt%) in the composite films, the incorporated SNP-graphene sheets reduced the OP as well as the WVP simultaneously by over 70% at 23 °C 50% RH (and additionally at 80% RH for the OP). The absolute values of the OP and the WVP are comparable to that of common petrochemical-based plastics used in food packaging, such as EVOH and LDPE, respectively. Motivated by the gas barrier properties, the aqueous SNP-graphene dispersion was also formulated to electrically conductive inks with long-term storage and stable drop formation during inkjet printing. When rapid photonic annealing was applied on the printed films, the electrical conductivity was substantially improved to $2.4 \cdot 10^4$ S m⁻¹. The rapid photonic annealing approach is applicable on a wide range of flexible substrates, including heat-sensitive polymers, such as PET. The combined gas barrier and the high electrical conductivity of these functional composite films demonstrate the versatility of the aqueous SNP-graphene dispersion and its potential for barrier composite films that can meet current and future demands of the packaging industry.

6 Sammanfattning på Svenska

Vattenhaltiga grafendispersioner som är formulerade med hjälp av biobaserade dispergeringsmedel som alternativ till konventionella syntetiska molekyler har kommit en lång väg. Det är dock inte alla biobaserade dispergeringsmedel är lämpliga för storskaliga tillämpningar eller kompatibla med en avsedd ytbelägningsformulering. Dessutom kräver specifika tillämpningar skräddarsydda grafenkvaliteter, såsom morfologi, ytkemi och stabilitet bland många andra.

I detta avhandlingsarbete var det övergripande syftet att få en djupare förståelse för beredningen och användningen av vattenhaltiga grafendispersioner för pappersförpackningstillämpningar. I ett tidigt skede var initiala erfarenheter av amfifila molekyler en avgörande språngbräda för att förstå vattenhaltiga grafendispersioner. Relativt små molekyler med hög ytaktivitet, såsom konventionella tensider, kunde inte uppfylla förväntningarna på vattenhaltiga grafendispersioner för barriärfilmer. Även om tensider har varit avgörande för dispergeringen av grafen i vatten, behövs de ofta i överskott och tenderar därför att migrera till gränssnitten i de resulterande kompositfilmerna, vilket leder till defekter som försämrar barriären. Fördelarna med grafen hindras kraftigt av tensiderna, även efter att överskottet av tensider har avlägsnats. Dessa utmaningar ledde därför till jakten på alternativ utöver tensiderna, såsom biobaserade material. Bland många biobaserade material undersöktes FMN och stärkelse som dispergeringsmedel för grafen i vatten, båda har sin egen unika uppsättning av egenskaper.

FMN-biomolekylen visade sig dispergera grafen i vatten via π - π -interaktioner, vilket ändrade den elektroniska konfigurationen av isoalloxazin-ringsystemet i FMN-molekylen. Denna typ av interaktion förstods av spektroskopiska blåskiftningar av FMN-banden i UV-Vis-absorptionsspektra. En modell är föreslagen som beskriver FMN-molekylernas adsorption på grafenytan i en parallell konformation med deras isoalloxazin-ringsystem staplade med grafenytan. Denna modell stöds ytterligare av förändringar av vibrationslägena associerade med bindningsställena på isoalloxazin och förbättrad termisk stabilitet hos grafenet. Stärkelsen, en komplex långkedjig biopolymer, bearbetades till SNPar som visade sig fysiskt adsorbera på grafenytan och underlätta dispergeringen av grafen i vatten till minst 3 mg ml⁻¹. Den kolloidala stabiliteten hos SNP-grafenarken med en

medianpartikelstorlek på 3,4 μm förbättrades avsevärt genom närvaron av SNPar i dispersionen, vilket bibehöll 91,1% av grafenkoncentrationen efter 1 månads lagring i rumstemperatur. Ändå var zetapotentialen av SNP-grafenarken relativt svag vid $-22,9 \pm 4,8$ mV, vilket indikerar en stabiliseringsmekanism genom steriskt hinder och troligen i kombination med elektrostatisk repulsion. Dessutom formulerades den vattenhaltiga SNP-grafen-dispersionen till tensidfria kompositfilmer för barriärmätningar. Stärkelsefilmer har naturliga barriäregenskaper mot syrgas som härrör från dess semikristallina strukturella egenskaper när dess polysackaridkedjor är organiserade. Å andra sidan försämrar den hygroskopiska naturen hos stärkelsen barriäregenskaperna mot vattenånga. Att uppnå en kombinerad gasbarriär mot både syre och vattenånga är därför en till synes motsägelsefull utmaning. Hur som helst, vid ett lågt grafeninnehåll (3,0 vikt%) i kompositfilmerna, minskade de inkorporerade SNP-grafenarken OP såväl som WVP samtidigt med över 70 % vid 23 °C 50 % RH (och även vid 80 % RH för OP). De absoluta värdena för OP och WVP är jämförbara med de för vanliga petrokemiska plaster som används i livsmedelsförpackningar, såsom EVOH respektive LDPE. Motiverad av gasbarriäregenskaperna formulerades den vattenhaltiga SNP-grafen-dispersionen också till elektriskt ledande bläck med långtidslagring och stabil droppbildning under bläckstråleutskrift. När snabb fotonisk glödning applicerades på de tryckta filmerna förbättrades den elektriska ledningsförmågan avsevärt till $2,4 \cdot 10^4 \text{ S m}^{-1}$. Den snabba fotoniska glödgningsmetoden är tillämpbar på ett brett utbud av flexibla substrat, inklusive värmekänsliga polymerer, såsom PET.

Den kombinerade gasbarriären och höga elektriska ledningsförmågan i dessa funktionella kompositfilmer visar mångsidigheten hos den vattenhaltiga SNP-grafendispersionen och dess potential för barriärkompositfilmer som kan möta nuvarande och framtida krav från förpackningsindustrin.

7 Acknowledgments

In the midst of an ongoing pandemic (COVID-19), I express my sincere gratitude to all the people who have supported me and contributed to this thesis in every possible way during these unprecedented times.

During this journey, I had the honour to be guided by six supervisors, to whom I will always be grateful, for providing the opportunity to drive this project. First and foremost, I would like to acknowledge my main supervisor Anwar Ahniyaz, for all those times you were there for me even when you had no time. It was truly a pleasure to have scientific discussions with you, learn from you, and test many seemingly impossible ideas that shaped this thesis. I would also like to acknowledge my co-supervisor Abhilash Sugunan, also a passionate and creative researcher with a keen eye for details. You could discern key pieces of information when I could not. Moreover, your mentorship in the laboratory as well as in many business opportunities has taught me valuable skills. My co-supervisors at BillerudKorsnäs, Johan A. Larsson and Thomas Gillgren. I am grateful for your support and the valuable insights on gas barriers and paper packaging from an industrial perspective. Also, thank you for the opportunities to visit the production facility in Frövi as well as participate in different events with the BillrudKorsnäs team. In addition, thank you, Thomas for offering regular meetings when needed the most. Those scientific discussions as well as the mentorship helped me navigate through tortuous roads during the journey. My co-supervisors at Uppsala University, Zhi-Bin Zhang and Shi-Li Zhang. I am grateful for your support, professional network, and guidance through all stages. Thank you, Zhi-Bin, for assistance with electrical and Raman characterizations. Thank you, Shi-Li, for always being available and sharing your wisdom as well as passion for science. Moreover, I would like to acknowledge your leadership and vigilance in ensuring a healthy and safe working environment during the ongoing pandemic. Thank you all for these memorable years. I have indeed been standing on the shoulders of giants and grown wiser and more confident as a researcher.

To my co-authors on the papers, Niklas Nordgren, Jens Sommertune, Illia Dobryden, Subimal Majee, Robert Brooke, and David Nilsson. It was a pleasure to put our heads together and face seemingly impossible challenges,

and what a joy when we found a workable solution. Thank you for the fruitful collaborations. I would also like to acknowledge the Swedish Foundation for Strategic Research (SSF, grant no. FID-15-0105) and BillerudKorsnäs AB for the financial support of this project.

To all my colleagues at Uppsala University, thank you for all the scientific discussions, studies, and technical support to improve my work. Furthermore, thank you for making me feel welcomed every time I visited. To all my colleagues (past and present) at RISE, thank you for all the help, support, discussions. Your contributions to an enjoyable, inclusive, and collaborative work environment are appreciated. Thank you, Rose-Marie Larsson, for always being there for me since I joined SP (now RISE). Thanks to Jens Sommertune for teaching me confocal Raman spectroscopy and encouraged me to take the WITec Academy training program for advanced Raman instrument and software operations in Ulm, Germany. Rubén Álvarez-Asencio and Niklas Nordgren for teaching me AFM. Mikael Sundin for helping me with everything that exists in a laboratory facility, such as repairing equipment and keeping a good habit of measuring standards after every characterization. Karin Hallstensson for assistance with the SEM studies and Marie Ernstsson with the XPS studies. Andreas Fall, Åsa Blademo, and Tiffany Abitbol for fruitful collaborations on nanocellulose for graphene dispersions. I would also like to acknowledge my past managers, Andrea Fornara, Marie Sjöberg, Anna Stenemyr, Björn Gregertsen, and Jenny Adrian Meredith. All of you had a pivotal role during my PhD studies. Moreover, thank you for ensuring a healthy and safe working environment, especially during these unprecedented times. Finally, Juhanes Aydin, my present manager, thank you for the opportunity and welcome to join your unit “Additives and Binders” as a researcher. Your passion for turning science into practice and business as well as bringing people together is inspiring. I look forward to working with you and my new colleagues, learning from you all, and continuing to develop as a researcher to support our business areas.

Special thanks to Amanda, Daniel, and Zandra and your respective partners for encouragement, kindness, and making my journey brighter. Now I wish you all have an equally bright PhD journey! To my parents, words are not sufficient to describe the love and support. You have supported me in all possible ways and given me strength to move forward. Also, the support from the family of my partner from afar and during their visits is acknowledged. Finally, to my partner Natalia. It's quite a unique life experience to pursue a PhD degree at the same time and place. We have both endured hardships, but at the end of the day we lift each other. Thank you for always being there for me and sharing both the laughter and the hardships. No matter how tough a day has been, it is with you that I can end the day with a smile and start the next day grateful.

8 References

- [1] K. S. Novoselov *et al.*, “Electric Field Effect in Atomically Thin Carbon Films,” *Science*, vol. 306, no. 5696, pp. 666–669, Oct. 2004.
- [2] A. K. Geim and K. S. Novoselov, “The rise of graphene,” *Nat. Mater.*, vol. 6, no. 3, pp. 183–191, Mar. 2007.
- [3] K. S. Novoselov, V. I. Fal’ko, L. Colombo, P. R. Gellert, M. G. Schwab, and K. Kim, “A roadmap for graphene,” *Nature*, vol. 490, no. 7419, pp. 192–200, Oct. 2012.
- [4] R. Collins, “Graphene Market & 2D Materials Assessment 2021-2031.” <https://www.idtechex.com/en/research-report/graphene-market-and-2d-materials-assessment-2021-2031/789> (accessed Nov. 21, 2021).
- [5] S. V. Morozov *et al.*, “Giant Intrinsic Carrier Mobilities in Graphene and Its Bilayer,” *Phys. Rev. Lett.*, vol. 100, no. 1, p. 016602, Jan. 2008.
- [6] K. I. Bolotin *et al.*, “Ultrahigh electron mobility in suspended graphene,” *Solid State Commun.*, vol. 146, no. 9–10, pp. 351–355, Jun. 2008.
- [7] A. A. Balandin, “Thermal properties of graphene and nanostructured carbon materials,” *Nat. Mater.*, vol. 10, no. 8, pp. 569–581, Aug. 2011.
- [8] C. Lee, X. Wei, J. W. Kysar, and J. Hone, “Measurement of the Elastic Properties and Intrinsic Strength of Monolayer Graphene,” *Science*, vol. 321, no. 5887, pp. 385–388, Jul. 2008.
- [9] J. S. Bunch *et al.*, “Impermeable Atomic Membranes from Graphene Sheets,” *Nano Lett.*, vol. 8, no. 8, pp. 2458–2462, Aug. 2008.
- [10] O. Leenaerts, B. Partoens, and F. M. Peeters, “Graphene: A perfect nanoballoon,” *Appl. Phys. Lett.*, vol. 93, no. 19, p. 193107, Nov. 2008.
- [11] V. Berry, “Impermeability of graphene and its applications,” *Carbon*, vol. 62, pp. 1–10, Oct. 2013.
- [12] A. C. Ferrari *et al.*, “Science and technology roadmap for graphene, related two-dimensional crystals, and hybrid systems,” *Nanoscale*, vol. 7, no. 11, pp. 4598–4810, 2015.
- [13] B. M. Yoo, H. J. Shin, H. W. Yoon, and H. B. Park, “Graphene and graphene oxide and their uses in barrier polymers,” *J. Appl. Polym. Sci.*, vol. 131, no. 1, p. n/a-n/a, Jan. 2014.
- [14] S. Majee, M. Song, S.-L. Zhang, and Z. Zhang, “Scalable inkjet printing of shear-exfoliated graphene transparent conductive films,” *Carbon*, vol. 102, pp. 51–57, Jun. 2016.

- [15] P. Blake *et al.*, “Graphene-Based Liquid Crystal Device,” *Nano Lett.*, vol. 8, no. 6, pp. 1704–1708, Jun. 2008.
- [16] Y. Hernandez *et al.*, “High-yield production of graphene by liquid-phase exfoliation of graphite,” *Nat. Nanotechnol.*, vol. 3, no. 9, pp. 563–568, Sep. 2008.
- [17] U. Khan, H. Porwal, A. O’Neill, K. Nawaz, P. May, and J. N. Coleman, “Solvent-Exfoliated Graphene at Extremely High Concentration,” *Langmuir*, vol. 27, no. 15, pp. 9077–9082, Aug. 2011.
- [18] C.-J. Shih, S. Lin, M. S. Strano, and D. Blankschtein, “Understanding the Stabilization of Liquid-Phase-Exfoliated Graphene in Polar Solvents: Molecular Dynamics Simulations and Kinetic Theory of Colloid Aggregation,” *J. Am. Chem. Soc.*, vol. 132, no. 41, pp. 14638–14648, Oct. 2010.
- [19] D. W. Johnson, B. P. Dobson, and K. S. Coleman, “A manufacturing perspective on graphene dispersions,” *Curr. Opin. Colloid Interface Sci.*, vol. 20, no. 5–6, pp. 367–382, Oct. 2015.
- [20] S. Wang, Y. Zhang, N. Abidi, and L. Cabrales, “Wettability and Surface Free Energy of Graphene Films,” *Langmuir*, vol. 25, no. 18, pp. 11078–11081, Sep. 2009.
- [21] M. Lotya *et al.*, “Liquid Phase Production of Graphene by Exfoliation of Graphite in Surfactant/Water Solutions,” *J. Am. Chem. Soc.*, vol. 131, no. 10, pp. 3611–3620, Mar. 2009.
- [22] M. Lotya, P. J. King, U. Khan, S. De, and J. N. Coleman, “High-Concentration, Surfactant-Stabilized Graphene Dispersions,” *ACS Nano*, vol. 4, no. 6, pp. 3155–3162, Jun. 2010.
- [23] P. Ramalingam, S. T. Pusuluri, S. Periasamy, R. Veerabahu, and J. Kulandaivel, “Role of deoxy group on the high concentration of graphene in surfactant/water media,” *RSC Adv.*, vol. 3, no. 7, p. 2369, 2013.
- [24] Z. Sun, J. Masa, Z. Liu, W. Schuhmann, and M. Muhler, “Highly Concentrated Aqueous Dispersions of Graphene Exfoliated by Sodium Taurodeoxycholate: Dispersion Behavior and Potential Application as a Catalyst Support for the Oxygen-Reduction Reaction,” *Chem. - A Eur. J.*, vol. 18, no. 22, pp. 6972–6978, May 2012.
- [25] A. G. Hsieh, C. Punckt, S. Korkut, and I. A. Aksay, “Adsorption of Sodium Dodecyl Sulfate on Functionalized Graphene Measured by Conductometric Titration,” *J. Phys. Chem. B*, vol. 117, no. 26, pp. 7950–7958, Jul. 2013.
- [26] M. J. Fernández-Merino *et al.*, “Investigating the influence of surfactants on the stabilization of aqueous reduced graphene oxide dispersions and the characteristics of their composite films,” *Carbon*, vol. 50, no. 9, pp. 3184–3194, Aug. 2012.
- [27] S. M. Notley, “Highly Concentrated Aqueous Suspensions of Graphene through Ultrasonic Exfoliation with Continuous Surfactant Addition,” *Langmuir*, vol. 28, no. 40, pp. 14110–14113, Oct. 2012.

- [28] L. Guardia *et al.*, “High-throughput production of pristine graphene in an aqueous dispersion assisted by non-ionic surfactants,” *Carbon*, vol. 49, no. 5, pp. 1653–1662, Apr. 2011.
- [29] A. J. Patil, J. L. Vickery, T. B. Scott, and S. Mann, “Aqueous Stabilization and Self-Assembly of Graphene Sheets into Layered Bio-Nanocomposites using DNA,” *Adv. Mater.*, vol. 21, no. 31, pp. 3159–3164, Aug. 2009.
- [30] M. Cao *et al.*, “Direct exfoliation of graphite into graphene in aqueous solutions of amphiphilic peptides,” *J. Mater. Chem. B*, vol. 4, no. 1, pp. 152–161, 2016.
- [31] P. Laaksonen *et al.*, “Interfacial Engineering by Proteins: Exfoliation and Functionalization of Graphene by Hydrophobins,” *Angew. Chemie Int. Ed.*, vol. 49, no. 29, pp. 4946–4949, Jun. 2010.
- [32] A. Pattammattel and C. V. Kumar, “Kitchen Chemistry 101: Multigram Production of High Quality Biographene in a Blender with Edible Proteins,” *Adv. Funct. Mater.*, vol. 25, no. 45, pp. 7088–7098, Dec. 2015.
- [33] W. Yoon *et al.*, “Graphene nanoribbons formed by a sonochemical graphene unzipping using flavin mononucleotide as a template,” *Carbon*, vol. 81, no. 1, pp. 629–638, Jan. 2015.
- [34] M. Ayán-Varela *et al.*, “Achieving Extremely Concentrated Aqueous Dispersions of Graphene Flakes and Catalytically Efficient Graphene-Metal Nanoparticle Hybrids with Flavin Mononucleotide as a High-Performance Stabilizer,” *ACS Appl. Mater. Interfaces*, vol. 7, no. 19, pp. 10293–10307, May 2015.
- [35] A. Tzitzinou *et al.*, “Surfactant concentration and morphology at the surfaces of acrylic latex films,” *Prog. Org. Coatings*, vol. 35, no. 1–4, pp. 89–99, Aug. 1999.
- [36] A. Hellgren, P. Weissenborn, and K. Holmberg, “Surfactants in water-borne paints,” *Prog. Org. Coatings*, vol. 35, no. 1–4, pp. 79–87, Aug. 1999.
- [37] E. Kientz and Y. Holl, “Distribution of surfactants in latex films,” *Colloids Surfaces A Physicochem. Eng. Asp.*, vol. 78, no. C, pp. 255–270, Oct. 1993.
- [38] B. J. Roulstone, M. C. Wilkinson, and J. Hearn, “Studies on polymer latex films: II. Effect of surfactants on the water vapour permeability of polymer latex films,” *Polym. Int.*, vol. 27, no. 1, pp. 43–50, 1992.
- [39] G. Ying, “Fate, behavior and effects of surfactants and their degradation products in the environment,” *Environ. Int.*, vol. 32, no. 3, pp. 417–431, Apr. 2006.
- [40] K. Jardak, P. Drogui, and R. Daghrir, “Surfactants in aquatic and terrestrial environment: occurrence, behavior, and treatment processes,” *Environ. Sci. Pollut. Res.*, vol. 23, no. 4, pp. 3195–3216, Feb. 2016.
- [41] I. Uysal Unalan, C. Wan, S. Trabattoni, L. Piergiovanni, and S. Farris,

- “Polysaccharide-assisted rapid exfoliation of graphite platelets into high quality water-dispersible graphene sheets,” *RSC Adv.*, vol. 5, no. 34, pp. 26482–26490, 2015.
- [42] A. Hajian, S. B. Lindström, T. Pettersson, M. M. Hamed, and L. Wågberg, “Understanding the Dispersive Action of Nanocellulose for Carbon Nanomaterials,” *Nano Lett.*, vol. 17, no. 3, pp. 1439–1447, Mar. 2017.
- [43] D. Le Corre and H. Angellier-Coussy, “Preparation and application of starch nanoparticles for nanocomposites: A review,” *React. Funct. Polym.*, vol. 85, pp. 97–120, Dec. 2014.
- [44] O.-K. Kim, J. Je, J. W. Baldwin, S. Kooi, P. E. Pehrsson, and L. J. Buckley, “Solubilization of Single-Wall Carbon Nanotubes by Supramolecular Encapsulation of Helical Amylose,” *J. Am. Chem. Soc.*, vol. 125, no. 15, pp. 4426–4427, Apr. 2003.
- [45] L. Stobinski *et al.*, “Single-walled carbon nanotube–amylopectin complexes,” *Carbohydr. Polym.*, vol. 51, no. 3, pp. 311–316, Feb. 2003.
- [46] X. Cao, Y. Chen, P. R. Chang, and M. A. Huneault, “Preparation and properties of plasticized starch/multiwalled carbon nanotubes composites,” *J. Appl. Polym. Sci.*, vol. 106, no. 2, pp. 1431–1437, Oct. 2007.
- [47] Z. Liu, L. Zhao, M. Chen, and J. Yu, “Effect of carboxylate multi-walled carbon nanotubes on the performance of thermoplastic starch nanocomposites,” *Carbohydr. Polym.*, vol. 83, no. 2, pp. 447–451, Jan. 2011.
- [48] R. Li, C. Liu, and J. Ma, “Studies on the properties of graphene oxide-reinforced starch biocomposites,” *Carbohydr. Polym.*, vol. 84, no. 1, pp. 631–637, Feb. 2011.
- [49] J. Ma, C. Liu, R. Li, and J. Wang, “Properties and structural characterization of oxide starch/chitosan/graphene oxide biodegradable nanocomposites,” *J. Appl. Polym. Sci.*, vol. 123, no. 5, pp. 2933–2944, Mar. 2012.
- [50] Y. Feng, N. Feng, and G. Du, “A green reduction of graphene oxide via starch-based materials,” *RSC Adv.*, vol. 3, no. 44, pp. 21466–21474, Nov. 2013.
- [51] P. K. Sandhya, M. S. Sreekala, M. Padmanabhan, K. Jesitha, and S. Thomas, “Effect of starch reduced graphene oxide on thermal and mechanical properties of phenol formaldehyde resin nanocomposites,” *Compos. Part B Eng.*, vol. 167, no. March 2018, pp. 83–92, Jun. 2019.
- [52] T. Ma, P. R. Chang, P. Zheng, and X. Ma, “The composites based on plasticized starch and graphene oxide/reduced graphene oxide,” *Carbohydr. Polym.*, vol. 94, no. 1, pp. 63–70, Apr. 2013.
- [53] P. Zheng, T. Ma, and X. Ma, “Fabrication and Properties of Starch-Grafted Graphene Nanosheet/Plasticized-Starch Composites,” *Ind. Eng. Chem. Res.*, vol. 52, no. 39, pp. 14201–14207, Oct. 2013.

- [54] W. H. Ferreira, K. Dahmouche, and C. T. Andrade, "Dispersion of reduced graphene oxide within thermoplastic starch/poly(lactic acid) blends investigated by small-angle X-ray scattering," *Carbohydr. Polym.*, vol. 208, pp. 124–132, Mar. 2019.
- [55] C. Rodríguez-González, A. L. Martínez-Hernández, V. M. Castaño, O. V. Kharissova, R. S. Ruoff, and C. Velasco-Santos, "Polysaccharide Nanocomposites Reinforced with Graphene Oxide and Keratin-Grafted Graphene Oxide," *Ind. Eng. Chem. Res.*, vol. 51, no. 9, pp. 3619–3629, Mar. 2012.
- [56] Y. He *et al.*, "Biodegradable amylose films reinforced by graphene oxide and polyvinyl alcohol," *Mater. Chem. Phys.*, vol. 142, no. 1, pp. 1–11, Oct. 2013.
- [57] J. H. Han, G. H. Seo, I. M. Park, G. N. Kim, and D. S. Lee, "Physical and Mechanical Properties of Pea Starch Edible Films Containing Beeswax Emulsions," *J. Food Sci.*, vol. 71, no. 6, pp. E290–E296, Aug. 2006.
- [58] S. J. Walker, "The structure of graphite," *Proc. R. Soc. London. Ser. A, Contain. Pap. a Math. Phys. Character*, vol. 106, no. 740, pp. 749–773, Dec. 1924.
- [59] P. R. Wallace, "The Band Theory of Graphite," *Phys. Rev.*, vol. 71, no. 9, pp. 622–634, May 1947.
- [60] M. D. Stoller, S. Park, Y. Zhu, J. An, and R. S. Ruoff, "Graphene-Based Ultracapacitors," *Nano Lett.*, vol. 8, no. 10, pp. 3498–3502, Oct. 2008.
- [61] R. R. Nair *et al.*, "Fine Structure Constant Defines Visual Transparency of Graphene," *Science*, vol. 320, no. 5881, pp. 1308–1308, Jun. 2008.
- [62] P. Z. Sun *et al.*, "Limits on gas impermeability of graphene," *Nature*, vol. 579, no. 7798, pp. 229–232, Mar. 2020.
- [63] S. Hu *et al.*, "Proton transport through one-atom-thick crystals," *Nature*, vol. 516, no. 7530, pp. 227–230, Dec. 2014.
- [64] F. Bonaccorso, A. Lombardo, T. Hasan, Z. Sun, L. Colombo, and A. C. Ferrari, "Production and processing of graphene and 2d crystals," *Mater. Today*, vol. 15, no. 12, pp. 564–589, Dec. 2012.
- [65] Y. Xu, H. Cao, Y. Xue, B. Li, and W. Cai, "Liquid-Phase Exfoliation of Graphene: An Overview on Exfoliation Media, Techniques, and Challenges," *Nanomaterials*, vol. 8, no. 11, p. 942, Nov. 2018.
- [66] K. R. Paton *et al.*, "Scalable production of large quantities of defect-free few-layer graphene by shear exfoliation in liquids," *Nat. Mater.*, vol. 13, no. 6, pp. 624–630, Jun. 2014.
- [67] T. J. Nacken, C. Damm, J. Walter, A. Rüger, and W. Peukert, "Delamination of graphite in a high pressure homogenizer," *RSC Adv.*, vol. 5, no. 71, pp. 57328–57338, 2015.
- [68] P. G. Karagiannidis *et al.*, "Microfluidization of Graphite and Formulation of Graphene-Based Conductive Inks," *ACS Nano*, vol. 11,

- no. 3, pp. 2742–2755, Mar. 2017.
- [69] A. Ciesielski and P. Samori, “Graphene via sonication assisted liquid-phase exfoliation,” *Chem. Soc. Rev.*, vol. 43, no. 1, pp. 381–98, Jan. 2014.
 - [70] G. Cravotto and P. Cintas, “Sonication-Assisted Fabrication and Post-Synthetic Modifications of Graphene-Like Materials,” *Chem. - A Eur. J.*, vol. 16, no. 18, pp. 5246–5259, May 2010.
 - [71] J. N. Israelachvili, *Intermolecular and Surface Forces*, 3rd ed. Elsevier, 2011.
 - [72] H. C. Hamaker, “The London—van der Waals attraction between spherical particles,” *Physica*, vol. 4, no. 10, pp. 1058–1072, Oct. 1937.
 - [73] J. N. Israelachvili, “Special Interactions: Hydrogen-Bonding and Hydrophobic and Hydrophilic Interactions,” in *Intermolecular and Surface Forces*, vol. 4, Elsevier, 2011, pp. 151–167.
 - [74] R. J. Smith, M. Lotya, and J. N. Coleman, “The importance of repulsive potential barriers for the dispersion of graphene using surfactants,” *New J. Phys.*, vol. 12, no. 12, p. 125008, Dec. 2010.
 - [75] V. Georgakilas *et al.*, “Functionalization of Graphene: Covalent and Non-Covalent Approaches, Derivatives and Applications,” *Chem. Rev.*, vol. 112, no. 11, pp. 6156–6214, Nov. 2012.
 - [76] V. Georgakilas *et al.*, “Noncovalent Functionalization of Graphene and Graphene Oxide for Energy Materials, Biosensing, Catalytic, and Biomedical Applications,” *Chem. Rev.*, vol. 116, no. 9, pp. 5464–5519, May 2016.
 - [77] J. Björk, F. Hanke, C.-A. Palma, P. Samori, M. Cecchini, and M. Persson, “Adsorption of Aromatic and Anti-Aromatic Systems on Graphene through π - π Stacking,” *J. Phys. Chem. Lett.*, vol. 1, no. 23, pp. 3407–3412, Dec. 2010.
 - [78] Y. Hsun Su, Y. Kai Wu, S. Tu, and S.-J. Chang, “Electrostatic studies of π - π interaction for benzene stacking on a graphene layer,” *Appl. Phys. Lett.*, vol. 99, no. 16, p. 163102, Oct. 2011.
 - [79] W. Wang, Y. Zhang, and Y.-B. Wang, “Noncovalent π ··· π interaction between graphene and aromatic molecule: Structure, energy, and nature,” *J. Chem. Phys.*, vol. 140, no. 9, p. 094302, Mar. 2014.
 - [80] T. Premkumar and K. E. Geckeler, “Graphene–DNA hybrid materials: Assembly, applications, and prospects,” *Prog. Polym. Sci.*, vol. 37, no. 4, pp. 515–529, Apr. 2012.
 - [81] J. Wang, Z. Chen, and B. Chen, “Adsorption of Polycyclic Aromatic Hydrocarbons by Graphene and Graphene Oxide Nanosheets,” *Environ. Sci. Technol.*, vol. 48, no. 9, pp. 4817–4825, May 2014.
 - [82] D. Parviz, S. Das, H. S. T. Ahmed, F. Irin, S. Bhattacharia, and M. J. Green, “Dispersions of Non-Covalently Functionalized Graphene with Minimal Stabilizer,” *ACS Nano*, vol. 6, no. 10, pp. 8857–8867, Oct. 2012.
 - [83] Y. Shin *et al.*, “Stable, concentrated, biocompatible, and defect-free

- graphene dispersions with positive charge.,” *Nanoscale*, vol. 12, no. 23, pp. 12383–12394, Jun. 2020.
- [84] “Not so transparent,” *Nat. Mater.*, vol. 12, no. 10, pp. 865–865, Oct. 2013.
 - [85] J. Rafiee *et al.*, “Wetting transparency of graphene,” *Nat. Mater.*, vol. 11, no. 3, pp. 217–222, Mar. 2012.
 - [86] Z. Li *et al.*, “Effect of airborne contaminants on the wettability of supported graphene and graphite,” *Nat. Mater.*, vol. 12, no. 10, pp. 925–931, Oct. 2013.
 - [87] M. Munz, C. E. Giusca, R. L. Myers-Ward, D. K. Gaskill, and O. Kazakova, “Thickness-Dependent Hydrophobicity of Epitaxial Graphene,” *ACS Nano*, vol. 9, no. 8, pp. 8401–8411, Aug. 2015.
 - [88] B. Kronberg, K. Holmberg, and B. Lindman, *Surface Chemistry of Surfactants and Polymers*. Chichester, UK: John Wiley & Sons, Ltd, 2014.
 - [89] A. M. Díez-Pascual, C. Vallés, R. Mateos, S. Vera-López, I. A. Kinloch, and M. P. S. Andrés, “Influence of surfactants of different nature and chain length on the morphology, thermal stability and sheet resistance of graphene,” *Soft Matter*, vol. 14, no. 29, pp. 6013–6023, 2018.
 - [90] P. M. Carrasco *et al.*, “High-concentration aqueous dispersions of graphene produced by exfoliation of graphite using cellulose nanocrystals,” *Carbon*, vol. 70, pp. 157–163, Apr. 2014.
 - [91] V. Chabot, B. Kim, B. Sloper, C. Tzoganakis, and A. Yu, “High yield production and purification of few layer graphene by Gum Arabic assisted physical sonication,” *Sci. Rep.*, vol. 3, no. 1, p. 1378, Dec. 2013.
 - [92] Y. Li *et al.*, “Nanocellulose as green dispersant for two-dimensional energy materials,” *Nano Energy*, vol. 13, pp. 346–354, Apr. 2015.
 - [93] A. Brakat and H. Zhu, “Nanocellulose-Graphene Hybrids: Advanced Functional Materials as Multifunctional Sensing Platform,” *Nano-Micro Lett.*, vol. 13, no. 1, p. 94, Jan. 2021.
 - [94] R. Xiong *et al.*, “Wrapping Nanocellulose Nets around Graphene Oxide Sheets,” *Angew. Chemie*, vol. 130, no. 28, pp. 8644–8649, Jul. 2018.
 - [95] S. Immel and F. W. Lichtenthaler, “The Hydrophobic Topographies of Amylose and its Blue Iodine Complex,” *Starch - Stärke*, vol. 52, no. 1, pp. 1–8, Jan. 2000.
 - [96] W. Henry, “III. Experiments on the quantity of gases absorbed by water, at different temperatures, and under different pressures,” *Philos. Trans. R. Soc. London*, vol. 93, pp. 29–274, Dec. 1803.
 - [97] A. Fick, “Ueber Diffusion,” *Ann. der Phys. und Chemie*, vol. 170, no. 1, pp. 59–86, 1855.
 - [98] J. M. Lagaron, R. Catalá, and R. Gavara, “Structural characteristics defining high barrier properties in polymeric materials,” *Mater. Sci.*

- Technol.*, vol. 20, no. 1, pp. 1–7, Jan. 2004.
- [99] K. K. Mokwena and J. Tang, “Ethylene Vinyl Alcohol: A Review of Barrier Properties for Packaging Shelf Stable Foods,” *Crit. Rev. Food Sci. Nutr.*, vol. 52, no. 7, pp. 640–650, Jul. 2012.
 - [100] S. Majee *et al.*, “Low temperature chemical sintering of inkjet-printed Zn nanoparticles for highly conductive flexible electronic components,” *npj Flex. Electron.*, vol. 5, no. 1, p. 14, Dec. 2021.
 - [101] D. McManus *et al.*, “Water-based and biocompatible 2D crystal inks for all-inkjet-printed heterostructures,” *Nat. Nanotechnol.*, vol. 12, no. 4, pp. 343–350, Apr. 2017.
 - [102] N. Reis and B. Derby, “Ink Jet Deposition of Ceramic Suspensions: Modeling and Experiments of Droplet Formation,” *MRS Proc.*, vol. 625, p. 117, Feb. 2000.
 - [103] R. Shanker, S. Sardar, S. Chen, S. Gamage, S. Rossi, and M. P. Jonsson, “Noniridescent Biomimetic Photonic Microdomes by Inkjet Printing,” *Nano Lett.*, vol. 20, no. 10, pp. 7243–7250, Oct. 2020.
 - [104] S. O. Mansoorabadi, C. J. Thibodeaux, and H. Liu, “The Diverse Roles of Flavin Coenzymes Nature’s Most Versatile Thespians,” *J. Org. Chem.*, vol. 72, no. 17, pp. 6329–6342, Aug. 2007.
 - [105] C. Backes *et al.*, “Spectroscopic metrics allow in situ measurement of mean size and thickness of liquid-exfoliated few-layer graphene nanosheets,” *Nanoscale*, vol. 8, no. 7, pp. 4311–4323, 2016.
 - [106] D. Li, M. B. Müller, S. Gilje, R. B. Kaner, and G. G. Wallace, “Processable aqueous dispersions of graphene nanosheets,” *Nat. Nanotechnol.*, vol. 3, no. 2, pp. 101–105, Feb. 2008.
 - [107] C. V. RAMAN and K. S. KRISHNAN, “A New Type of Secondary Radiation,” *Nature*, vol. 121, no. 3048, pp. 501–502, Mar. 1928.
 - [108] A. C. Ferrari *et al.*, “Raman Spectrum of Graphene and Graphene Layers,” *Phys. Rev. Lett.*, vol. 97, no. 18, p. 187401, Oct. 2006.
 - [109] A. C. Ferrari and D. M. Basko, “Raman spectroscopy as a versatile tool for studying the properties of graphene,” *Nat. Nanotechnol.*, vol. 8, no. 4, pp. 235–246, Apr. 2013.
 - [110] S. K. Chapman and G. A. Reid, *Flavoprotein Protocols*, 1st ed., vol. 131. New Jersey: Humana Press, 1999.
 - [111] K. R. Paton and J. N. Coleman, “Relating the optical absorption coefficient of nanosheet dispersions to the intrinsic monolayer absorption,” *Carbon*, vol. 107, pp. 733–738, Oct. 2016.
 - [112] M. Ayán-Varela *et al.*, “Achieving Extremely Concentrated Aqueous Dispersions of Graphene Flakes and Catalytically Efficient Graphene-Metal Nanoparticle Hybrids with Flavin Mononucleotide as a High-Performance Stabilizer,” *ACS Appl. Mater. Interfaces*, vol. 7, no. 19, pp. 10293–10307, May 2015.
 - [113] Z. Baig, O. Mamat, M. Mustapha, A. Mumtaz, K. S. Munir, and M. Sarfraz, “Investigation of tip sonication effects on structural quality of graphene nanoplatelets (GNPs) for superior solvent dispersion,”

- Ultrason. Sonochem.*, vol. 45, no. May 2017, pp. 133–149, Jul. 2018.
- [114] U. Khan, A. O'Neill, M. Lotya, S. De, and J. N. Coleman, "High-Concentration Solvent Exfoliation of Graphene," *Small*, vol. 6, no. 7, pp. 864–871, Apr. 2010.
 - [115] S. Wang, M. Yi, and Z. Shen, "The effect of surfactants and their concentration on the liquid exfoliation of graphene," *RSC Adv.*, vol. 6, no. 61, pp. 56705–56710, 2016.
 - [116] X. Zhou, B.-K. Baik, R. Wang, and S.-T. Lim, "Retrogradation of waxy and normal corn starch gels by temperature cycling," *J. Cereal Sci.*, vol. 51, no. 1, pp. 57–65, Jan. 2010.
 - [117] S.-K. Kim *et al.*, "Retrogradation kinetics of cross-linked and acetylated corn starches under high hydrostatic pressure," *Food Sci. Biotechnol.*, vol. 24, no. 1, pp. 85–90, Feb. 2015.
 - [118] S. Wang, C. Li, L. Copeland, Q. Niu, and S. Wang, "Starch Retrogradation: A Comprehensive Review," *Compr. Rev. Food Sci. Food Saf.*, vol. 14, no. 5, pp. 568–585, Sep. 2015.
 - [119] S. Deng and V. Berry, "Wrinkled, rippled and crumpled graphene: an overview of formation mechanism, electronic properties, and applications," *Mater. Today*, vol. 19, no. 4, pp. 197–212, May 2016.
 - [120] A. Eckmann *et al.*, "Probing the Nature of Defects in Graphene by Raman Spectroscopy," *Nano Lett.*, vol. 12, no. 8, pp. 3925–3930, Aug. 2012.
 - [121] A. Gupta, G. Chen, P. Joshi, S. Tadigadapa, and Eklund, "Raman Scattering from High-Frequency Phonons in Supported n-Graphene Layer Films," *Nano Lett.*, vol. 6, no. 12, pp. 2667–2673, Dec. 2006.
 - [122] H. Wang, Y. Wang, X. Cao, M. Feng, and G. Lan, "Vibrational properties of graphene and graphene layers," *J. Raman Spectrosc.*, vol. 40, no. 12, pp. 1791–1796, Dec. 2009.
 - [123] Y. Hao *et al.*, "Probing Layer Number and Stacking Order of Few-Layer Graphene by Raman Spectroscopy," *Small*, vol. 6, no. 2, pp. 195–200, Jan. 2010.
 - [124] L. G. Cançado *et al.*, "Quantifying Defects in Graphene via Raman Spectroscopy at Different Excitation Energies," *Nano Lett.*, vol. 11, no. 8, pp. 3190–3196, Aug. 2011.
 - [125] A. Eckmann, A. Felten, I. Verzhbitskiy, R. Davey, and C. Casiraghi, "Raman study on defective graphene: Effect of the excitation energy, type, and amount of defects," *Phys. Rev. B*, vol. 88, no. 3, p. 035426, Jul. 2013.
 - [126] W. D. Bowman and T. G. Spiro, "Normal mode analysis of lumiflavin and interpretation of resonance Raman spectra of flavoproteins," *Biochemistry*, vol. 20, no. 11, pp. 3313–3318, May 1981.
 - [127] Y. Nishina, K. Sato, C. Setoyama, H. Tamaoki, R. Miura, and K. Shiga, "Intramolecular and Intermolecular Perturbation on Electronic State of FAD Free in Solution and Bound to Flavoproteins: FTIR Spectroscopic Study by Using the C = O Stretching Vibrations as

- Probes,” *J. Biochem.*, vol. 142, no. 2, pp. 265–272, May 2007.
- [128] M. P. Kabir, Y. Orozco-Gonzalez, G. Hastings, and S. Gozem, “The effect of hydrogen-bonding on flavin’s infrared absorption spectrum,” *Spectrochim. Acta Part A Mol. Biomol. Spectrosc.*, vol. 262, p. 120110, Dec. 2021.
 - [129] S.-Y. Ju, J. Doll, I. Sharma, and F. Papadimitrakopoulos, “Selection of carbon nanotubes with specific chiralities using helical assemblies of flavin mononucleotide,” *Nat. Nanotechnol.*, vol. 3, no. 6, pp. 356–362, Jun. 2008.
 - [130] K. B. Narayanan, H. D. Kim, and S. S. Han, “Biocompatibility and hemocompatibility of hydrothermally derived reduced graphene oxide using soluble starch as a reducing agent,” *Colloids Surfaces B Biointerfaces*, vol. 185, no. 2020, p. 110579, Jan. 2020.
 - [131] R. Kizil, J. Irudayaraj, and K. Seetharaman, “Characterization of Irradiated Starches by Using FT-Raman and FTIR Spectroscopy,” *J. Agric. Food Chem.*, vol. 50, no. 14, pp. 3912–3918, Jul. 2002.
 - [132] J. J. G. van Soest, H. Tournois, D. de Wit, and J. F. G. Vliegenthart, “Short-range structure in (partially) crystalline potato starch determined with attenuated total reflectance Fourier-transform IR spectroscopy,” *Carbohydr. Res.*, vol. 279, no. C, pp. 201–214, Dec. 1995.
 - [133] J. Masłowska and M. Malicka, “Thermal behaviour of riboflavin,” *J. Therm. Anal.*, vol. 34, no. 1, pp. 3–9, Jan. 1988.
 - [134] F. Farivar *et al.*, “Unlocking thermogravimetric analysis (TGA) in the fight against ‘Fake graphene’ materials,” *Carbon*, vol. 179, pp. 505–513, Jul. 2021.
 - [135] S. Kim, M. Jang, M. Park, N.-H. Park, and S.-Y. Ju, “A self-assembled flavin protective coating enhances the oxidative thermal stability of multi-walled carbon nanotubes,” *Carbon*, vol. 117, pp. 220–227, Jun. 2017.
 - [136] P. Aggarwal, D. Dollimore, and K. Heon, “Comparative thermal analysis study of two biopolymers, starch and cellulose,” *J. Therm. Anal.*, vol. 50, no. 1–2, pp. 7–17, Sep. 1997.
 - [137] X. Zhang, J. Golding, and I. Bugar, “Thermal decomposition chemistry of starch studied by ¹³C high-resolution solid-state NMR spectroscopy,” *Polymer*, vol. 43, no. 22, pp. 5791–5796, Jan. 2002.
 - [138] L. S. Guinesi, A. L. da Róz, E. Corradini, L. H. C. Mattoso, E. D. M. Teixeira, and A. A. da S. Curvelo, “Kinetics of thermal degradation applied to starches from different botanical origins by non-isothermal procedures,” *Thermochim. Acta*, vol. 447, no. 2, pp. 190–196, Aug. 2006.
 - [139] P. Aggarwal and D. Dollimore, “A thermal analysis investigation of partially hydrolyzed starch,” *Thermochim. Acta*, vol. 319, no. 1–2, pp. 17–25, Oct. 1998.
 - [140] X. Liu, L. Yu, F. Xie, M. Li, L. Chen, and X. Li, “Kinetics and

- mechanism of thermal decomposition of cornstarches with different amylose/amylopectin ratios,” *Starch - Stärke*, vol. 62, no. 3–4, pp. 139–146, Apr. 2010.
- [141] Y. Qin, C. Liu, S. Jiang, L. Xiong, and Q. Sun, “Characterization of starch nanoparticles prepared by nanoprecipitation: Influence of amylose content and starch type,” *Ind. Crops Prod.*, vol. 87, pp. 182–190, Sep. 2016.
 - [142] H. Grajek, G. Żurkowska, R. Drabent, and C. Bojarski, “The structure of the flavomononucleotide dimer,” *Biochim. Biophys. Acta - Gen. Subj.*, vol. 881, no. 2, pp. 241–247, Apr. 1986.
 - [143] H. Grajek, I. Gryczynski, P. Bojarski, Z. Gryczynski, S. Bharill, and L. Kułak, “Flavin mononucleotide fluorescence intensity decay in concentrated aqueous solutions,” *Chem. Phys. Lett.*, vol. 439, no. 1–3, pp. 151–156, May 2007.
 - [144] M. Sun, T. A. Moore, and P.-S. Song, “Molecular luminescence studies of flavines. I. Excited states of flavines,” *J. Am. Chem. Soc.*, vol. 94, no. 5, pp. 1730–1740, Mar. 1972.
 - [145] R. Chang *et al.*, “Green preparation and characterization of starch nanoparticles using a vacuum cold plasma process combined with ultrasonication treatment,” *Ultrason. Sonochem.*, vol. 58, no. June, p. 104660, Nov. 2019.
 - [146] B. White, S. Banerjee, S. O’Brien, N. J. Turro, and I. P. Herman, “Zeta-Potential Measurements of Surfactant-Wrapped Individual Single-Walled Carbon Nanotubes,” *J. Phys. Chem. C*, vol. 111, no. 37, pp. 13684–13690, Sep. 2007.
 - [147] O. Frank *et al.*, “Compression Behavior of Single-Layer Graphenes,” *ACS Nano*, vol. 4, no. 6, pp. 3131–3138, Jun. 2010.
 - [148] J. Yang, J. Yu, and X. Ma, “Study on the properties of ethylenebisformamide and sorbitol plasticized corn starch (ESPTPS),” *Carbohydr. Polym.*, vol. 66, no. 1, pp. 110–116, Oct. 2006.
 - [149] J. Wang, D. J. Gardner, N. M. Stark, D. W. Bousfield, M. Tajvidi, and Z. Cai, “Moisture and Oxygen Barrier Properties of Cellulose Nanomaterial-Based Films,” *ACS Sustain. Chem. Eng.*, vol. 6, no. 1, pp. 49–70, Jan. 2018.
 - [150] F. Wu, M. Misra, and A. K. Mohanty, “Challenges and new opportunities on barrier performance of biodegradable polymers for sustainable packaging,” *Prog. Polym. Sci.*, vol. 117, p. 101395, Jun. 2021.
 - [151] P. Forssell, “Oxygen permeability of amylose and amylopectin films,” *Carbohydr. Polym.*, vol. 47, no. 2, pp. 125–129, Feb. 2002.
 - [152] X. Ge, H. Li, L. Wu, P. Li, X. Mu, and Y. Jiang, “Improved mechanical and barrier properties of starch film with reduced graphene oxide modified by SDBS,” *J. Appl. Polym. Sci.*, vol. 134, no. 22, Jun. 2017.
 - [153] A. Ashori, “Effects of graphene on the behavior of chitosan and starch nanocomposite films,” *Polym. Eng. Sci.*, vol. 54, no. 10, pp. 2258–

- 2263, Oct. 2014.
- [154] A. M. Nzengu et al., “Novel bionanocomposite films based on graphene oxide filled starch/polyacrylamide polymer blend: structural, mechanical and water barrier properties,” *J. Polym. Res.*, vol. 25, no. 4, p. 86, Apr. 2018.
 - [155] A. Ashori and R. Bahrami, “Modification of Physico-Mechanical Properties of Chitosan-Tapioca Starch Blend Films Using Nano Graphene,” *Polym. Plast. Technol. Eng.*, vol. 53, no. 3, pp. 312–318, Feb. 2014.
 - [156] I. Conti, C. Simioni, G. Varano, C. Brenna, E. Costanzi, and L. M. Neri, “Legislation to limit the environmental plastic and microplastic pollution and their influence on human exposure,” *Environ. Pollut.*, vol. 288, no. July, p. 117708, Nov. 2021.
 - [157] O. A. Bin-Dahman, M. Rahaman, D. Khastgir, and M. A. Al-Harhi, “Electrical and dielectric properties of poly(vinyl alcohol)/starch/graphene nanocomposites,” *Can. J. Chem. Eng.*, vol. 96, no. 4, pp. 903–911, Apr. 2018.
 - [158] N. Gürlür and G. Torğut, “Graphene-reinforced potato starch composite films: Improvement of mechanical, barrier and electrical properties,” *Polym. Compos.*, vol. 42, no. 1, pp. 173–180, Jan. 2021.
 - [159] W. H. Ferreira, K. Dahmouche, and C. T. Andrade, “Tuning the mechanical and electrical conductivity properties of graphene-based thermoplastic starch/poly(lactic acid) hybrids,” *Polym. Compos.*, vol. 40, no. S2, pp. E1131–E1142, Mar. 2019.
 - [160] W. H. Ferreira and C. T. Andrade, “Preparation and Properties of Poly(lactic Acid)/Thermoplastic Starch/Reduced Graphene Oxide Composites,” *Macromol. Symp.*, vol. 381, no. 1, p. 1800113, Oct. 2018.
 - [161] E. B. Secor, P. L. Prabhumirashi, K. Puntambekar, M. L. Geier, and M. C. Hersam, “Inkjet Printing of High Conductivity, Flexible Graphene Patterns,” *J. Phys. Chem. Lett.*, vol. 4, no. 8, pp. 1347–1351, Apr. 2013.
 - [162] E. B. Secor, S. Lim, H. Zhang, C. D. Frisbie, L. F. Francis, and M. C. Hersam, “Gravure Printing of Graphene for Large-area Flexible Electronics,” *Adv. Mater.*, vol. 26, no. 26, pp. 4533–4538, Jul. 2014.
 - [163] W. J. Hyun, E. B. Secor, M. C. Hersam, C. D. Frisbie, and L. F. Francis, “High-Resolution Patterning of Graphene by Screen Printing with a Silicon Stencil for Highly Flexible Printed Electronics,” *Adv. Mater.*, vol. 27, no. 1, pp. 109–115, Jan. 2015.
 - [164] E. B. Secor, B. Y. Ahn, T. Z. Gao, J. A. Lewis, and M. C. Hersam, “Rapid and Versatile Photonic Annealing of Graphene Inks for Flexible Printed Electronics,” *Adv. Mater.*, vol. 27, no. 42, pp. 6683–6688, Nov. 2015.
 - [165] F. Miao, S. Majee, M. Song, J. Zhao, S.-L. Zhang, and Z.-B. Zhang, “Inkjet printing of electrochemically-exfoliated graphene nano-

- platelets,” *Synth. Met.*, vol. 220, pp. 318–322, Oct. 2016.
- [166] K. Parvez, R. Worsley, A. Alieva, A. Felten, and C. Casiraghi, “Water-based and inkjet printable inks made by electrochemically exfoliated graphene,” *Carbon*, vol. 149, pp. 213–221, Aug. 2019.
- [167] V. Dua *et al.*, “All-Organic Vapor Sensor Using Inkjet-Printed Reduced Graphene Oxide,” *Angew. Chemie Int. Ed.*, vol. 49, no. 12, pp. 2154–2157, Mar. 2010.
- [168] L. Huang, Y. Huang, J. Liang, X. Wan, and Y. Chen, “Graphene-based conducting inks for direct inkjet printing of flexible conductive patterns and their applications in electric circuits and chemical sensors,” *Nano Res.*, vol. 4, no. 7, pp. 675–684, Jul. 2011.

Acta Universitatis Upsaliensis

*Digital Comprehensive Summaries of Uppsala Dissertations
from the Faculty of Science and Technology 2110*

Editor: The Dean of the Faculty of Science and Technology

A doctoral dissertation from the Faculty of Science and Technology, Uppsala University, is usually a summary of a number of papers. A few copies of the complete dissertation are kept at major Swedish research libraries, while the summary alone is distributed internationally through the series Digital Comprehensive Summaries of Uppsala Dissertations from the Faculty of Science and Technology. (Prior to January, 2005, the series was published under the title "Comprehensive Summaries of Uppsala Dissertations from the Faculty of Science and Technology".)



ACTA
UNIVERSITATIS
UPSALIENSIS
UPPSALA
2022

Distribution: publications.uu.se
urn:nbn:se:uu:diva-465565